THE UNIVERSITY *of* EDINBURGH

This thesis has been submitted in fulfilment of the requirements for a postgraduate degree (e.g. PhD, MPhil, DClinPsychol) at the University of Edinburgh. Please note the following terms and conditions of use:

This work is protected by copyright and other intellectual property rights, which are retained by the thesis author, unless otherwise stated.
A copy can be downloaded for personal non-commercial research or study, without prior permission or charge.
This thesis cannot be reproduced or quoted extensively from without first obtaining permission in writing from the author.
The content must not be changed in any way or sold commercially in any format or medium without the formal permission of the author.
When referring to this work, full bibliographic details including the author, title, awarding institution and date of the thesis must be given.

Colloidal Particles at a Liquid-Liquid Interface – Interactions and Rheology

Iain Muntz

Doctor of Philosophy
The University of Edinburgh
August 2020

Abstract

Colloidal particles at fluid interfaces are present in many industries and applications, including the food, pharmaceutical and cosmetics industries. Much work has focussed on the behaviour of charge stabilised colloidal particles at fluid interfaces, investigating both the interactions between particles and the flow behaviour of a particle laden interface. However, there is markedly less work on sterically stabilised particles at fluid interfaces, which can also be used to create systems with high interfacial area, such as Pickering emulsions. In this work I consider sterically stabilised poly(methyl methacrylate) (PMMA) particles adsorbed to a water-dodecane interface. I investigate the interaction between these particles and develop a novel method for characterising the rheology of a particle laden interface.

I begin by investigating the long-range interaction between PMMA particles adsorbed to a liquid interface. A theory for the interaction between point charges at the interface between two dielectric media with finite screening lengths is developed, which I will argue is relevant further on. The result of this shows that there are three possible contributions to the interaction: a screened monopole term, a screened dipole term and a screened $\frac{1}{r^2}$ term. As it turns out, the screened dipole term is experimentally inaccessible for my system.

For PMMA stabilised by poly(lauryl methacrylate) (PLMA), blinking optical trap (BOT) measurements indicate that the particles are (close to) neutrally charged in oil, while qualitative evidence indicates they also acquire no charge in water. However, radial distribution functions ($g(r)$, measured using fluorescence microscopy) when the PMMA-PLMA particles are adsorbed to an interface evince an unexpectedly long-range interaction. Interparticle potentials, $U(r)$, are extracted from $g(r)$ using two methods: Ornstein-Zernike (OZ) inversion at low surface fraction and reverse Monte Carlo (RMC) at a higher surface fraction. $U(r)$ are also measured at the interface using a BOT. In each case, a single

screened monopole potential can be used to describe the data, with no dipolar contribution evident. To corroborate these findings, a Bayesian model comparison was performed on the BOT data, showing that the single screened monopole potential was ~ 40 times more likely to describe the data than a combination of screened monopole and unscreened dipole.

I also show that a screened $\frac{1}{r^2}$ provides a better fit to our data than an unscreened dipole. The comparison of the screened $\frac{1}{r^2}$ and the single screened monopole shows that at low separations the single screened monopole provides a better fit while at high separations the screened $\frac{1}{r^2}$ provides a better fit. I propose that this long-range interaction arises as the neutrally charged particles behave as neutral holes in the charged plane of the water-dodecane interface. $g(r)$ at varying aqueous salt concentration and pH are consistent with this physical model, providing a method for varying the surface charge density of the fluid interface.

In Chapter 4, I perform Monte Carlo simulations with a bimodal distribution of particles using the single screened monopole interaction discussed. I show that, while well-ordered structures have been observed experimentally for particles interacting with a dipolar potential, particles interacting via a screened monopolar potential with experimentally relevant parameters exhibit no such long-range order. I also show that the method for loading particles on to the interface affects the local structure of the particles. At low surface fraction, a sequential deposition of particles leads to greater local hexagonal ordering. However, at a higher surface fraction, a one-step deposition leads to more local hexagonal ordering. I attribute this effect to particles becoming stuck in areas of the same size particle at high surface fraction in a one step deposition, while in a sequential deposition the larger particles can first rearrange to have larger spacings before the smaller particles are introduced. The possible separation of large and small particles in the one step deposition would lead to greater local hexagonal arrangements but little long-range order.

To probe the rheological response of the particle-laden interface I have developed a novel method for performing interfacial rheology which requires no probe attached directly to the interface, described in Chapter 5. I argue that this method is applicable to applications where, for example, an emulsion being sheared indirectly deforms the droplet interface via deformation of the continuous phase. In addition, the interface probed is purely a particle laden, liquid-liquid interface with no large probe immersed therein. My method uses simultaneous confocal microscopy to track the response of the interface, while shearing the upper oil

phase using a parallel plate rheometer.

Using this method I measure steady shear material properties such as the interfacial viscosity for fluid-like interfaces and the interfacial elastic modulus for solid-like interface. These measurements are consistent with recent studies on a similar system using a more direct probe, however using my indirect technique I can measure lower interfacial viscosities than have previously been reported using a double wall ring interfacial rheometer. As this technique uses simultaneous confocal imaging, it lends itself to structural analysis and I have correlated the rheological response of the interface to the structural behaviour under shear. I show that the structural properties of the interface have an effect on the shear behaviour, thereby the results from Chapter 4 become particularly relevant, and shearing the interface can have an irreversible effect on the interfacial structure.

Finally, in Chapter 6, I use the indirect rheometry setup from Chapter 5 to measure stress propagation across the liquid-liquid interface. Using tracer particles in the lower water phase, I show, using a velocimetry technique, that the rheological properties of the interface play a key role in stress propagation across the interface. When the interface behaves as a fluid, there is little barrier for stresses to propagate to the lower phase. On the other hand, when the interface behaves as a solid, the response of the lower phase closely follows the response of the interface, i.e. the interface "shields" the lower phase from external stresses. This has profound implications for droplet-like systems in external shears, where the internal phase may need to be protected to maintain its functionality.

Considering these results together, I have improved the understanding of particle-laden interfaces by adding the behaviour of interfacially adsorbed (uncharged) sterically stabilised particles to the existing literature. This has been achieved from a theoretical, simulational, and experimental standpoint, demonstrating new physics in this field. Additionally, I have provided a novel method for probing these systems' rheological properties in an industrially relevant manner, including considering stress profiles across a particle-laden interface which is important for many droplet-like systems in an external flow field. This novel method also allows measurements of remarkably low interfacial viscosities which can be seen for relatively weak rheological responses of, for instance, PMMA particles at water-oil interfaces.

Lay Summary

Interfaces, boundaries between two materials, occur everywhere in the world we live in, such as between the ground and the air, the sea and the air, or oil and vinegar. The examples I have given are three different types of interface, namely a solid-gas, a liquid-gas and a liquid-liquid interface. In my work I focus on liquid-liquid interfaces, although the results might also be applied to liquid-air interfaces in a lot of cases.

Now, the interface between, for example, water and air is a "simple" interface, which means that it can be fully described by one number called the interfacial tension. This represents the proclivity for the interfacial area to be as small as possible because water and air do not like to be in contact. (Of course water and air have no likes or dislikes but this language is used commonly in the field.) However, in many situations liquid-liquid interfaces are not quite so simple because some molecule or particle will attach to the interface. This can happen because one part of a molecule likes to interact with water while the other part of the molecule likes to interact with oil or air; the molecule, called a surfactant, will therefore bridge between the two media.

In my thesis I study interfaces with solid particles attached. These act a little differently to surfactants, the particle acts as a wall between the two media, preventing them from interacting and therefore lowering the unfavoured interfacial area. Using surfactants or particles allows two liquids to mix which would normally not, like oil and water. By mixing oil, water and a stabiliser large areas of interface can be created and remain stable for long periods of time; an example of this would be in preparing a vinaigrette in which mustard can be added to stabilise the emulsion. An advantage of using particles over surfactants is that they can stabilise large areas for a longer period of time than surfactants can, emulsions have been observed to remain stable for months and years.

When a large number of particles attach to an interface, interesting physics can come into play as the particles interact with each other in manners unique to the situation. For instance, if the particle is heavy enough to change the shape of the interface they can attract each other to try and hide these shape changes. This is the effect commonly seen in a bowl of cereal where bits of cereal will bunch together at the surface of the milk, known as the "Cheerios effect".

The particles I use are small enough, roughly a micron, that they do not deform the interface. However, despite having no interaction when dispersed in oil, they repel each other over a long range when attached to an interface. I describe experiments to measure this interaction and theory to predict how the interaction changes as the particles get closer together. The results reveal an unexpected interaction which has not been seen in previous work.

I then simulate the effect of attaching two different sizes of particle to the interface. I observe that, unlike previously reported systems, the interaction I measure leads to very little order in the arrangement of interfacial particles. I go on to show that this structure has an effect on how easy it is for the interface to be deformed. In doing so I have developed a new method for measuring the flow, or rheological, properties of an interface.

Usually, a tool is submerged into the interface and deformed with a known force. The amount that the tool moves allows measurements of interfacial properties to be made. In my work I induce flow in only the upper medium (the oil) and observe the response of the interface using a microscope. Using this novel technique I show that the structure of particles at the interface plays a key role in the interfacial properties and I also find that this technique allows for much more sensitive measurements to be made.

Finally, I observe the effect of flow in the upper phase on the lower phase. I find that, for interfaces which can flow, the lower phase will also flow with the upper phase. However, for interfaces which can resist flow, behaving more like a solid, the lower phase behaves more like a solid and follows the behaviour of the interface closely. This has important consequences for systems with droplets where the inside of the drop may need to be protected from external flow to maintain their functionality, for example, a mechanically sensitive drug can be delivered via droplets dispersed in water.

Declaration

I declare that this thesis was composed by myself, that the work contained herein is my own except where explicitly stated otherwise in the text, and that this work has not been submitted for any other degree or professional qualification except as specified.

Parts of this work have been published in

Chapter 3: A. Morozov, I. Muntz, J. H. J. Thijssen, and D. Marenduzzo, "Debye-Hückel potential at an interface between two media,", Physical Review E, (accepted), 2020
Chapter 3: I. Muntz, F. Waggett, M. Hunter, A. B. Schofield, P. Bartlett, D. Marenduzzo, J. H. J. Thijssen, "Interaction between Nearly Hard Colloidal Spheres at an Oil-Water Interface", Physical Review Research, **2**(2), 023388, 2020

Chapter 5: I. Muntz, J. H. J.Thijssen, "Interfacial Shear Rheology without an Interfacial Geometry", In Preparation.

(*Iain Muntz, August 2020*)

Acknowledgements

First and foremost I wish to thank Job Thijssen for his excellent supervision in all matters related to my PhD. Thanks also must go to Davide Marenduzzo for his assistance in navigating the simulation work and Alexander Morozov for guiding me through some nasty mathematics. And thanks to Paul Clegg for his advice and support as my second supervisor.

A big thanks has to go to Andy Schofield for synthesising all the particles without which my experiments would be far less interesting and Andy Garrie for constructing instrumentation which was crucial throughout. Also thanks to Paul Bartlett for allowing me the use of his lab setup in Bristol and Ceska Waggett for teaching me how to use said equipment. Also thanks to Rob van Hooghten for digging through old experimental data so that I could compare my results to his. Thanks also to Katy Dickinson and Rudi Mears for practical lab advice and general discussions on my project which also proved useful.

Thanks must go to all the PhD students with whom I ever lunched, played board games, or rebooted the postgrad society as PPA. But special thanks here must go to "O" and "M" who had to put up with my idiosyncrasies for four years and continue to willingly do so.

Finally thanks to Amy for everything and Sookie for being a cat.

Contents

List of Figures

List of Tables

Chapter 1

Introduction and Background

1.1 Overview

Fluid interfaces are common in both industry and nature, from simple interfaces, such as that between water and air, to complex interfaces, which can be found in foodstuffs, cosmetics, or biological cells [1, 2]. While simple interfaces generally lead to a phase separation (e.g. a mixture of water and olive oil will settle to a layer of oil on top of the water), complex interfaces can allow for a system with a large interfacial area which remains stable over a long timescale [2, 3].

In this work, I will focus on complex interfaces created by the adsorption of solid particles to the interface of two immiscible fluids, namely water and dodecane. Solid colloidal particles can irreversibly adsorb to an interface allowing for the production of very long lived emulsions, systems with an extremely large interface which would be unstable to phase separation without a stabilising agent [4]. These particles form a stable film on the surface of a droplet, preventing coalescence of droplets by acting as an "armour" through steric or electrostatic repulsion. Emulsions stabilised solely by solid particles were first produced independently by Pickering and Ramsden early in the 20^{th} century and are known as Pickering emulsions [5, 6].

A more recent focus has been on the interactions between these colloidal particles when adsorbed to a fluid interface. It is well known that charge stabilised particles exhibit a longer range repulsion when adsorbed to an interface than is observed in bulk. This repulsion was first measured as a dipolar interaction by

Pieranski [7], with further experimental work proposing models for the source of this dipole behaviour [8, 9]. However, a long ranged repulsion is also observed when sterically stabilised particles are adsorbed to an interface [10], particles which behave as hard spheres when dispersed in bulk [11]. The models which explain the dipolar behaviour of interfacially adsorbed charge stabilised particles are not applicable in this instance and in this work I introduce a new model to describe my experimental observations.

After considering the quiescent behaviour of a particle laden interface, I then move on to explore the rheological behaviour of this interface. Interfacial rheology is a technique which has been used extensively to probe interfaces, where stresses are applied using a probe attached to the interface allowing for rheological properties to be measured [10, 12–16] (also see review articles on the subject [2, 3]). In this work I develop a novel technique where stresses are applied to the interface indirectly by shearing one of the bulk phases. I show that this technique allows me to measure useful rheological properties while ensuring that the probe is not affecting the response of the interface or the structure of the interface before measurements can be made.

For the rest of this chapter I will give an overview of the adsorption of particles at interfaces and the interactions between them. I will then go into further detail on interfacial shear rheology and its relation to systems of large interfacial area. Chapter 2 will then describe the materials used in the experimental work and provide some detail on the experimental techniques I employ to measure the properties of the interface.

In Chapter 3 I discuss the interaction between nearly hard sphere particles adsorbed to a dodecane-water interface, showing that this interaction is unexpectedly long-range. I describe quantitative results measuring this interaction and provide an explanation for the physical source of the interaction based on the idea of neutral holes in a charged plane. Chapter 4 expands on the work in Chapter 3 by considering the structure of a bimodal distribution of particles adsorbed to an oil-water interface. In light of the Covid-19 pandemic, this work involved Monte Carlo simulations, mimicking experimental conditions, with two different sizes of particle.

I introduce a novel method for interfacial rheology in Chapter 5 which involves no probe attached directly to the particle laden oil-water interface. I show that this method allows for highly sensitive measurements of interfacial viscosity and I

argue that this method is more applicable to industrial processing than previous methods in the literature. The final results chapter, Chapter 6, uses the interfacial rheometer described in Chapter 5 to observe the effect of a complex interface on the propagation of stresses across that interface. Finally, in Chapter 7 I summarise the results presented in this thesis. I also suggest some future work which might be undertaken to continue the work presented here.

The work I present here adds to the existing literature on particle-laden interfaces by investigating the behaviour of interfacially adsorbed (uncharged) sterically stabilised particles. I have probed the interactions between these particles, as well as the resultant structures that are observed, from a theoretical, simulational and experimental viewpoint. Additionally, I have introduced a novel method for interfacial rheology which allows measurements of rheological properties in a more industrially relevant manner. Using this method I have determined how stresses propagate across a particle-laden interface and how this is affected by the interfacial structure.

1.2 Background

1.2.1 Colloidal Particles at Liquid-Liquid Interfaces

It is well known that colloidal particles can irreversibly adsorb to a liquid-liquid interface [17–21]. This phenomenon is central to the stability of certain systems with large interfacial areas, which I will discuss further in section 1.2.2. In this section I will describe the physics behind interfacial adsorption by considering the free energy required to detach a particle from the interface, following chapter 1 of [18].

Here I consider a planar interface around the particle, i.e. there is no meniscus effect, this corresponds to the statement that the effect of gravity is negligible compared to the other forces acting on the particle. This can be checked by calculating the Bond number of the system, a dimensionless quantity which is the ratio of gravitational effects to interfacial tension effects [22, 23],

$$\mathrm{Bo} = \frac{(\rho_\mathrm{w} - \rho_\mathrm{o})R^2 g}{\gamma_\mathrm{ow}}, \tag{1.1}$$

where ρ_{o} (ρ_{w}) is the mass density of oil (water), R is the radius of the particle, g is the gravitational acceleration and γ_{ow} is the interfacial tension. For the system I consider in this work, Bo $\simeq 10^{-8} \ll 1$, indicating that gravitational effects are negligible. For now, this helps to simplify geometries when calculating free energies. In section 1.2.3 however, this point becomes important for considering interparticle interactions.

The free energy of an interface between two phases, F, can be written as the product of the interfacial tension, γ and the area between the two phases, A,

$$F_i = \gamma_i A_i, \tag{1.2}$$

where i describes the interface under consideration. In the case of a colloidal particle adsorbing to an oil/water interface, there are three interfaces present, particle/oil (po), particle/water (pw), and oil/water (ow), each with an associated interfacial tension.

By considering that a hydrophilic ("water loving") particle will preferentially detach into the water phase, and a hydrophobic ("water hating") will detach into the oil phase, we can write the detachment free energy, ΔF_d, in two ways depending on the three phase contact angle of the particle, θ (see Fig. 1.1(a)). Then

$$\Delta F_d = \begin{cases} \pi R^2 \gamma_{\mathrm{ow}} (1 - \cos\theta)^2 & \text{for } 0^\circ \leq \theta \leq 90^\circ \\ \pi R^2 \gamma_{\mathrm{ow}} (1 + \cos\theta)^2 & \text{for } 90^\circ \leq \theta \leq 180^\circ \end{cases} \tag{1.3}$$

can be derived from the geometry of the system and Young's equation, which relates the contact angle to the interfacial tensions between the three phases. Young's equation is given as

$$\cos\theta = \frac{\gamma_{\mathrm{po}} - \gamma_{\mathrm{pw}}}{\gamma_{\mathrm{ow}}}, \tag{1.4}$$

which lets us calculate ΔF_d without needing to measure solid/liquid interfacial tensions. Eq. (1.3) can be written more succinctly as

$$\Delta F_d = \pi R^2 \gamma_{\mathrm{ow}} (1 - |\cos\theta|)^2. \tag{1.5}$$

Fig. 1.1(b) shows a plot of the detachment free energy versus contact angle for an interface with $\gamma_{\mathrm{ow}} = 50$ mNm^{-1} and a particle of radius 1 μm. This plots shows that, over a large range of θ, the free energy of detachment is $> 10^6 k_{\mathrm{B}}T$, verifying the statement that these particles can *irreversibly* attach to an interface. This

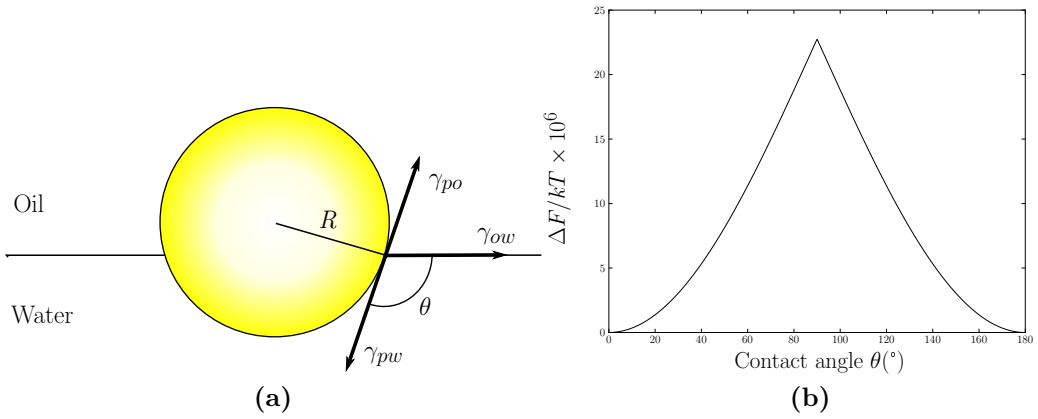

Figure 1.1 *(a) Schematic of a colloidal particle sitting at an oil/water interface. Here the interface is planar signifying that gravity is negligible compared to other forces on the particle. (b) Plot of the free energy of detachment versus contact angle.*

irreversible detachment is a key difference between surfactant laden interfaces and particle laden interfaces, where surfactants adsorb with energies on the order of thermal energies [24].

Appealing to this behaviour, if we were to create large amounts of interface (for instance by mechanical agitation) and allow particles to adsorb to the interface at the same time, this system would remain stable against coalescence as the colloidal particles would act as an armour, coating the interface. This is the basis for creation of Pickering emulsions [5, 6], where the droplets are spherical in shape to minimise the surface area to volume ratio. Other shapes, however, are also possible under specific circumstances. One can create a bicontinuous mixture by initiating a spinodal decomposition phase separation, where the colloidal particles "jam" at the interface before one phase can form spheres, this system is called a bijel (bicontinuous interfacially jammed emulsion gel) [25–27]. The jamming of interfacial particles can also be used to permanently deform droplets from spherical when freezing emulsions, a non-spherical shape being retained upon thawing of the continuous phase [28, 29].

1.2.2 Systems of Large Interfacial Area

As I have mentioned, two systems with large complex surface areas of particular interest are Pickering emulsions and bicontinuous emulsion gels, bijels. These can both be produced using solid particles as interfacial stabilisers to allow two

immiscible substances to remain in some (semi)mixed state [18, 30].

Emulsions exist in many areas, including food, pharmaceuticals and cosmetics. These are mostly oil (or fat) in water emulsions (milk, vinaigrette, moisturiser) although can sometimes be water in oil (butter). Model systems have been available since the works of Ramsden and Pickering in the early 20th century, who created emulsions using well defined, controllable particles [5, 6]. Now, common particles used to stabilise these emulsions are made from poly(methyl methacrylate) (PMMA) [31], silica [32] or latex [33].

In order to indirectly probe the interface of these emulsions, rheology can be performed on an emulsion system. This has been done using a rheoimaging setup [34] in order to measure how these systems differ from the rheology of solid particle dispersions. Different behaviours were observed for droplets with different interactions, which was controlled by varying salt concentration of the continuous phase [35]. The bridging between the droplets in emulsions can also be affected by the shear rate during emulsification, with large shear rates causing large amounts of inter-droplet bridging [36].

The limiting case of single droplets has also been studied, this allows closer examination of the particles adsorbed to the interface and how they behave. One such behaviour is that of "tank treading", a droplet deforms into an ellipsoidal shape when a surrounding flow field is applied and the surface of the droplet rotates. This has been observed in red blood cells in a surrounding flow field [37, 38] as well as vesicles made using lipid solutions [39]. However, when particle coated droplets are subjected to a flow field, this tank treading behaviour is no longer observed [40] due to the large resistance to shear of particle coated surfaces compared with other interfaces. This effect has relevant consequences for situations where an active species is contained in a droplet, for example in some drug delivery applications or in biological cells, where one may want minimal disturbance for the active species during transportation.

A specific class of emulsion is the bijel, where rather than one phase being made of droplets dispersed in a continuous phase, both phases are continuous but still mixed. The overall strength and structure of the bijel is governed in part by the interfacial properties, such as structure and rheological behaviour [3]. The first experimental realisation of bijels was in 2007 by Herzig *et al.* [26] having previously been predicted through simulations in 2005 by Stratford *et al.* [25]. This was done by mixing two partially miscible fluids with particles

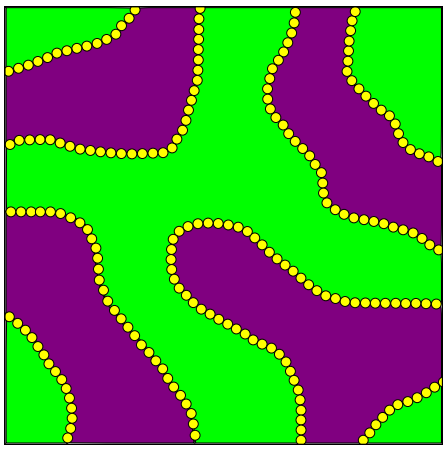

Figure 1.2 *A cartoon representation of a bijel. The two immiscible fluids are coloured green and purple, with the interfacially jammed particles coloured yellow. While this 2d cross section can not be drawn as bicontinuous, in 3 dimensions bicontinuity is observed.*

which are neutrally wetted by both fluids. Demixing of the fluids happened by spinodal decomposition following a thermal quench and the particles adsorbed to the interface during demixing. The adsorption arrested the phase separation leading to a permanent bicontinuous structure which is characteristic of spinodal decomposition [41]. A 2-dimensional representation of the structure is shown in figure 1.2.

1.2.3 Interactions between Interfacial Particles

It has been shown that, when dispersed in organic media, PMMA particles will behave approximately as hard spheres, i.e. have no long range interaction and only a short range interaction when particles come into close proximity, due to their steric stabilisation. This was first shown by Pusey and van Megen in a solution of decalin and carbon disulphide [11] and, more pertinently to this work, has been shown to be true in dodecane (and other alkanes) as well [42, 43].

It is becomingly increasingly clear, however, that when these particles are adsorbed to an oil-aqueous interface, there is a long range interaction between particles [10]. One possible contribution to this interaction is capillary effects. These have been well-studied and arise as deformations in an interface cause particles to either repel or attract each other depending on the specifics of the deformation [14, 44–46]. A schematic of this is shown in figure 1.3. However, these effects are only significant if there is a deformation of the interface, i.e.

gravitational effects become important and Bo $\gtrsim 1$ (c.f. equation (1.1)) or some external force pushes the particles away from their equilibrium position.

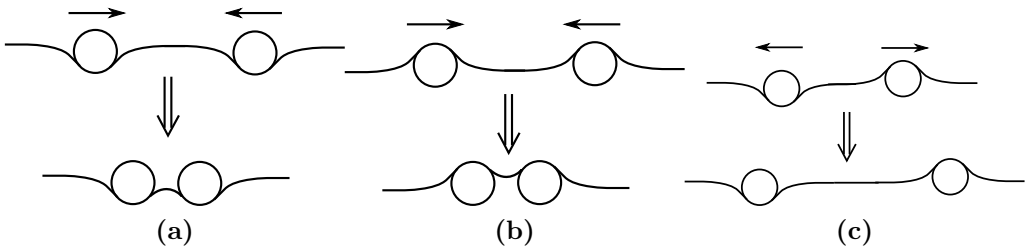

Figure 1.3 *Direction of capillary forces on particles at an interface. (a) and (b) are attractive forces when the menisci have the same orientation while (c) is a repulsive force when the menisci have opposite orientations.*

At this point it is important to distinguish between charge stabilised particles and sterically stabilised particles. Colloidal particles require stabilisation to prevent aggregation due to attractive forces such as van der Waals forces. Charge stabilisation is achieved by producing colloidal particles with surface charges such that the electrostatic repulsion overcomes the van der Waals attraction. On the other hand, steric stabilisation requires a polymer brush to be grafted to the colloidal surface; if two polymer brushes begin to overlap the entropy of the system decreases leading to a repulsive force [41].

For charge stabilised particles which are small enough such that gravitational effects are negligible, i.e. Bo $\ll 1$ (e.g. $\sim$micron sized polystyrene particles), the interaction potential, $U(r)$, between interfacially adsorbed particles is well described by a dipole-dipole interaction:

$$U(r) = \frac{A}{r^3}, \tag{1.6}$$

where A is a prefactor related to the particle's charge and r is the separation between two particles. This form for the interaction potential was first described in an experimental paper by Pieranski in 1980 [7], and theoretically confirmed by Hurd in 1985 [47] following Stillinger's earlier work [48]. The source of the dipole has led to confusion in the literature; the asymmetry in the charge distribution may arise from residual charges trapped at the particle-oil interface [49] or from the finite size of the ionic layer at the particle-water interface [9].

For the case of charges trapped at the particle-oil interface, an image charge of the opposite sign can be considered in the water phase, this leads to an effective

dipole across the water-oil interface. The method of image charges is a tool used to provide analytic solutions to these solutions. Physically, the opposite charge comes from a build up of surface charge at the dielectric boundary which leads to the same analysis and result as solving the image charge setup.

In the case of the finite size of the ionic layer, the charge at the particle-water surface induces a build up of oppositely charged ions near the particle surface. In bulk, this local asymmetry of ions at the particle surface does not produce a dipolar effect as the particle itself has spherical symmetry. However, when a particle is partially submerged in two phases, the ionic build up only occurs on the water side. This asymmetry therefore leads to a dipolar effect and a long-range dipolar repulsion.

Part of this confusion has arisen from conflicting results when salt is added to the water phase. As this repulsion is electrostatic in nature, it is natural to assume that the introduction of electrolytes (e.g. salt) will introduce screening effects and change some aspect of the interaction. It has been shown that, through the introduction of salts the magnitude of the repulsion decreases [50, 51], which suggests that the repulsion arises due to charges building up on the water side of the particle. Earlier work, however, showed no change in repulsion upon the addition of salts [8], implying the main source of the repulsion is from charges on the oil-side of the particle.

In any case, the interaction has been measured repeatedly and with complementary techniques such as inversion of radial distribution functions, $g(r)$, [52] using optical tweezers to directly measure the interaction [53], or inferring the potential from rheological measurements of the interfacial shear modulus [9]. Using these methods it has been shown that charge stabilised particles interact via a dipolar repulsion at oil-water or air-water interfaces. However, no work has been performed to investigate the long-range interaction between interfacially adsorbed sterically stabilised particles which was only recently observed qualitatively [10] and is the subject of Chaper 3 in this thesis.

1.2.4 Interfacial Rheology

Interfacial rheology measures the response of an interface to an imposed stress, for dilational rheology the interface maintains a fixed shape but changes its area, while for shear rheology the interface maintains a fixed area but changes its shape

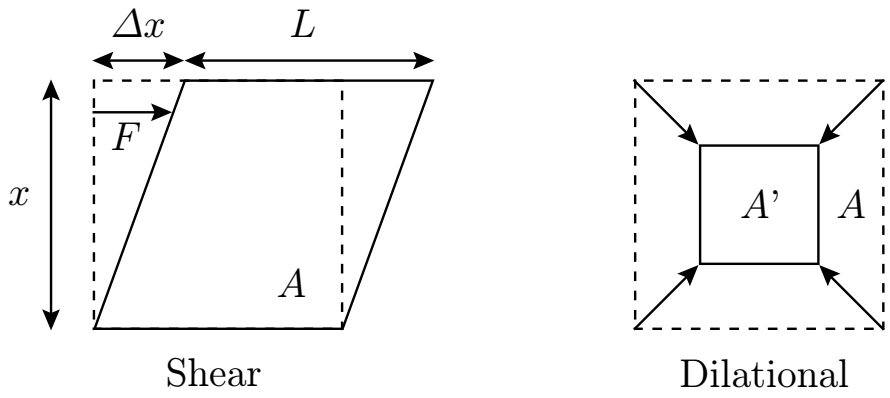

Figure 1.4 *Schematic of a shear deformation and a dilational deformation as labelled showing respectively a change in shape at constant area, A, and a change in area at constant shape. Important parameters when considering a shear deformation are the height of the area, x, the length of the area, L, the force applied to cause the deformation, F, and the size of the deformation, Δx. These parameters are sufficient to determine the shear stress and the shear strain as described in the main text.*

(figure 1.4) [2, 3]. Shear rheology is performed using, for example, a magnetic rod rheometer [54–56] or a double wall ring rheometer [15, 57]. On the other hand, dilational rheology is performed using a setup which allows for a change in interfacial area, such as a Langmuir trough [58–60] or oscillatory pendant drop method [61–63]. The following discussion is limited to shear rheology as this is what is undertaken in this work.

When considering shear deformations there are two key measurements, the interfacial shear stress, σ, which is the force imposed per unit length, and the interfacial shear strain, γ, which is the relative deformation. These are given by (see figure 1.4):

$$\sigma = \frac{F}{L} \quad \gamma = \frac{\Delta x}{x}, \tag{1.7}$$

where F is the force applied along a length L, Δx is the distance moved parallel to that force and x is the length of the sample perpendicular to the force.

One can either impose a fixed shear stress, σ, and measure the resultant strain, or impose a fixed shear strain, γ, and measure the stress required to impose that strain. For a Hookean solid, these are simply related through the shear modulus G:

$$\sigma = G\gamma, \tag{1.8}$$

while for a Newtonian fluid the stress is related to the strain rate, $\dot{\gamma}$ through the

interfacial viscosity, η:

$$\sigma = \eta\dot{\gamma}. \tag{1.9}$$

While these relationships are sufficient to describe a purely viscous or purely elastic interface, many interfaces are complex and have viscoelastic properties. For example, many fluids have a viscosity which is itself a function of the strain rate and equation 1.8 becomes

$$\sigma = \eta(\dot{\gamma})\dot{\gamma}. \tag{1.10}$$

Two common examples are shear thinning and shear thickening fluids where η respectively decreases or increases with an increasing shear rate [41]. While shear thinning and shear thickening fluids are generally considered for bulk materials, the same principles apply for complex interfaces.

Another common method to measure viscoelastic properties is via oscillatory rheology [64]. In this case an oscillatory strain is applied to the sample at a fixed frequency, ω:

$$\gamma(t) = \gamma_0 \cos(\omega t), \tag{1.11}$$

where $\gamma(t)$ is the strain at time t and γ_0 is the amplitude of the oscillation. In order to determine the stress required to provide this oscillation, we must consider the relaxation modulus, $G(t)$, and the superposition principle. The relaxation modulus relates the stress and the strain for a general viscoelastic material when a step strain is imposed, i.e. if

$$\gamma(t) = \begin{cases} 0 & t < 0 \\ \gamma_0 & t > 0 \end{cases}, \tag{1.12}$$

then the stress and strain are related via

$$\sigma = \gamma_0 G(t). \tag{1.13}$$

For an elastic solid $G(t) = G$[1] while for a viscous fluid $G(t) = \eta\delta(t)$ where δ is the Dirac-delta function.

The superposition principle applies for small perturbations of a sample. Suppose a small strain, $\gamma_1(t)$ leads to a stress response $\sigma_1(t)$ and similarly $\gamma_2(t)$ leads to $\sigma_2(t)$. The superposition principle says that if a strain $\gamma(t) = \gamma_1(t) + \gamma_2(t)$ is

[1]Hence the use of the same symbol for these two parameters, it is therefore crucial to be careful in distinguishing $G(t)$, the relaxation modulus, and G, the shear modulus

applied then the response is $\sigma(t) = \sigma_1(t) + \sigma_2(t)$. Now, consider that any strain can be described by a series of small step strains applied at different times, t_i

$$\gamma(t) = \sum_i \Delta\gamma_i \Theta(t - t_i), \tag{1.14}$$

where $\Theta(t)$ is the Heaviside step function. Therefore we can write the stress response as

$$\sigma(t) = \sum_i G(t - t_i)\Delta\gamma_i. \tag{1.15}$$

If we take the limit $\Delta t \to 0$ ($\Delta\gamma_i \to \dot{\gamma}(t_i)dt$) we can convert this sum to an integral given by

$$\sigma(t) = \int_{-\infty}^{t} dt' G(t - t')\dot{\gamma}(t'). \tag{1.16}$$

Now, if we consider applying the oscillatory strain (equation (1.11)) we wish to measure the stress response for an arbitrary viscoelastic material

$$\begin{aligned} \sigma(t) &= \int_{-\infty}^{t} dt' G(t - t')(-\gamma_0 \omega \sin \omega t') \\ &= \int_{0}^{\infty} dt' G(t')(-\gamma_0 \omega \sin \omega (t - t') \\ &= \gamma_0 \left[G'(\omega) \cos \omega t - G''(\omega) \sin \omega t \right]. \end{aligned} \tag{1.17}$$

where I have identified the storage modulus,

$$G'(\omega) = \omega \int_0^{\infty} dt' G(t') \sin \omega t, \tag{1.18}$$

and the loss modulus,

$$G''(\omega) = \omega \int_0^{\infty} dt' G(t') \cos \omega t. \tag{1.19}$$

These are important parameters as they represent the in phase (elastic) and out of phase (viscous) response of the material respectively. The complex modulus, G^*, is then given by

$$G^* = G' + iG'' \tag{1.20}$$

which simply relates the stress and strain via

$$\sigma(t) = \gamma_0 \mathrm{Re}\left[G^*(\omega) e^{i\omega t} \right], \tag{1.21}$$

where Re denotes the real part of the bracketed expression.

When performing interfacial shear rheology, an important parameter to consider is the ratio of the bulk stresses to the interfacial stresses, the Boussinesq number, Bq [2, 3]. This parameter is dependent on the geometry used to probe the interface and therefore an effective geometry is one which maximises this number, i.e. $Bq \gg 1$. The Boussinesq number is given by:

$$Bq = \frac{\eta_S}{\eta L}, \tag{1.22}$$

where η_S is the shear viscosity of the surface, measured in Pa·s·m, η is the shear viscosity of the bulk, measured in Pa·s and L is a length scale appropriate to the geometry used. Formally, this length scale is the ratio of the area over which a stress is applied to the perimeter which surface stresses act on. An appropriate choice for an interfacial geometry is therefore one which minimises L, i.e. has a large perimeter for a given surface area.

It does not require much thought to see that an appropriate geometry for interfacial shear rheology is therefore a long, thin rod; this forms the basis for the magnetic rod interfacial stress rheometer [54]. This uses a magnetised rod residing at a liquid-fluid interface (e.g. water/air or water/oil). Known stresses are then applied to the rod using two large Helmholtz coils and strains are measured using optical microscopy. By using the Helmholtz coils to apply a sinusoidal stress, the interfacial storage and loss moduli can be measured.

Another common geometry for interfacial shear rheology is the double wall ring rheometer (DWR) (figure 1.5). While this generally has a slightly larger Boussinesq number than the magnetic rod rheometer [57], it has the great advantage of being compatible with a rotational rheometer, commonly used for bulk rheology.

This setup is also amenable to simultaneous imaging while rheological measurements are made. "Rheoimaging" was developed in 2008 by Besseling, et al. for bulk rheology using confocal microscopy [34]. The advantage that interfacial rheology has for rheoimaging is that there is only one plane of interest and therefore images can be recorded at video rates using a simple microscope with video recorder [15]. This has been utilised to investigate the effect of interfacial microstructure on interfacial rheological properties, directly observing the microscopic behaviour underlying the interfaces rheological response [16].

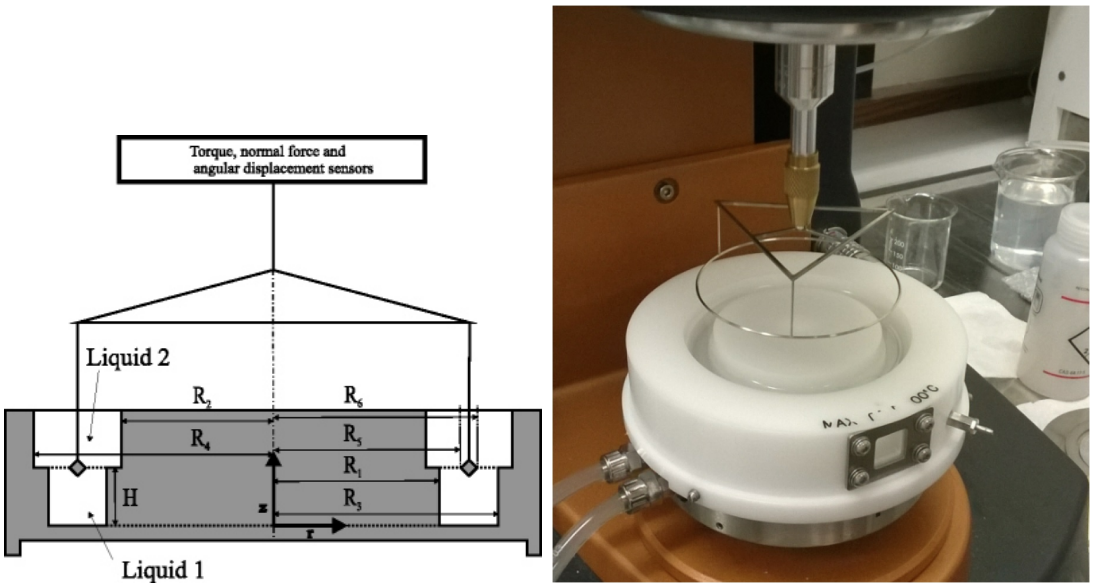

(a) (b)

Figure 1.5 *(a) Cross section of the DWR setup. Reproduced from [57] with permission from Springer Nature. (b) Photograph of the DWR setup.*

Chapter 2

Materials and Methods

2.1 Introduction

In this chapter I describe the materials and methods used throughout this thesis. Materials and methods specific to individual chapters are described in that chapter.

2.2 Materials

Various batches of poly(methyl methacrylate) (PMMA) colloidal particles were used, the specific properties of which are detailed in Table 2.1. Poly(lauryl methacrylate) (PLMA) stabilised PMMA was synthesised following [65], poly(12-hydroxystearic acid) (PHSA) stabilised PMMA was synthesised following [42], and charge stabilised PMMA was synthesised following [66]. The fluorescent dyes 4-chloro-7-nitrobenzo-2-oxa-1,3-diazol (NBD) and DiIC-18 were used for different particle batches as specified in Table 2.1.

Methods to measure particle size, batch polydispersity, and contact angle are described in detail in sections 2.3.3, 2.3.3 and 2.3.4 respectively. The contact angle of batch ASMMAF5 is not given as these particles are never attached to an interface. The contact angle of batch ASM628 is assumed to be the same as ASM629 and has not been explicitly measured. Particle sizes were also verified using a Jeol JSM-6010PLUS/LV Scanning Electron Microscope (SEM) which

Batch	Radius/nm	PD	θ	Dye	Stabiliser
ASM369	940 (DLS) 1100 (SLS)	9% 2.4%	$123 \pm 6°$	NBD	PHSA
ASM628	1400 (DLS) 1500 (SLS)	8% 5%	*	NBD	PLMA
ASM629	1000 (DLS) 1200 (SLS)	6% 2.5%	$123 \pm 4°$	DiIC-18	PLMA
ASMMAF5	230 (DLS) 190 (SLS)	3% 3%	**	DiIC-18	Charge

Table 2.1 *Various properties of the particles used throughout this thesis. DLS: Dynamic Light Scattering; SLS: Static Light Scattering; NBD: 7-nitrobenzo-2-oxa-1,3-diazole; PD: Polydispersity; θ: Three phase contact angle between water/dodecane/particle. *The contact angle of ASM628 is assumed to be the same as ASM629. **As ASMMAF5 is only used in bulk water the contact angle was not measured.*

also verified their spherical shape. However, as SEM measurements are based on imaging, there is a limit to sample size without producing an infeasible amount of raw data. Therefore the results for SEM should only be treated as confirmatory. For ASM369, with a sample size of 300 particles, I find $R = 1040$ nm with a polydispersity of 5.6%, for ASM628, with a sample size of 300 particles, I find $R = 1460$ nm with a polydispersity of 15%[1], and for ASM629, with a sample size of 200 particles, I find $R = 1190$ nm with a polydispersity of 2.8%. The ASMMAF5 particles are considerably smaller therefore more difficult to see using this particular SEM and the size is less important as they are only ever used as tracer particles so SEM data was not taken for these.

All water used was distilled and deionised to a resistivity of 18 MΩcm. The particles were kept in *n*-dodecane (Acros Organics, 99% pure) which is also used as the upper phase in every experiment. Prior to use the *n*-dodecane was cleaned by filtering 3 times through a 25 cm×4 cm cylindrical column of alumina (Honeywell, Aluminium Oxide, activated, basic, Brockmann I). Particle dispersions were kept at volume fractions of 1% or 0.1% and diluted before use to appropriate volume fractions to prepare an interface (described in more detail in § 2.3.1). Before and after each dilution the dispersion was shaken and then sonicated for at least 15 minutes in an ultrasonic bath at 45 kHz and 80 W (VWR, USC300T).

[1]Although the shape of the distribution of particle sizes is non-Gaussian

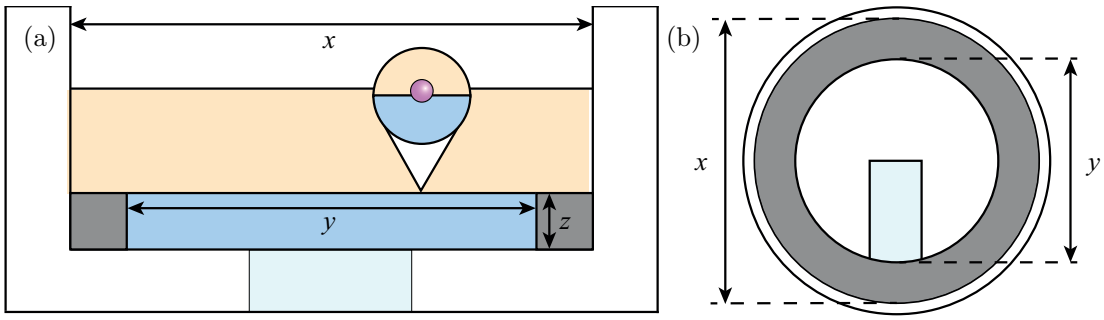

Figure 2.1 *(a) Side view of the PTFE cup, $x = 42mm$, $y = 20mm$, $z = 3mm$. (b) Top view of the PTFE cup, the rectangular, light blue area is the glass viewing window in the bottom of the cup and the grey area is the aluminium ring insert.*

2.3 Methods

2.3.1 Interface Preparation

Interfaces were prepared in a custom made cup, made by Andrew Garrie, which was designed to allow a flat interface as well as visualisation of the interface from both above and below. A schematic for this cup is shown in figure 2.1.

The aluminium ring insert helps to "pin" the interface. The sharp ledge prevents there being a noticeable meniscus and then the interface can be made completely planar by adding the correct volume of the lower, aqueous phase. The flatness of the interface was verified through careful observations of any reflections from the room's lighting as the water is added. For rheology measurements, the inner edge of the aluminium ring was roughened manually with Silicon Carbide sandpaper to facilitate no slip conditions.

As the particles were kept in a dispersion in dodecane there was no need for a spreading solvent, rather, the upper phase was a very low volume fraction dispersion of particles in dodecane with the dodecane remaining as the upper phase. This specific procedure was chosen as initial experiments showed that using a spreading solvent, or using a small amount of high volume fraction dodecane added to an upper phase of pure dodecane lead to a more heterogeneous interfacial structure. The procedure outlined allowed for minimal aggregation at the interface and a uniform interfacial density across the interface.

In order to get a specific surface coverage both the volume and volume fraction of dispersion added as the upper phase must be considered. The volume fraction,

φ, of the dispersion is the ratio of the volume of the particles, $V_{\text{particles}}$, to the total volume of the sample, V_{T},

$$\varphi = \frac{V_{\text{particles}}}{V_{\text{T}}}, \tag{2.1}$$

which, for spherical particles can be rewritten as

$$\varphi = \frac{4\pi R^3 N}{3V_{\text{T}}}, \tag{2.2}$$

where R is the particle radius and N is the number of particles.

The surface fraction, ϕ, is found in a similar way to φ,

$$\phi = \frac{A_{\text{particles}}}{A_{\text{T}}}, \tag{2.3}$$

where A is now an area rather than a volume. We can also rewrite this for spherical particles using the number of particles,

$$\phi = \frac{\pi R^2 N}{A_{\text{T}}}. \tag{2.4}$$

A simple rearrangement then lets us calculate ϕ from known (A_{T}, R), or controllable (φ, V_{T}) parameters to find

$$\phi = \frac{3V_{\text{T}}\varphi}{A_{\text{T}}R}. \tag{2.5}$$

From initial experiments, the surface fraction observed is lower than the theoretical surface fraction which would be measured based on equation 2.5. This is likely due to particles being stuck to the inside of the pipette or to the edge of the cup. At low volume fraction this effect is much more pronounced than at higher volume fraction such that the actual volume fraction required can be up to 5 times higher than expected.

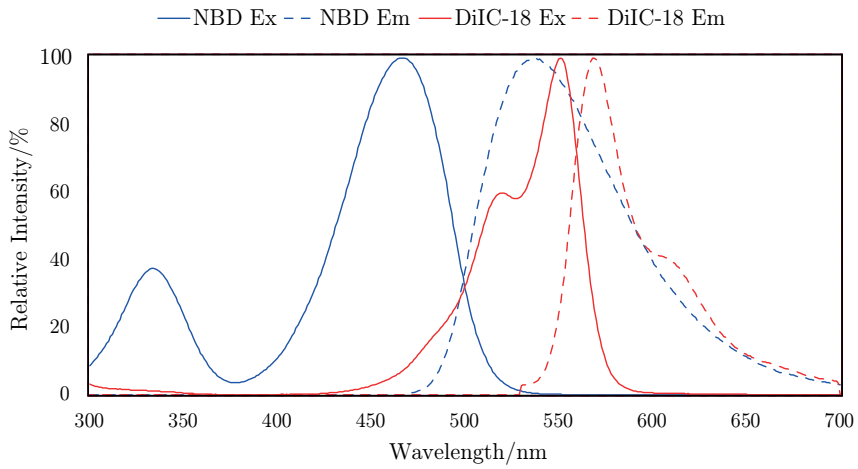

Figure 2.2 *Excitation (Ex, solid lines) and emission (Em, dashed lines) spectra for NBD (blue) and DiIC-18 (red) fluorescent dyes. Data was taken from [67].*

2.3.2 Microscopy

Fluorescence Microscopy

To image the interface, I used a Nikon Eclipse E800 microscope with a Nikon 10× 0.3 NA Plan Fluor objective. In fluorescent microscopy, specific wavelengths of light illuminate the sample. The sample contains a fluorescent dye which adsorb a certain wavelength, λ_{ex}, and emit light at a different specific wavelength, λ_{em}. A mercury-vapour lamp is used to produce light which is then filtered through a filter cube. The filter cube allows one wavelength of light, λ_{in}, to pass in one direction and a different wavelength, λ_{out} to pass in the opposite direction. To use these filter cubes with a fluorescent dye one needs $\lambda_{in} \simeq \lambda_{ex}$ and $\lambda_{out} \simeq \lambda_{em}$. However note that the excitation and emission are distributed over a range of wavelengths with a peak at λ_{ex} and λ_{em} respectively - see figure 2.2 for the excitation and emission spectra for NBD and DiIC-18 [67].

Confocal Microscopy

Confocal microscopy uses the same principle of fluorescence as regular fluorescence microscopy, however the light source is a monochromatic laser rather than a white light source with filters. The main advantage of confocal microscopy over more standard microscopy is the rejection of out of focus light using a pinhole

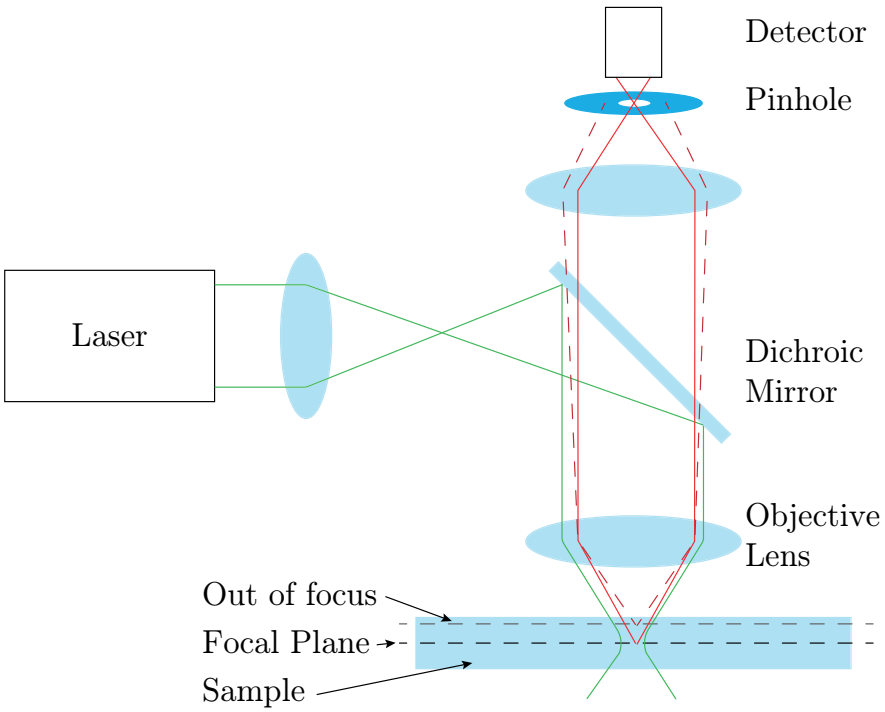

Figure 2.3 *Schematic showing the working principle of a confocal microscope. Out of focus light (red dashed line) is rejected from the detector using a pinhole which allows light from the focal plane (red solid line) to pass.*

in front of the detector (see figure 2.3). The use of a laser, which has a narrow beam, with the pinhole, which rejects out of focus light, allows for the fluorescence of a single, small point in a sample. The laser light then scans through the sample and the emitted light can be collected by a detector, which is typically a photomultiplier tube. The emitted light can be filtered before reaching the detector either using a filter screen or using prisms to selectively refract certain wavelengths into the detector. The configuration leading to rejected out of focus light provides greater axial resolution, or z-resolution. The improved z-resolution allows for 3-dimensional images to be built up if the scanning is not restricted to the xy-plane. This z-scanning can be achieved by a piezzo electric device to allow fast, 3-dimensional fluorescence imaging. For further details see [68].

I use a Leica TCS SP8 confocal microscope with a Leica 10× 0.3 NA PL Fluotar objective lens. The 488 nm laser line is used to excite NBD labelled PMMA and the 555 nm laser line is used to excite DiIC-18 labelled PMMA. The emission is filtered using prisms through a range of wavelengths above the excitation wavelength with a range of approximately 50 nm.

2.3.3 Light Scattering

In light scattering measurements, a monochromatic laser (632.8 nm wavelength) illuminates a sample and the intensity of scattered light is measured. By measuring this intensity as a function of angle or time, information on the particle size can be extracted using static or dynamic light scattering respectively. For further details see [69].

Static Light Scattering (SLS)

In SLS laser light is shone on a sample and the intensity of scattered light is measured at various angles. A model is assumed for the scatterers, in this case colloidal particles. When the particles are spherical and comparable in size to the wavelength of the incoming light the most appropriate model is Mie scattering [70]. This requires the particles to have a constant refractive index, n_p. The refractive index of the solvent, n_s, and the wavelength of the scattered light, λ, are also inputs for the Mie scattering model. In order for the model to be applicable, any scattered light must only be scattered by one particle; this places a limit on the concentration of the particles which becomes a balance between having high enough concentration such that the signal to noise ratio is high but low enough concentration such that the probability of multiple scattering is low.

The light source is a JDSU 1145P He-Ne laser with a wavelength of 632.8 nm, the sample is loaded into a glass vial which sits in a toluene bath kept at 297.6 K with a Haake K20 and DC1 circulating bath and temperature control. The angle is controlled using an ALV cgs-3 goniometer and the light intensity is measured using two Perkin Elmer Photon Counting Modules. The autocorrelation of the light signal can then be measured by an ALV/LSE-5004 correlator. The ALV apparatus is controlled via a PC with ALV Correlator software. The sample is diluted such that the intensity at the detector at 90° is approximately 150 kHz. The scattered intensity was measured every 1° from 30° to 150°. Theoretical plots of intensity vs scattering vector magnitude using Mie theory were generated for particles of mean radius and fixed polydispersity and compared to experimental results by eye. The radius and polydispersity were varied until the theoretical curves matched the experimental curves.

Dynamic Light Scattering (DLS)

In DLS, laser light is shone on the sample and the intensity of scattered light is measured as a function of time at a specific angle. Over time the sample's microstructure changes due to thermal fluctuations and the intensity of the scattered light also changes. The change in intensity over time can be quantified using the autocorrelation of the intensity, where typical timescales can be related to the diffusion of the particle. The particle radius, R, can then be inferred from the diffusion constant of the system using:

$$D = \frac{k_{\mathrm{B}}T}{6\pi\eta R}, \tag{2.6}$$

where $k_{\mathrm{B}}T$ is the thermal energy and η is the solvent viscosity. This relationship is true for spherical particles but defines the "hydrodynamic" radius, which is the effective radius of the particle considering the drag acting on a solvation shell around the particle, rather than the physical radius of the particle. The hydrodynamic radius should be larger than the particle for hard particles and therefore radii measured from DLS are expected to be greater than or the same as those measured using SLS. However, for larger particles sedimentation can play a noticeable role, apparently decreasing the correlation time, leading to a smaller measured radius.

2.3.4 Contact Angle Measurement

To measure the contact angle I use a recently developed spectroscopic technique [71]. This technique relies on the relative difference in refractive index between both media that the particle is in, i.e. the optical path length depends on the contact angle. The intensity of (un)scattered light as a function of wavelength therefore changes depending on the contact angle. By measuring the transmission, $\alpha(\lambda)$, as a function of wavelength for a system of particles in bulk dodecane and particles at an interface, the immersion depth, δ_D, of the particles into the water phase can be determined.

To measure α, the intensity of light transmitted with particles, $S(\lambda)$, without particles, $R(\lambda)$ and with no light source, $D(\lambda)$, must be measured. α is then found via:

$$\alpha(\lambda) = \frac{S(\lambda) - D(\lambda)}{R(\lambda) - D(\lambda)}. \tag{2.7}$$

This transmission spectrum will have a feature, for the particles used here this is a maximum, at a certain wavelength. When we measure $\alpha(\lambda)$ for particles in bulk dodecane we can identify a maximum (or minimum) at a wavelength of λ_{hm} while for particles at the dodecane-water interface we can identify the extreme at λ_{i}. The immersion depth can then be found via:

$$\delta_D = \frac{\lambda_{\mathrm{i}}}{\lambda_{\mathrm{hm}}} \frac{\left(n_p^{(\lambda_{\mathrm{hm}})} - n_1^{(\lambda_{\mathrm{hm}})}\right) - \left(n_p^{(\lambda_{\mathrm{i}})} - n_1^{(\lambda_{\mathrm{i}})}\right)}{\left(n_1^{(\lambda_{\mathrm{i}})} - n_2^{(\lambda_{\mathrm{i}})}\right)}, \tag{2.8}$$

where n are the refractive indices of the particle, p, medium 1 (dodecane) and medium 2 (water) at the wavelengths denoted in the bracketed superscript. Refractive indices are obtained from [72] for water. For dodecane, the empirical formula

$$n^{\lambda}_{\mathrm{dodecane}} = 1.41336 + \frac{2349.37\ \mathrm{nm}^2}{\lambda^2} + \frac{193451000\ \mathrm{nm}^2}{\lambda^4} \tag{2.9}$$

is used, which is derived using refractive index data from [73] to calculate the coefficients of the Cauchy equation up to λ^{-4} [74]. The contact angle, θ can then be determined using:

$$\cos\theta = 2\delta_d - 1. \tag{2.10}$$

In principle, this method will result in accurate measurements for contact angles. Experimental errors shown in Table 2.1 arise from uncertainties in locating the peak of wavelength in $\alpha(\lambda)$ in both bulk and interfacial measurements. It should be noted that this model relies on a monodisperse distribution of contact angles in the particle batch.

2.4 Conclusion

In this Chapter I have first described the materials used throughout this thesis, notably detailing the size, polydispersity and contact angle of particle batches used. I have also described some experimental methods which are used in multiple chapters such as fluorescence and confocal microscopy.

Chapter 3

Interactions between Nearly Hard Colloidal Spheres at a Liquid Interface

The work presented in this chapter has been published as Muntz *et al.*, *Physical Review Research*, 2(2), 023388, 2020 [75]. Part of the work presented here, in particular the development of the neutral hole model, was done in close collaboration with my supervisor, however the singular first person pronoun is used to maintain a consistent style.

3.1 Abstract

I show that the interaction potential between sterically stabilised, nearly hard-sphere (PLMA-PMMA) colloids at a water-oil interface has a negligible unscreened-dipole contribution, suggesting that models previously developed for charged particles at liquid interfaces are not necessarily applicable to sterically stabilised particles. Interparticle potentials, $U(r)$, are extracted from radial distribution functions ($g(r)$, measured by fluorescence microscopy) via Ornstein-Zernike (OZ) inversion and via a reverse Monte Carlo scheme. The results are then validated by particle tracking in a blinking optical trap. Using a Bayesian model comparison, I find that my PLMA-PMMA data is better described by screened monopole only rather than a functional form having a screened monopole

plus an unscreened dipole term. As there is currently no theory available that explains long-range repulsion between interfacial hard spheres, I propose that the long range repulsion I observe arises mainly through interactions between neutral holes on a charged interface i.e. the charge of the liquid interface cannot, in general, be ignored. In agreement with this interpretation, I find that the interaction can be tuned by varying salt concentration or pH in the aqueous phase. Inspired by recent theoretical work on point charges at dielectric interfaces, which I explain is relevant here, I show that a screened $\frac{1}{r^2}$ term can also be used to fit my data. Finally, I present measurements for PHSA-PMMA particles at a water-oil interface. These suggest that, for PHSA-PMMA particles, there is an additional contribution to the interaction potential. This is in line with my optical-tweezer measurements for PHSA-PMMA colloids in bulk oil, which indicate that they are slightly charged.

3.2 Introduction

To make meaningful observations on the rheology of particle laden interfaces, it is constructive to have an understanding of the interactions between those particles. In this chapter, measurements of interfacial interactions are described under varying experimental conditions. A theoretical description for these interactions is given and tested independently by experiments and simulations.

When colloidal particles adsorb to a liquid interface their collective behaviour changes from what is observed in a bulk fluid, namely a longer range interparticle pair potential arises [7–10]. The interparticle interaction affects the microstucture of an assembly of these particles and consequently affects the rheological properties of the interface as a whole [3]. These properties play a role in the formation and stability of systems with large interfacial area, such as particle-stabilised emulsions and foams [2, 3, 76], which have well-known and widely used applications in the personal care, mineral, and food sectors [18, 30, 77, 78]. Understanding the interparticle interactions is therefore important to understand the properties of Pickering systems.

Previous work has considered the microstructure and interactions of charge stabilised particles at liquid-air and liquid-liquid interfaces. Pieranski [7] showed that, for polystyrene particles at a water-air interface, the interaction can be described by a long range dipole-dipole interaction. Further work showed that

a combination of a screened Coulomb potential and a long range dipole-dipole interaction gives a more complete description [47, 48],

$$U(r) = \frac{A}{r} e^{-\kappa r} + \frac{B}{r^3} \ , \tag{3.1}$$

where A and B are prefactors related respectively to the charge and the effective dipole moment of the particles, κ is the screening length in water, and r is the separation between two particles. In the derivation of Eq. 3.1 the two phases are taken as water and air, where notably it is assumed that there are exactly zero free charges in the air (such that Poisson's equation[1] has a right hand side of zero in that region of space), and a point charge is assumed to be sitting exactly in the interface.

Experimental studies on polystyrene particles at oil-water interfaces [8, 9] concluded that the repulsion observed there might be due to charges either on the oil [8] or water [9] side of the particle. While theoretical work assumes a point charge sitting exactly at the interface, the experimental work from Aveyard, *et al.* [8] and Masschaele, *et al.* [9] attribute the dipolar repulsion to an asymmetric distribution of charge caused by the two fluid phases.

In contrast, there has been less work investigating the nature of the interaction between *sterically* stabilised interfacial particles, which can behave as nearly hard spheres when dispersed in a bulk fluid [11]. Like charge stabilised particles, sterically stabilised colloids can be used to stabilise large interfaces. A common particle choice is poly(methyl methacrylate)(PMMA) with polymer hairs grafted to the surface to prevent aggregation due to van der Waals forces [11, 79]. PMMA stabilised with poly(12-hydroxystearic acid) (PHSA) is often used in dodecane as a model hard sphere system [42, 43], although it has recently been noted that when these particles attach to a dodecane-water interface the particles appear to show a long range repulsion [10] – the origin of this repulsion is unclear as these particles have been shown to behave as hard spheres in dodecane [42, 43] and are not stable in water. Additionally, it was found that PHSA-PMMA particles display a dipole-dipole repulsion on interfaces between water and a cyclohexyl bromide (CHB)-alkane mixture which is prone to light-induced dissociation [80, 81]. This arises because PMMA particles suspended in the CHB component acquire an effective charge, consistent with them forming colloidal crystals with large lattice spacings in this solvent, so PMMA in this solvent can be considered

[1] $\nabla^2 \varphi = \frac{-\rho}{\epsilon}$, with φ the electric potential, ρ the charge density and ϵ the permittivity

as a charge stabilised system [82].

In this chapter, I will describe new theoretical work on the interaction between two point charges at a liquid-liquid interface significantly extending the work of Stillinger [48] and Hurd [47]. I will then describe experimental work to measure the interparticle pair potential between interfacially adsorbed sterically stabilised particles using two separate techniques, inverting the radial distribution function, $g(r)$, and direct measurement using a blinking optical trap (BOT). I show that these measurements are consistent with the theoretical description I present and show no measurable dipole contribution, in contrast to what is observed for charge stabilised particles. I attribute the point charge like behaviour to the particles acting as neutral holes in the plane of the charged interface and I will explain why this should give different results than those seen for charged particles. Finally, I will look at further tests of this hypothesis. I will look at what happens when different steric stabilisers are used on the particles and how this affects the behaviour. I will also look at both adding salt to the water phase and altering the pH of the water phase.

3.3 Theory

3.3.1 Background

In 1961, Stillinger investigated "Interfacial Solutions of the Poisson-Boltzmann Equation" [48] considering a point charge at the interface between an electrolyte solution and air. Stillinger arrived at a solution for the pair potential from the linearised Poisson-Boltzmann equation as

$$U(r) = \frac{Q^2}{2\pi\epsilon_{\mathrm{w}}\epsilon_0 r}\int_0^\infty \frac{xJ_0(x)\mathrm{d}x}{(x^2+\kappa_{\mathrm{w}}^2 r^2)^{1/2}+x/\epsilon_{\mathrm{w}}}, \tag{3.2}$$

where $J_0(x)$ is the zero-th order Bessel function of the first kind, Q is the magnitude of the point charge at the interface, ϵ_{w} is the relative permittivity of water, ϵ_0 is the permittivity of free space, r is the charge separation, and κ_{w} is the inverse Debye screening length in water. The numerical integration (Fig. 3.1) of equation (3.2) can be well approximated by a single screened monopole at low separations, followed by a crossover to a dipolar interaction, $U(r) \propto 1/r^3$, at

larger separations[2].

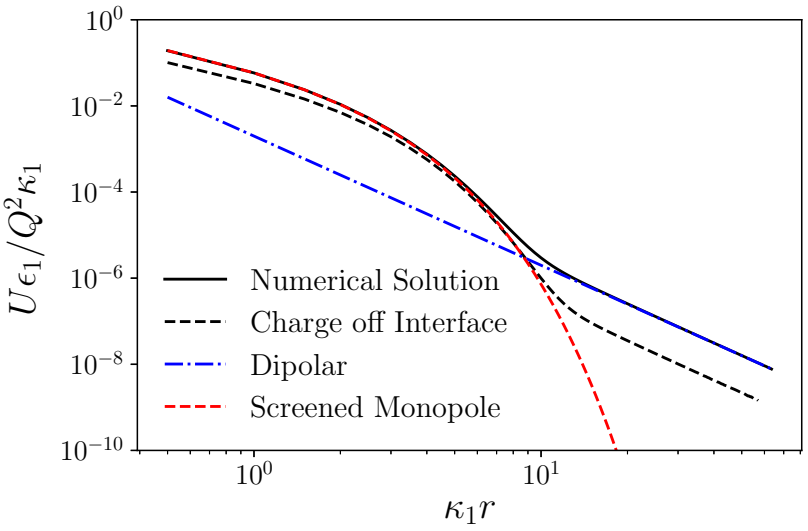

Figure 3.1 *Plot of the numerical integration to the interaction potential, U, between two point charges, Q, at the water-air interface. κ_1 is the screening length in water and ϵ_1 is the permittivity of water. "Off the Interface" refers to the numerical integration of the interaction between two point charges positioned κ_1^{-1} into the water phase, equation (3.3) in text. Also shown is the screened monopolar potential at low separations and the dipolar decay at large separations. The code to calculate numerical integrations to integrals of these types was written by Davide Marenduzzo in Python.*

It was not until Pieranski in 1980 when the first experimental paper proposed a dipolar repulsion between interfacially adsorbed particles [7]. Pieranski trapped charged polystyrene particles at an air-water interface and observed what he refers to as "two-dimensional crystals"[3]. He noted that these particles had a longer ranged repulsion when adsorbed to the interface than when dispersed in bulk, appealing to the inherent asymmetry of the charge he concluded that this would take on a dipolar form with a dipole moment, p of the order $Q\kappa^{-1}$.

At this point it is worth noting that, while there is clear agreement between Pieranski and Stillinger in the results (see Fig. 3.1), the source of this dipolar effect is in fact different in each case. In Pieranski's idea, the charge is entirely

[2]This numerical integration was not presented in Stillinger's work, or indeed the first experimental work done by Pieranski in 1980 where he proposed a dipolar interaction. It was not until Hurd in 1985 when a numerical integration was first reported.

[3]In actuality, crystal was a misnomer from Pieranski as a perfect crystal is impossible in 2 dimensions due to there being no energy barrier to defects [83]

in the water phase, leading to an asymmetric distribution, while in Stillinger's theoretical work the charge is exactly in the interface and the dipolar interaction comes out of Eq. 3.2. One can consider a charge not in the interface using Stillinger's work and, by setting $x = x_c = R$ in equation (15) of [48], one would find

$$U(r) = \frac{Q^2}{4\pi\epsilon_{\mathrm{w}}\epsilon_0 r}\int_0^\infty \frac{xJ_0(x)\mathrm{d}x}{(\kappa_{\mathrm{w}}^2 r^2 + x^2)^{1/2}} \times \left[1 + \frac{\epsilon_{\mathrm{w}}(\kappa_{\mathrm{w}}^2 r^2 + x^2)^{1/2} - x}{\epsilon_{\mathrm{w}}(\kappa_{\mathrm{w}}^2 r^2 + x^2)^{1/2} + x} e^{-\frac{2R}{r}(\kappa_{\mathrm{w}}^2 r^2 + x^2)^{1/2}}\right], \quad (3.3)$$

where I have defined the point charge as being at a distance R into the water phase. The effect of moving the charge R into the water phase is to lower the interaction energy over the entire range, without changing the shape of the curve (figure 3.1). Setting $R = 0$ recovers Eq. 3.2 as expected, and taking R large, i.e. putting the charge into bulk electrolyte, recovers the familiar screened Coulomb potential

$$U(r) = \frac{Q^2}{4\pi\epsilon_{\mathrm{w}}\epsilon_0 r} e^{-\kappa_{\mathrm{w}} r}, \quad (3.4)$$

using the identity

$$\int_0^\infty \frac{xJ_0(x)\mathrm{d}x}{(x^2 + k^2)^{1/2}} = e^{-k}. \quad (3.5)$$

Returning to the case where $R = 0$, Hurd (1985) found that Eq. 3.2 could be written as the sum of two integrals, which can be approximated as the dipole term proposed by Pieranski and a screened monopole term

$$U(r) \simeq \frac{\epsilon_{\mathrm{w}}^2}{\epsilon_{\mathrm{w}}^2 - 1}\frac{2Q^2}{\epsilon_{\mathrm{w}}\epsilon_0}\frac{e^{-\kappa_{\mathrm{w}} r}}{r} + \frac{2Q^2}{\kappa_{\mathrm{w}}^2\epsilon_{\mathrm{w}}^2\epsilon_0}\frac{1}{r^3}. \quad (3.6)$$

Using the physical parameter values given by Hurd, $\kappa_{\mathrm{w}}^{-1} \sim 0.7$ μm and $\epsilon_{\mathrm{w}} \sim 80$, the dipolar term first becomes larger than the screened Coulomb term at separations of 6.10 μm, in line with Pieranski's experiments.

A discrepancy in the κ_{w} dependence of the dipolar term arose when Aveyard, *et al.* found that the interparticle force was independent of salt concentration in the water phase, at odds with the κ_{w} dependence evident in Eq. 3.6 [8]. Frydel, *et al.* proposed that this could be solved by a non-linear charge renormalisation where the effective charge q_{eff} is dependent on both q and κ_{w}. Park, *et al.* [50] found experimentally consistent results for the κ_{w} dependence with good quantitative agreement versus Frydel's work.

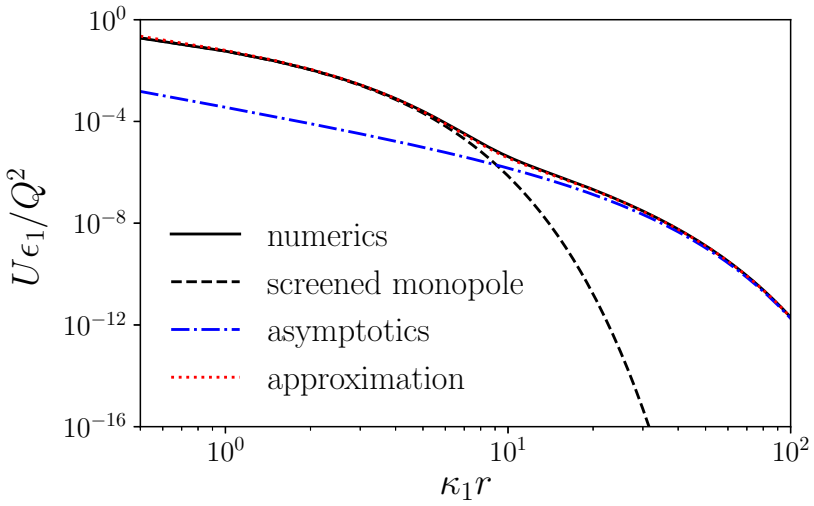

Figure 3.2 *Plot of the numerical integration of $U\epsilon_1/Q^2$ versus $\kappa_1 r$ (equation (3.7)) showing the crossover between low r behaviour, a screened monopole with decay constant κ_1, and asymptotic behaviour. The analytical approximation given in equation (3.9) is also shown. The parameters are chosen such that $\kappa_1 = 10\kappa_2$ and $\epsilon_1 = 40\epsilon_2$.*

3.3.2 Theoretical Work

The work in this section was done in collaboration with Alexander Morozov, Job Thijssen, and Davide Marenduzzo and can be read in more detail at [84].

A crucial assumption from Stillinger's work leading to Eq. 3.2 is that the nonpolar phase has exactly zero free charges, or equivalently that there is no screening – $\kappa = 0$. While this is true for air, recent measurements of colloidal interactions in dodecane imply that this is not necessarily the case for alkanes [85, 86]. Taking this into account, Eq. 3.2 can be amended by considering an inverse screening length in oil κ_o, leading to

$$U(r) = \frac{Q^2}{2\pi\epsilon_0 r}\int_0^\infty \mathrm{d}x \frac{xJ_0(x)}{\epsilon_\mathrm{w}\sqrt{\kappa_\mathrm{w}^2 r^2 + x^2} + \epsilon_\mathrm{o}\sqrt{\kappa_\mathrm{o}^2 r^2 + x^2}}, \tag{3.7}$$

where for dodecane the relative permittivity $\epsilon_\mathrm{o} \sim 2$.

Fig. 3.2 shows the results of a numerical integration to this equation. By plotting this on a log-log plot I can see that for $\kappa_\mathrm{o}/\kappa_\mathrm{w} = 0.1$, parameters appropriate for a water-dodecane system as discussed in the experimental section further on, there

is no apparent dipolar regime. Indeed, a good empirical fit to this solution is

$$U(r) = \frac{A}{r} e^{-\kappa_{\mathrm{w}} r} + \frac{B}{r^2} e^{-\kappa_{\mathrm{o}} r}, \tag{3.8}$$

for $\kappa_{\mathrm{w}} = 1\ \mu\mathrm{m}^{-1}$, $\kappa_{\mathrm{o}} = 0.1\ \mu\mathrm{m}^{-1}$, $\epsilon_{\mathrm{o}} = 2$, and $\epsilon_{\mathrm{w}} = 80$.

Following a similar procedure to Hurd, an analytical approximation can also be found for Eq. 3.7, given by

$$U(r) \simeq \frac{Q^2}{2\pi\epsilon_0} \left(\frac{1}{\epsilon_{\mathrm{w}}} \frac{e^{-\kappa_{\mathrm{w}} r}}{r} + \frac{\epsilon_{\mathrm{o}} \kappa_{\mathrm{o}}}{\epsilon_{\mathrm{w}}^2 \kappa_{\mathrm{w}}^2} \frac{e^{-\kappa_{\mathrm{o}} r}}{r^2} + \frac{\epsilon_{\mathrm{o}}}{\epsilon_{\mathrm{w}}^2 \kappa_{\mathrm{w}}^2} \frac{e^{-\kappa_{\mathrm{o}} r}}{r^3} \right). \tag{3.9}$$

As expected from the numerical fit, the prefactors of the "screened monopole" and "screened $1/r^2$" terms are $\frac{1}{80} \frac{Q^2}{2\pi\epsilon_0}$ and $3.125 \times 10^{-5} \frac{Q^2}{2\pi\epsilon_0}\ \mu\mathrm{m}$, and I can also see the agreement between the numerical integration and the analytical approximation of the integral in Fig. 3.2. Notably, the analytical approximation shows that there is a "screened dipole" term which is the dominant term between $r = 9\kappa_{\mathrm{w}}^{-1}$ and $r = \kappa_{\mathrm{o}}^{-1}$, i.e. for the parameters used for a water-dodecane system, $\kappa_{\mathrm{w}} \simeq 1\ \mu\mathrm{m}^{-1}$ and $\kappa_{\mathrm{o}} \simeq 0.1\ \mu\mathrm{m}^{-1}$, the "screened dipole" term is squeezed out.

3.4 Materials and Methods

The materials and methods not specific to this chapter are described in Chapter 2. In this section methods which are specific to this chapter are described.

3.4.1 Materials

The PLMA-PMMA particles used were batch number ASM629. The PHSA-PMMA particles used were ASM369. For the particle properties see Table 2.1.

3.4.2 Sample Preparation

Interfaces were prepared following section §2.3.1 with surface fractions ranging from 0.1% to 5.0%. Surface fraction was measured by counting the number of particles, N, in a given image area, A_I. Then using the particle's radius, R, as

given in Table 2.1, the surface fraction is found as

$$\phi = \frac{N\pi R^2}{A_I}. \tag{3.10}$$

3.4.3 Measuring $g(r)$

Particle laden interfaces were imaged using a fluorescence microscope (Nikon Eclipse E800, 10× 0.3 NA objective) and the particle positions were located using the trackpy package in Python 3.6.8 [87]. A histogram of particle separations was then produced, $N_{\text{expt}}(r)$, as well as a histogram of particle separations for randomly generated particle positions with the same number of particles, $N_{\text{rand}}(r)$. Here $N_{\text{expt}}(r)$ and $N_{\text{rand}}(r)$ are the number of particles separated by a distance between r and $r+\Delta r$ where Δr is the bin width. The dependence of the data on bin width was tested by varying the number of bins and observing any differences. It was found that at the bin width I used there was no dependence on this. The bin width was controlled by setting the total number of bins to 500. The radial distribution function, $g(r)$, was then found as

$$g(r) = \frac{N_{\text{expt}}(r)}{N_{\text{rand}}(r)}\ . \tag{3.11}$$

This algorithm was chosen in order to minimise any edge effects arising from the finite size of the image. Another method of calculating $g(r)$ from $N_{\text{expt}}(r)$ is using

$$g(r) = \frac{N_{\text{expt}}(r)}{2n\pi r\Delta r}, \tag{3.12}$$

where n is the number density of particles and Δr is the bin size which should be small. I chose not to use this method as, despite the removal of any random contribution from $N_{\text{rand}}(r)$, edge effects become a considerable problem. Considering a particle located close to the corner of the image, using Eq. 3.12, $N(r)$ would be underestimated by roughly a factor of 4. Using Eq. 3.11, however, gets rid of this effect; at large r where edge effects begin to affect Eq. 3.12, the shapes of $N_{\text{rand}}(r)$ and $N_{\text{expt}}(r)$ follow each other closely as seen in Fig. 3.3.

The measured radial distributions were averaged over at least 600 images of the same interface taken at least 1 s apart such that subsequent images were uncorrelated due to Brownian motion.

$g(r)$ were measured at different salt (sodium chloride, NaCl) concentrations

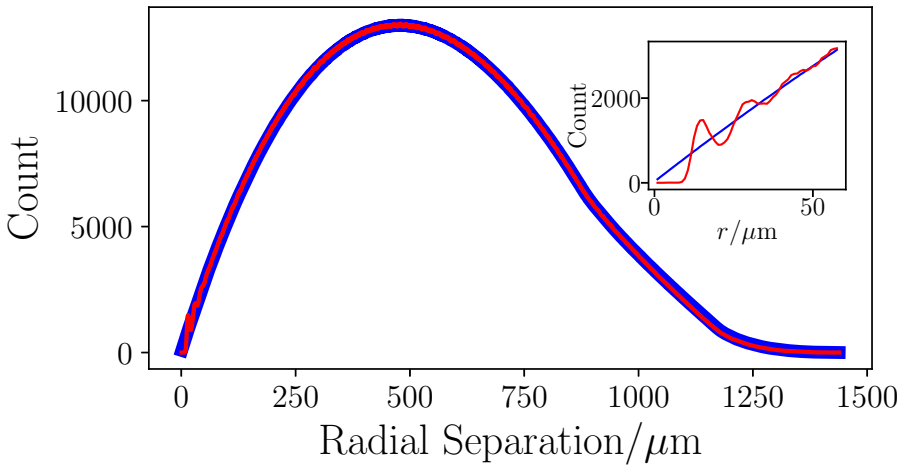

Figure 3.3 *Histogram data for interparticle distances from experiment (red) and a randomly generated distribution (blue). The similarity at the tail end for the randomly distributed particles and the experimental data shows that edge effects are accounted for with this method. The inset shows the behaviour at low separation r, where the linear behaviour of $N_{\mathrm{rand}}(r)$ is clear as well as the deviation of the experimental results from the ideal gas.*

(§ 3.4.6), different pH (§ 3.4.7), and for different particle batches.

3.4.4 Inverting $g(r)$

Measured $g(r)$ were inverted to interparticle pair potentials in two ways: i) Ornstein-Zernicke (OZ) inversion using the hypernetted chain (HNC) or the Percus-Yevick (PY) closure relation and ii) a reverse Monte Carlo scheme comparing experimental $g(r)$ to simulated $g(r)$ using a parameterised potential.

Ornstein-Zernicke Inversion

For infinitely dilute systems, the interparticle pair potential, $U(r)$, is exactly equal to the potential of mean force[4],

$$w(r) = -k_{\mathrm{B}}T\log(g(r)), \tag{3.13}$$

with k_{B} being Boltzmann's constant, T being temperature and log being the natural logarithm often written as ln. At higher concentrations $U(r)$ can be approximated from $w(r)$ using the Ornstein-Zernicke (OZ) integral equation with appropriate closure relations. Two closure relations which give good results are the hypernetted chain (HNC) approximation for soft particles and the Percus-Yevick (PY) approximation for hard particles. These are given by

$$u(r) = w(r) + \begin{cases} nk_{\mathrm{B}}TI(r) & \text{(HNC)} \\ k_{\mathrm{B}}T\log[1+nI(r)] & \text{(PY)} \end{cases}, \tag{3.14}$$

where $I(r)$ is the integral

$$I(r) = \int_0^{g(r)=1} [g(r') - 1 - nI(r)][g(|\mathbf{r}' - \mathbf{r}|) - 1]\mathrm{d}^2r' \tag{3.15}$$

which can be solved iteratively starting from $I(r) = 0$ [88]. The upper limit of the integral should be such that the experimental $g(r)$ has levelled off at 1.

The OZ equations can be used to find an approximate form for $U(r)$ from $g(r)$ by evaluating $I(r)$ numerically. However, this approximation begins to break down for densely packed systems, where correlations persist up to large distances leading to minima in $U(r)$ for purely repulsive systems [52]. Hence, when using the OZ inversion scheme, particles will generally have relatively large separations i.e. there is a lack of information for $U(r)$ at low separations.

The code to invert $g(r)$ was written in Fortran by Davide Marenduzzo.

Reverse Monte Carlo Inversion

$g(r)$ can also be inverted to $U(r)$ using a reverse Monte Carlo (RMC) technique. This involves running a Monte Carlo simulation on a 2d system with a

[4]Note that in this work I assume a central potential, that is $U(\vec{r}) = U(r)$ where $\vec{r}$ is the 2D position vector in the plane of the interface.

parameterised potential, $U(r, \{A_i\})$, where $\{A_i\}$ are fit parameters. For instance, a screened Coulomb potential would have $\{A_i\} = \{A, \kappa\}$ in

$$U(r) = \frac{A}{r} e^{-\kappa r}. \tag{3.16}$$

$g(r)$ were then extracted from these simulations and compared to experimental $g(r)$ at equivalent surface fraction. The fit parameters were then varied and the simulation was rerun until a minimum in a normalised χ_g^2 parameter was found:

$$\chi_g^2 = \frac{1}{N} \sum_{i=1}^{N} \frac{(g_{\text{expt}}^{(i)}(r) - g_{\text{sim}}^{(i)}(r))^2}{\Delta_i^2}, \tag{3.17}$$

where Δ_i is the measured error on measurement point i and there are N such points.

When compared to the OZ inversion, the RMC inversion scheme allows $U(r)$ to be obtained at much lower separations as $g(r)$ can be compared at any experimentally accessible surface fraction. On the other hand, the RMC scheme requires a parameterised potential which is not known *a priori*, and can be computationally expensive rendering the method impractical for parameterisations with more than 2 parameters. Hence, these inversions should be used complementarily to determine the best choice of model (by using OZ) along with the best fit paremeters in that model (by using RMC).

The code to run the RMC scheme was written in Fortran by Davide Marenduzzo.

3.4.5 Blinking Optical Trap

These measurements were done in collaboration with Franceska Waggett and Paul Bartlett in the School of Chemistry at the University of Bristol.

Optical tweezers provide a more direct route to measuring interparticle pair potentials. Generally these are used to measure the force required to hold a particle in the repulsive potential of another particle [53]. Here I use a blinking optical trap (BOT) which measures particle displacement upon release from the trap.

For the bulk measurements, a capillary tube was filled with a dilute suspension (volume fraction $< 1\%$) of particles (§ 3.4.1), the tube was then sealed at either

end and attached to a cover slip with Norland Optical Adhesive UV curing glue. For the interfacial measurements, a dilute layer (surface coverage $\ll 1\%$) of particles was adsorbed onto a water-dodecane interface in a specially constructed cup to allow the water layer to be only 100 μm deep, similar to the geometry described in [53]. The top of the vessel was sealed with a cover slip and vacuum grease to minimise evaporation which can cause undesired particle motion.

In each case, two particles were trapped using a laser of power 0.46 W and wavelength 1064 nm (Diode pumped Nd:YAG Laser, IPG photonics). The particles were brought to a separation where the potential is expected to be small. The optical trap then blinked on and off at a fequency of 20 Hz. During the time that the lasers were off the particles' motions were tracked and the diffusion coefficient, D, and particle speeds, v, were measured from respectively mean squared displacement vs time and displacement vs time plots. The force was then calculated using the Stokes-Einstein relation [89]

$$F = \frac{k_{\mathrm{B}} T v}{D}. \tag{3.18}$$

This was repeated at closer and closer separations. Interparticle potentials were then calculated via a numerical integration in Python using the cumulative trapezoidal method.

3.4.6 Varying Salt Concentration of the Subphase

Interfaces were prepared as in §3.4.2 with the water phase being concentrations of aqueous sodium chloride (NaCl, Thermo Fisher Scientific) solutions. The concentrations used were 0.01 M, 0.1 M and 1.0 M. The upper phase remained dodecane. $g(r)$ were measured in the same way as §3.4.3 and these were inverted to $U(r)$ via the Reverse Monte Carlo scheme described in §3.4.4.

3.4.7 Varying pH of the Subphase

These experiments were performed by Philippa Wright as part of a Senior Honours project in which I ran day-to-day supervision.

Interfaces were prepared as in §3.4.2 with the water phase being concentrations of aqueous sodium chloride (NaCl) solutions and either hydrochloric acid

(HCl, Merck) or sodium hydroxide (NaOH, Thermo Fisher Scientific). The concentrations of NaCl and HCl or NaOH were such that the ionic strength, I, remained constant across various pH values. I is given by

$$I = \frac{1}{2}\sum_i c_i z_i^2, \tag{3.19}$$

where c_i is the molar concentration of ionic species i and z_i is that ion's valency. In each ionic species used for these experiments, $z_i = 1$. The upper phase remained dodecane. $g(r)$ were measured in the same way as §3.4.3.

3.5 Results

3.5.1 $g(r)$ Inversion with no Salt for PLMA-PMMA

I will begin by looking at the results for measuring $g(r)$ for PLMA-PMMA particles at a dodecane-water interface. Firstly, I will look at the results at low surface coverage such that the OZ inversion scheme can be used to obtain $U(r)$. From interfacial micrographs at low surface coverage (figure 3.4a) I observe there is no particular measurable order in the system, however notably there is a clear lack of particles in the vicinity of others, a "void space", indicating a strong repulsion in comparison to thermal energies.

$g(r)$ extracted from interfacial micrographs (figure 3.4b shows a near zero correlation at low separations, with no separation at which correlations greatly exceed 1. This indicates that, beyond the low separation void space particles distribute randomly, i.e. approximately as an ideal gas.

The potential of mean force (figure 3.4c) exhibits a minimum, physically an attractive region of the potential, which I do not expect to observe at large separations, see below for a discussion on possible sources of attraction at lower separations. This seemingly attractive region arises due to many body effects which the potential of mean force inherently includes. Using the HNC or PY closure relations (figure 3.4c) I see no such attractive region, as expected the interparticle potential is purely repulsive at all separations probed.

Following the discussion in section 3.3, I fit the interparticle potentials to various models: 1) a combination of screened monopole and unscreened dipole following

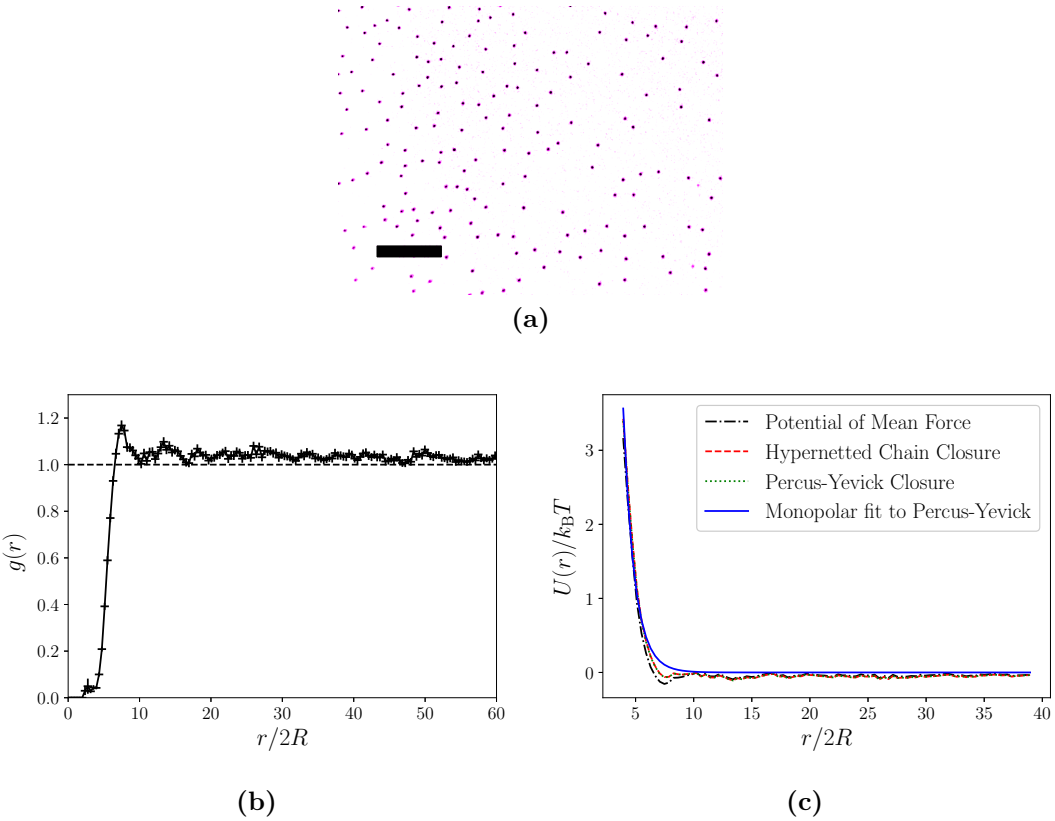

Figure 3.4 *(a) Interfacial micrograph of PLMA-PMMA particles adsorbed to a dodecane-water interface; the scale bar is 100 μm. (Brightness and contrast have been altered and the image has been recoloured for emphasis.) (b) g(r) extracted from series of interfacial micrographs such as that in (a) using a Python code written in house. (c) Potential of mean force (dot-dashed line, black) and interparticle potential calculated using the HNC closure (dashed line, red) or the PY closure (dotted line, green, note that this line is difficult to observe as it lies underneath the HNC line). These results are for PLMA-PMMA particles at a dodecane-water interface at a surface coverage of 0.32%.*

[7–9, 47, 48], 2) a single screened monopole, 3) a single screened $\frac{1}{r^2}$ term, and 4) fitting to equation (3.9) with A, B and C being the prefactors of the screened monopole, screened $\frac{1}{r^2}$ and screened dipole terms respectively. Table 3.1 summarises the results of these fit, including a measure of reduced χ^2 given by

$$\chi^2 = \frac{1}{\nu}\sum_i \frac{(U_i - U_{\text{model}}(r_i))^2}{\sigma_i^2} \tag{3.20}$$

, where $\nu = N - (\text{numberoffreeparameters})$ is the number of degrees of freedom, N is the number of data points, i denotes a data point, U_i is the measured interparticle potential at a separation r_i, $U_{\text{model}}(r_i)$ is the calculated interparticle

Table 3.1 *Summary of the results from OZ inversion of $g(r)$ for PLMA-PMMA particles at a dodecane-water interface. Various models are tested. χ^2 quantifies the difference between the data and the model.*

Model	Fit Parameters	χ^2
$\frac{A}{r}e^{-\kappa r} + \frac{B}{r^3}$	$A = 1000 \pm 200\ k_{\mathrm{B}}T\mu\mathrm{m}$ $B = 1.39 \times 10^{-16} \pm 551\ k_{\mathrm{B}}T\mu\mathrm{m}^3$ $\kappa = 0.27 \pm 0.02\ \mu\mathrm{m}^{-1}$	0.0054
$\frac{A}{r}e^{-\kappa r}$	$A = 1040 \pm 140\ k_{\mathrm{B}}T\mu\mathrm{m}$ $\kappa = 0.271 \pm 0.011\ \mu\mathrm{m}^{-1}$	0.0053
$\frac{A}{r^2}e^{-\kappa r}$	$A = 5500 \pm 800\ k_{\mathrm{B}}T\mu\mathrm{m}^2$ $\kappa = 0.203 \pm 0.011\ \mu\mathrm{m}^{-1}$	0.0059
$\frac{A}{r}e^{-\kappa_1 r} + \frac{B}{r^2}e^{-\kappa_2 r} + \frac{C}{r^3}e^{-\kappa_2 r}$	$A = 1040 \pm 140\ k_{\mathrm{B}}T\mu\mathrm{m}$ $B = 0.83 \pm 0\ k_{\mathrm{B}}T\mu\mathrm{m}^2$ $C = 1.00 \times 10^{-10} \pm 0\ k_{\mathrm{B}}T\mu\mathrm{m}^3$ $\kappa_1 = 0.271 \pm 0.011\ \mu\mathrm{m}^{-1}$ $\kappa_2 = 32.6 \pm 0\ \mu\mathrm{m}^{-1}$	0.0055

potential from the model and the best fir parameters, and σ_i is the experimental error on data point i .

From the χ^2 values in Table 3.1 the best fit to the data is given by a single screened monopole only. In addition, when fitting to equation (3.9) the best fit parameters are strongly influenced by the initial estimate parameters used in the fitting procedure. This indicates that the screened monopolar term is dominating the χ^2 landscape such that there are multiple local minima due to noise at roughly constant values of A and κ_1, confirmed by apparent zero variances in the parameters C, D and κ_2.

To summarise, the OZ inversion scheme applied to $g(r)$ measured at low density indicates that the system is best described by a single screened monopole. This is contrary to what is observed for charge stabilised particles at liquid-liquid interfaces where a strong dipolar repulsion is observed [8, 9]. I will discuss a possible source of this interaction below, after going through the results from the RMC scheme.

Considering the results from the OZ inversion, I chose to use a single screened

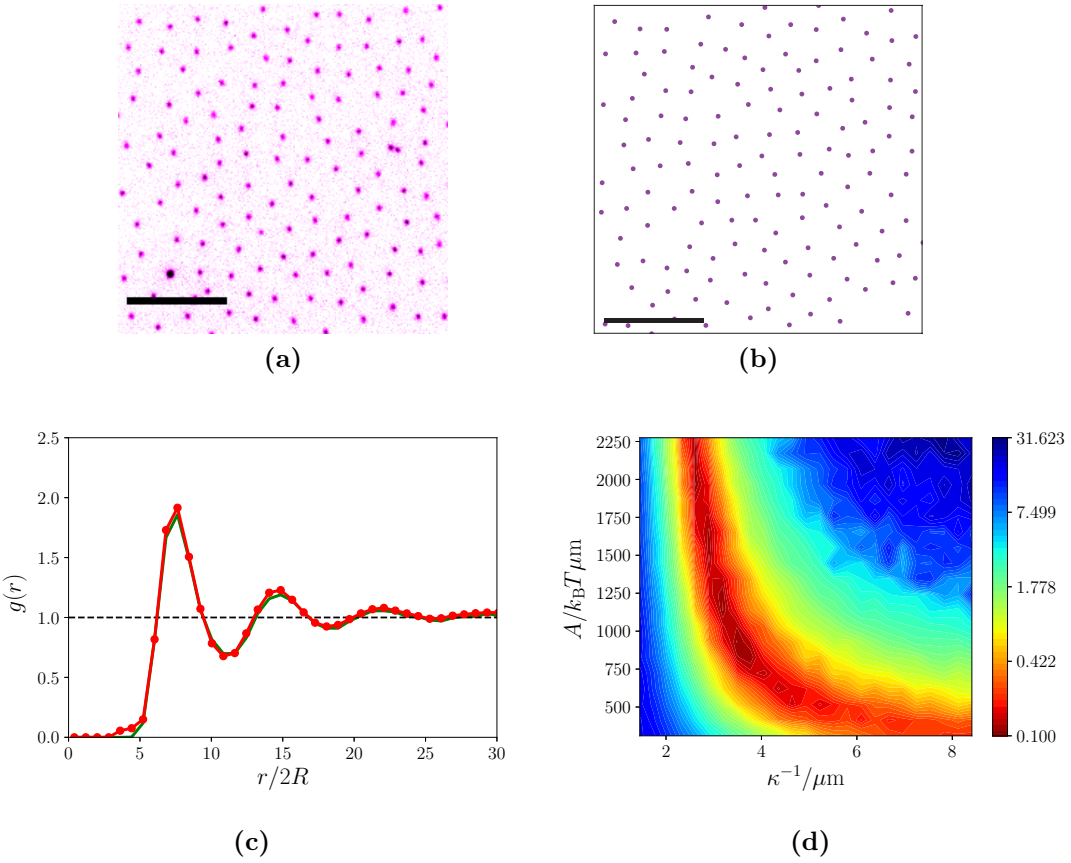

Figure 3.5 *(a) Interfacial micrograph of PLMA-PMMA particles adsorbed to a dodecane-water interface; the scale bar is 100 μm. (b) Simulated snapshot of particles at an interface, scale bar is 100 μm. (c) Comparison of experimental (red line with points) and simulated (green line) $g(r)$ for PLMA-PMMA at particles at $\phi = 2.49\%$. (d) Contour plot of χ^2 as a function of κ^{-1} and A for PLMA-PMMA. Optimal fits are minima in this plot.*

monopole for the parameterised form for the RMC scheme. Qualitatively, the experimental snapshots and the simulated snapshots show very little difference (figures 3.5a and 3.5b). Furthermore, there is very little quantitative difference between $g(r)$ extracted from series of micrographs and $g(r)$ from simulations (figure 3.5c); the minimum in χ^2 occurs at $A = 1964\ k_BT\mu m$ and $\kappa = 0.38\ \mu m^{-1}$ (figure 3.5d). It is notable that there are multiple value of (A, κ) which provide similar values of χ_g^2 – the order of magnitude is the same though. This is expected as phase behaviour should largely depend on the second virial coefficient rather than on A and κ separately. This point may explain the discrepancy between the OZ fit parameters and the RMC fit parameters. In any case, the goodness of the fits indicate that the single screened monopole model can be used to describe this system.

The relatively large value of the Debye screening length, $\kappa^{-1} \simeq 3$ μm, implies that the interaction propagates, at least in part, through the oil phase as water has a maximum Debye length of ~ 1 μm [90][5].

In addition to running the RMC scheme using the single screened monopole potential, a single screened $\frac{1}{r^2}$ and a single screened dipole potential were used. The minimum found in χ_g^2 in each of these cases was larger than that found for the screened monopole potential, i.e. the screened monopole potential continues to give the best fit. Any combination of terms was not run as it would take an infeasible amount of computation time to fit more than 2 parameters using this technique.

3.5.2 Blinking Optical Trap

I will begin by considering the results of the PLMA-PMMA particles dispersed in bulk dodecane, (figure 3.6a). As expected, I measure a very small interaction between a pair of particles, approaching hard-sphere-like behaviour. Moreover, the chemical structure of the PLMA stabiliser does not appear to feature any dissociable groups, so there is no obvious mechanism for these particles to acquire charge in water.

For the interfacial case (figure 3.6b) I repeat the analysis performed to obtain Table 3.1. The results are given in Table 3.2. Again, I observe that the χ^2 values indicate that the best model to describe my system is a single screened monopole.

For a more complete analysis of these results, I have applied a Bayesian model comparison on these datasets to determine the relative likelihood that the data is best described by each of the models set out in Table 3.2. In this Bayesian model comparison, models with more free parameters are penalised due to an "Occam's razor" term. The result of a Bayesian model analysis, comparing for instance models m and d[6], is the posterior ratio - the ratio between the probability of the data being described by respectively models m and d. This posterior ratio can be written as [91]

$$\mathrm{PR} = \frac{P(m|D,I)}{P(d|D,I)}, \tag{3.21}$$

[5]Predicting the Debye length in dodecane *a priori* is a difficult task due to the unknown, low ionic solubility. I will come back to this point when presenting the tweezer results.

[6]These are arbitrary labels but in this case would refer to the monopolar and the dipolar models respectively

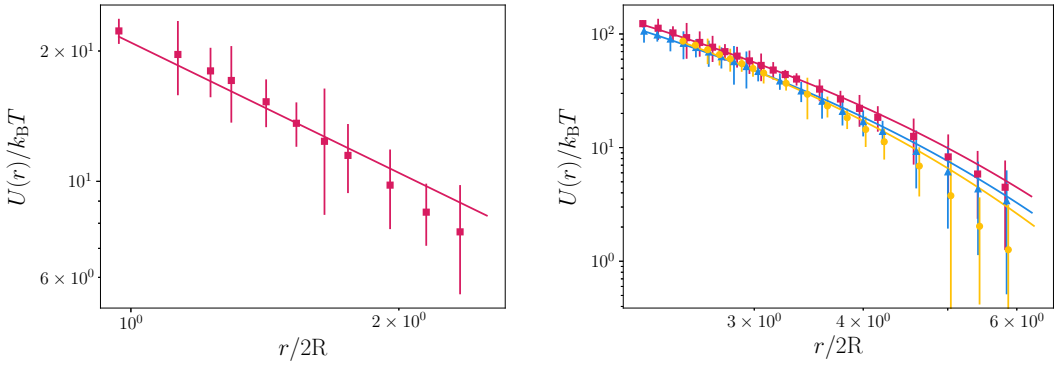

(a) **(b)**

Figure 3.6 *Energy profiles for PLMA-PMMA in bulk dodecane (a) and adsorbed to a dodecane-water interface (b) measured with a blinking optical trap. r is core-to-core separation and R is the particle radius; different symbols/colour correspond to different particle pairs. The solid lines are best fit lines to a screened Coulomb potential (equation (3.16)).*

Table 3.2 *Summary of the results from fitting interaction potentials of PLMA-PMMA particles at a dodecane-water interface measured using a BOT. Various models are tested. χ^2 quantifies the difference between the data and the model*

Model	Fit Parameters	χ^2
$\frac{A}{r}e^{-\kappa r} + \frac{B}{r^3}$	$A = 3250 \pm 180\ k_BT\mu m$ $B = 4.3 \times 10^{-13} \pm 1300\ k_BT\mu m^3$ $\kappa = 0.3021 \pm 0.0017\ \mu m^{-1}$	0.849
$\frac{A}{r}e^{-\kappa r}$	$A = 3250 \pm 70\ k_BT\mu m$ $\kappa = 0.302 \pm 0.003\ \mu m^{-1}$	0.796
$\frac{A}{r^2}e^{-\kappa r}$	$A = 8500 \pm 300\ k_BT\mu m^2$ $\kappa = 0.163 \pm 0.005\ \mu m^{-1}$	2.25
$\frac{A}{r}e^{-\kappa_1 r} + \frac{B}{r^2}e^{-\kappa_2 r} + \frac{C}{r^3}e^{-\kappa_2 r}$	Failed to find optimal parameters	N/A

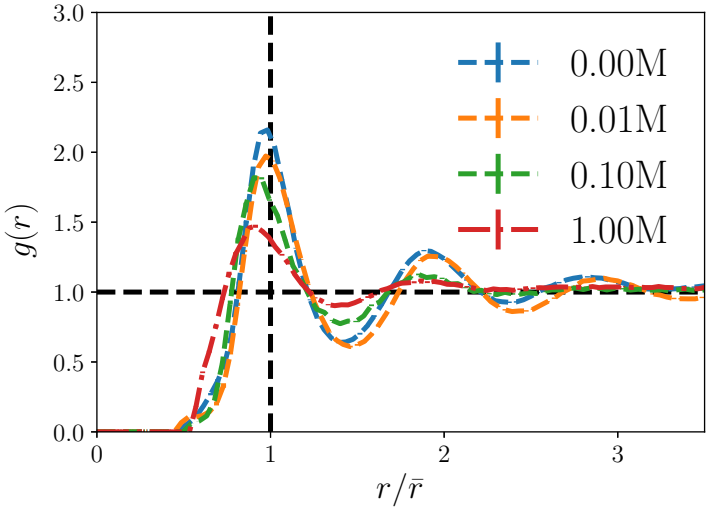

Figure 3.7 *Plot of $g(r)$ for PLMA-PMMA at a dodecane-water interface at various salt concentrations. Surface fractions are: 0.00 M - 3.40%, 0.01 M - 3.23%, 0.1 M - 4.04%, and 1.0 M - 2.92%. $\bar{r}$ is the average interparticle separation based on surface coverage.*

where D is the dataset, I is any initial belief and P is the probability. As usual "|" means "given", i.e. $P(X|Y)$ is the probability of event X given event Y has occurred. For more details on finding an analytical expression for PR see Appendix A.

In the case of comparing a single screened monopole with a combination of a screened monopole and a dipolar term, the Bayesian analysis indicates that the single screened monopole is ~ 40 times more likely to describe three independently measured datasets. Indeed, in each comparison made, the single screened monopole was favoured. Notably, when only fitting the data at large separations ($r > 7$ μm) the screened $\frac{1}{r^2}$ terms becomes favoured according to this analysis.

3.5.3 Varying Salt Concentration of the Subphase

The results of inverting $g(r)$ when PLMA-PMMA particles are adsorbed to a dodecane-salt solution interface (figure 3.7) using the RMC scheme are summarised in Table 3.3. For these inversions, a parameterised potential of a single screened monopole, equation 3.16, was used in line with the results from a water-oil interface with no salt in the water phase. The comparison of experimental and simulated $g(r)$ in each case is shown in Figure 3.8.

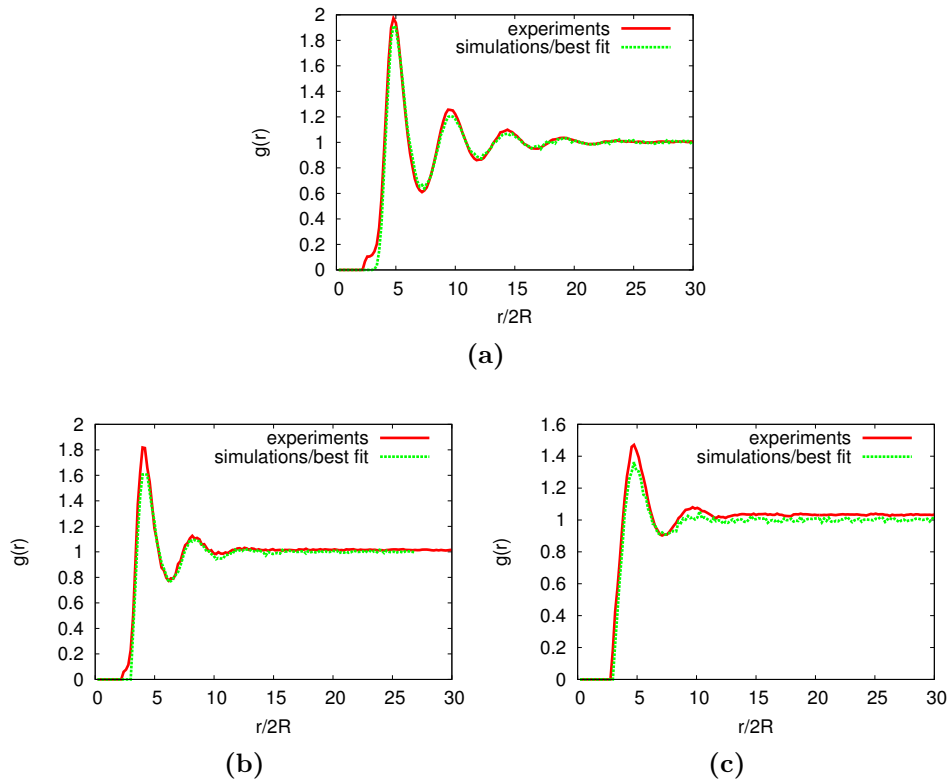

Figure 3.8 *Plots showing the comparison of experimental $g(r)$ and simulated $g(r)$ using a single screened monopolar potential for PLMA-PMMA at a dodecane-water interface at varying salt concentrations: (a) 0.01 M, (b) 0.1 M, and (c) 1.0 M.*

The best fit parameters show a clear trend in the prefactor, A, (c.f. $A = 1964\ k_{\mathrm{B}}T\mu\mathrm{m}$ at 0 M from the same RMC algorithm), with a decreasing A with increasing salt concentration. However, there is no obvious trend in the screening length, with κ initially increasing up to 0.1 M before a lower value being measured at 1.0 M. Note also that the comparison of experimental and simulated $g(r)$ becomes comparatively worse at higher salt concentrations.

In addition, the $g(r)$ were inverted using the same RMC scheme but with a

Table 3.3 *Best fit parameters using the RMC scheme for PLMA-PMMA particles at a salt solution-dodecane interface. The fits are to a single screened monopole, equation 3.16 in the main text.*

Concentration/M	$A/k_{\mathrm{B}}T\mu\mathrm{m}$	$\kappa/\mu\mathrm{m}^{-1}$
0.01	1861	0.43
0.1	1654	0.57
1.0	465	0.41

screened $\frac{1}{r^2}$ parameterisation:

$$U(r) = \frac{A_2}{r^2} e^{-\kappa r}. \tag{3.22}$$

The best fit parameters for this are given in Table 3.4. The comparison of experimental and simulated $g(r)$ in this case is shown in Figure 3.9.

The best fit parameters again show a clear trend in the prefactor, A, with a decreasing A with increasing salt concentration. With this form for the interaction potential, I see a constant screening length at varying salt concentration, implying that the interaction propagates through the oil phase. Note also that the comparison of experimental and simulated $g(r)$ becomes comparatively worse at higher salt concentrations.

3.5.4 Varying pH of the Subphase

There is a clear distinction when varying the pH between $g(r)$ measured at low pH and $g(r)$ measured at high pH, with the higher pH $g(r)$ indicating a more ordered structure as the peak is larger and at higher r (figure 3.10). At the lower pH values, the variation across the three $g(r)$ measurements is insignificant when considered against the variation in surface coverage of these experiments. All things being equal, a higher surface coverage will exhibit more order in $g(r)$ curves; this is true even for a hard sphere system which has no long range interactions.

Table 3.4 *Best fit parameters using the RMC scheme for PLMA-PMMA particles at a salt solution-dodecane interface. The fits are to a screened $\frac{1}{r^2}$ interaction potential.*

Concentration/M	$A_2/k_{\mathrm{B}}T\mu\mathrm{m}^2$	$\kappa_2/\mu\mathrm{m}^{-1}$
0.00M	3200	0.17
0.01	2000	0.15
0.1	800	0.17
1.0	600	0.17

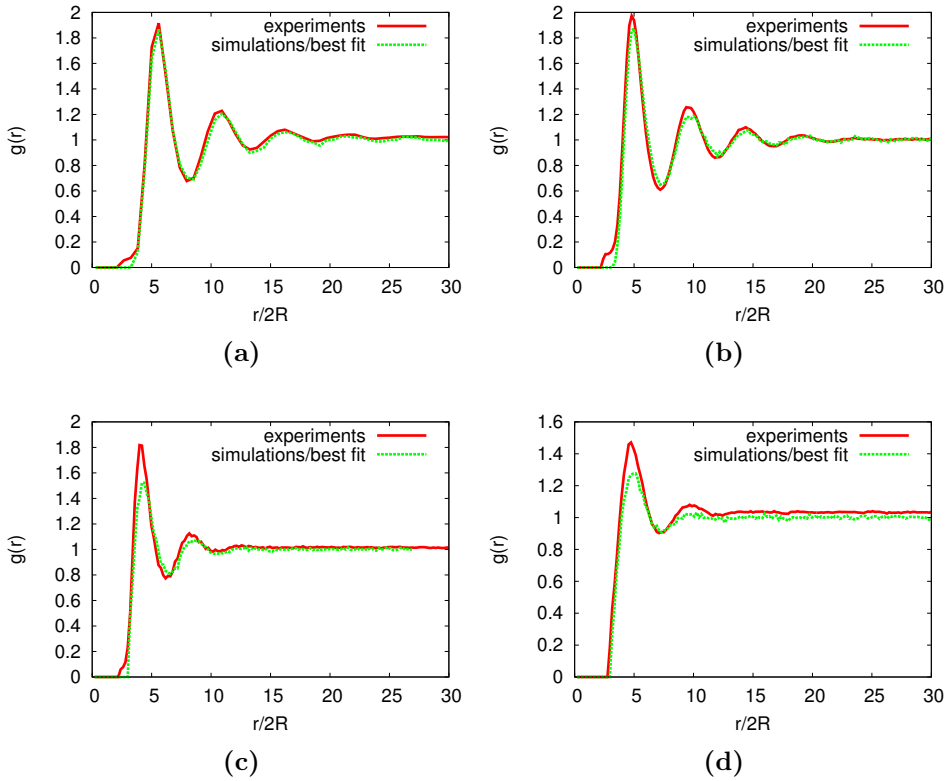

Figure 3.9 *Plots showing the comparison of experimental $g(r)$ and simulated $g(r)$ using a screened $\frac{1}{r^2}$ potential for PLMA-PMMA at a dodecane-water interface at varying salt concentrations: (a) 0.0 M, (b) 0.01 M, (c) 0.1 M, and (d) 1.0 M. These graphs were produced by Davide Marenduzzo using gnuplot.*

3.5.5 Interaction between Interfacial PHSA-PMMA

I also used PHSA-PMMA particles in both $g(r)$ and BOT measurements as these have been widely used in the literature as near hard spheres. Firstly, a comparison of experimental and simulated $g(r)$ (figure 3.11a) using the RMC inversion scheme with a screened monopole model (equation (3.16)) indicates reasonable agreement, although at higher r the agreement becomes worse than for PLMA-PMMA. The fit parameters providing the lowest χ^2 were found to be $A = 4136\ k_{\mathrm{B}}T\mu\mathrm{m}$ and $\kappa = 0.35\ \mu\mathrm{m}^{-1}$. Qualitatively, this inversion scheme for PHSA-PMMA gave a comparatively worse fit than the same scheme applied to PLMA-PMMA, especially at large separations.

The BOT data (figure 3.11b) reveals that the PHSA-PMMA particles do not behave as hard spheres in bulk dodecane (see also [92]). The long range

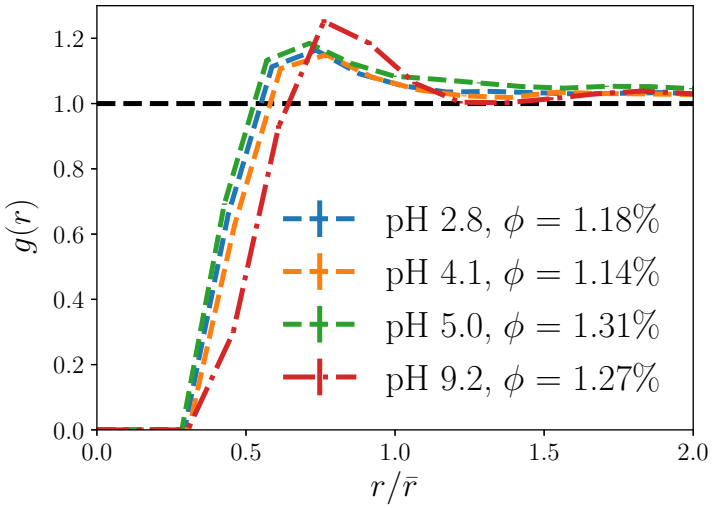

Figure 3.10 *Plot of $g(r)$ for PLMA-PMMA at a dodecane-water interface at various pH values. Surface fractions and pH are given in the legend. $\bar{r}$ is the average interparticle separation based on surface coverage.*

interaction can be fit to equation (3.16) [7] leading to optimal fit parameters of $A = 1400 \pm 70\ k_{\mathrm{B}}T\mu\mathrm{m}$ and a decay length, κ^{-1}, of $10.9 \pm 1.1\ \mu\mathrm{m}$. Using the bulk equivalent of equation (3.4) I find that the particles have a surface charge density of $2.3 \times 10^{-4}\ \mu\mathrm{C\ cm^{-2}}$. It is worth noting that this surface charge density is 4 orders of magnitude lower than the particles used by either Aveyard *et al.* [8] or Masschaele *et al.* [9]. However, when fitting the BOT data at the interface (figure 3.11c), the Bayesian model comparison indicates that these data are ∼10 times more likely to be described by a screened monopole than a combination of a screened monopole and dipole.

3.6 Discussion

The results presented here strongly indicate that sterically stabilised particles behave markedly different from charge stabilised particles when adsorbed to a water-oil interface. While it is well accepted that charge stabilised particles interact with a long-range dipolar interaction, I have measured negligible dipolar forms for the interaction potential. In fact, the potentials measured here are best

[7] Note that this begins to fail as the core to core interparticle separation, r, approaches the particle diameter, $2R$. However, for the data presented here for interfacial interactions r is sufficiently large for this equation to hold.

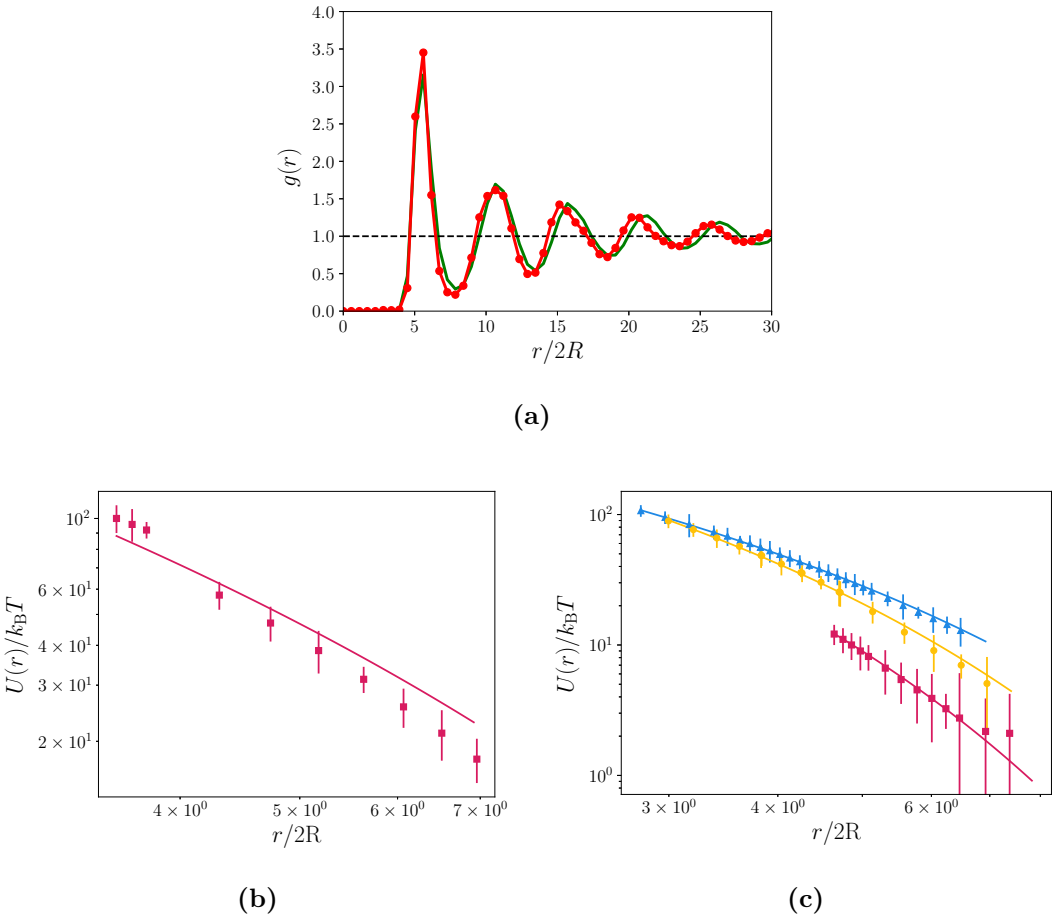

Figure 3.11 *(a) Comparison of experimental (red line, ◯) and simulated (green line, △) $g(r)$ for PHSA-PMMA at a dodecane-water interface at $\phi = 2.48\,\%$. (b) and (c) Energy profiles for PHSA-PMMA when in bulk dodecane (b) and adsorbed to a dodecane-water interface (c) measured using a blinking optical trap. r is core-to-core separation and R is the particle radius; different symbols/colours correspond to different particle pairs. The solid lines are best fit lines to a screened Coulomb potential (equation (3.16))*

described by a single screened monopole, seen from $g(r)$ inversion using the OZ inversion scheme, direct measurements using a BOT, and excellent agreement between experimental $g(r)$ and $g(r)$ obtained from simulations using a single screened monopole interaction. The fits are consistent with the theory described in § 3.3.

The question remains: where does the point charge required for the theory arise? There is strong evidence for the PLMA-PMMA particles having negligible charge in both oil and water phases. In the oil phase the BOT results confirm there is only a very weak interaction. The evidence for the particles being uncharged in

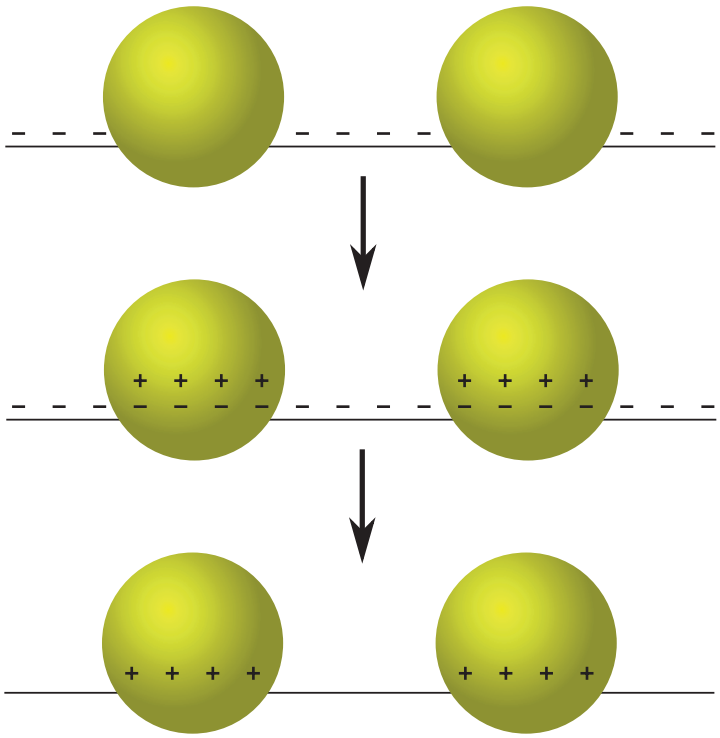

Figure 3.12 *Schematic representation of the idea of colloidal particles acting as neutral holes in the charged plane of the interface. An uncharged particle in a surface of negative charge can be considered as the superposition of an equal magnitude of positive and negative charge to match the surface charge density of the interface. Subtracting the negative plane leaves behind positively charged "holes". The theory of neutral holes applies to in-plane interparticle interactions and will not apply to any interaction out of the plane of the interface.*

water is twofold: 1) the particles are not stable in water, any attempts to disperse the particles in water have been unsuccessful - if the particles were charged, a charge stabilisation mechanism would allow the particles to disperse, and 2) the chemical structure of the PLMA stabiliser does not appear to feature any dissociable groups, so there is no obvious mechanism for the particles to charge in water. To the best of my knowledge, there is currently no theory which could predict a long-range repulsion for uncharged particles at a liquid interface. Here, I suggest that the charge leading to a Coulombic repulsion is the charge of the interface itself, with the particles then acting as repulsive "neutral holes" in the charged plane of the interface. A schematic representation of this idea is shown in figure 3.12.

It is known that water-alkane interfaces can become charged [93–96], and further, my measurements of the zeta potential of dodecane droplets in water give -65 ± 13 mV, which is in line with measurements made by Marinova *et al.* [93].

Invoking superposition at the level of the Poisson equation, we can consider that an array of neutral holes on a charged sheet will behave as an array of charged holes on a neutral sheet as far as in-plane interactions are concerned (neglecting the homogeneous electric field perpendicular to the interface as it does not contribute to the pair interaction). The holes will have an effective charge given by $Q_{\text{eff}} = a\sigma$, where a is the cross-sectional area of the particle at the interface and σ is the surface charge density of the bare liquid interface. The interparticle interaction should then be described by equation (3.9) with $Q = Q_{\text{eff}}$ as described.

While my results seem to contradict the literature on charge stabilised particles, it is in line with the theory outlined in § 3.3, where the dipolar contribution would be "squeezed out" by a screened monopole at low separations and a screened $\frac{1}{r^2}$ at high separations. It is worth noting that, for this system, the interaction strength falls to $< 1\ k_{\text{B}}T$ at separations around 15 μm. For a system of water ($\kappa^{-1} \sim 1\ \mu$m) and dodecane ($\kappa^{-1} \sim 10\ \mu$m), the theory predicts the crossover between the screened monopole term dominating and the screened $\frac{1}{r^2}$ term dominating occurs at approximately 10 μm [84]. This observation aligns with the screened monopole consistently providing the best fit to the experimental data. There are two reasons for this: 1) the Bayesian analysis provides a penalty for introducing more fitting parameters (in the spirit of Occam's razor), and 2) the greater number of data points in the region $r < 10\ \mu$m. In addition, the screened $\frac{1}{r^2}$ term providing a better fit in the BOT data at $r > 7\ \mu$m also aligns with this theory.

It is worth remarking on the difference in fits between $g(r)$ inversion using the OZ scheme and direct measurements of $U(r)$ using a BOT. Park, *et al.* [53] observed the same difference in the two measurement techniques. They claim that the difference stems from the fact that the ensemble averaged interaction is dominated by the particle pairs with low interactions. Therefore any heterogeneity in the particle batch (e.g. contact angle, particle size, stabiliser density) leads to a lower apparent interaction when finding $U(r)$ via an ensemble technique.

There is a consideration to be made for the physical sense of the fitting parameters when comparing the screened monopole and the screened $\frac{1}{r^2}$ models. As discussed, the screened monopole provides a (marginally) better fit than the screened $\frac{1}{r^2}$, but the latter provides fitting parameters that are physically more consistent. For example, screened-monopole fits result in values for A and κ that change non-monotonically with increasing salt concentration in the aqueous phase (see Table 3.3). On the contrary, fits using the screened $\frac{1}{r^2}$ model result in $6.0 <$

$\kappa^{-1} < 6.5$ μm and a monotonically decreasing value for A upon increasing salt concentration from 0 to 1.0 M (see Table 3.4). This is in line with results from the literature measuring the zeta potential of the bare water/oil interface at varying salt concentrations [93, 95]. In these works the absolute value of the zeta potential decreases upon addition of salts, this indicates that the magnitude of the surface charge decreases which, in the neutral holes theory, would decrease the interaction between two interfacially adsorbed particles. To consolidate this, the results from varying the pH of the subphase indicate that, in the neutral holes theory, the interface acquires a negative charge such that the isoelectric point is somewhere below pH 7. This can be seen in the relative lack of order in $g(r)$ curves taken at pH below 7 compared to the $g(r)$ curve taken at pH above 7 (see Figure 3.10). This aligns well with the measurement of the isoelectric point from [95] of dodecane droplets in water at pH$\sim$2.

In each case, the screening length differs from the assumed screening length of the bulk phase in question. In the screened monopole case I measure $\kappa^{-1} \sim 3$ μm where I expect to measure $\kappa_{\mathrm{w}}^{-1} \sim 1$ μm, and in the screened $\frac{1}{r^2}$ case I measure $\kappa^{-1} \sim 6$ μm where I expect to measure[8] $\kappa_{\mathrm{oil}}^{-1} \sim 10$ μm. It could be that the ionic density is subtly different near the interface than far from the interface leading to a modification of the apparent screening length. Notably, the screening length of water at the salt concentrations used here is expected to be orders of magnitude lower than what has been measured. For instance, at a concentration of 1.0 M NaCl, Debye Hückel theory predicts a screening length in water < 1 nm. These considerations indicate that, for the $g(r)$ data, the interaction is dominated by a screened $\frac{1}{r^2}$ propagating through the oil phase, as κ_{oil} features in the $\frac{1}{r^2}$ term in equation (3.9).

I will now consider the results when measuring the interaction of PHSA-PMMA particles, both in bulk dodecane and at a water-dodecane interface. Firstly, I have shown that these particles do not behave as hard spheres in dodecane (figure 3.11b). However, while they have a relatively long range interaction (compared to the particle size), the charge on the particles can be found from fits of the bulk BOT data to be much lower than charge stabilised systems previously reported in the literature, e.g. [8, 9]. So, while a charge stabilised system would expect to interact with a dipolar repulsion when attached to the interface, here I still measure a screened monopole as I do with PLMA-PMMA.

[8]Based on BOT results from PHSA-PMMA

Nevertheless, there is some evidence the potential for PHSA-PMMA particles at an interface is subtly more complicated. The poor comparison between simulated and experimental $g(r)$ at large r can indeed be improved by adding a small dipolar term to the simulation. There is no evidence from a theoretical standpoint that this dipolar term is the correct form to use however. All that I can confidently infer from this is that the interaction is slightly more complex than a single screened monopole, possibly due to the presence of charges at the particle-oil interface. However, it remains true that the interaction between these particles is best described by a single screened monopole, which aligns with the theory of neutral holes in a charged plane acting as point charges between two dielectric media with finite screening lengths.

3.7 Conclusion

In conclusion, I have experimentally shown that sterically stabilised, nearly hard-sphere PLMA-PMMA particles exhibit a long range repulsion when attached to an oil-water interface. I have also demonstrated that this interaction can be altered by changing the salt concentration or the pH in the aqueous phase and by changing the steric stabiliser of the colloidal particles. Quantitatively, the long-range repulsion observed has a negligible unscreened-dipole contribution (Tables 3.1 and 3.2) instead my data is better described by a screened Coulomb potential with an effective screening length. I attribute this long-range interaction to the particles acting as neutral holes in the charged plane of the water-oil interface. Hence, I have also fitted my data to recent theoretical results for the interaction between point charges at a dielectric interface. This fit is marginally worse than the screened-monopole case, but it provides fitting parameters that are physically more consistent, especially when considering the addition of salt to the aqueous phase.

I have also presented measurements for PHSA-PMMA particles at a water-oil interface. At relatively small interparticle separations, r, the data is consistent with the interaction between neutral holes in a charged plane. At larger r, the data suggests that an additional contribution to the interaction potential is required, which is in line with my optical-tweezer measurements that indicate that these PHSA-PMMA particles are slightly charged in bulk dodecane.

The generic point of these results is that, while existing models for particles

at liquid interfaces consider the charge at the particle-water and/or particle-oil surfaces [8, 9], the charge of the liquid interface cannot, in general, be ignored. Notably, this statement applies to any Pickering system where the fluid-fluid interface has a charge, not an unlikely scenario given [93–96].

Chapter 4

Structural Behaviour of a Bimodal Distribution of Interfacial Particles

4.1 Abstract

I have performed Monte Carlo simulations to observe the structural behaviour of a particle-laden interface with a bimodal distribution of particle sizes. The distribution is such that the large particles have a radius twice the size of the smaller particles, while the concentrations of small and large particles are varied with the concentration of small particles always being greater than the concentration of large particles. The particles interact via a screened monopolar potential as determined in Chapter 3. Following the neutral holes theory, the effective charge of the particles in the interaction potential is proportional to the cross-sectional area of the particles. While well ordered structures have been measured in the literature for particles interacting with a dipolar potential, my simulations show that particles interacting with a weaker, screened monopolar potential show no such long-range order. I also find that the deposition method of the particles plays a role in the final structure of the interface, which I will show in Chapter 5 has important consequences for the rheology of an interface. At low surface fraction, a sequential deposition of particles leads to greater local order as measured by the bond orientational order parameter. On the other hand, at a higher surface fraction a one-step deposition of particles leads to greater local order. I argue that this difference arises because the one-step deposition leads to domains of larger particles, which have greater short-range order. The ensemble of

particles cannot then rearrange to a structure with the larger particles exhibiting some longer range structures at higher surface fraction due to crowding effects.

4.2 Introduction

Previously, in Chapter 3, I investigated the interactions between a monomodal distribution of interfacially adsorbed colloidal particles. In this chapter, I will describe an extension of this model which introduces the added complexity of a bimodal system, i.e. a system of both large and small particles in a well defined ratio. Ideally, this would have been done experimentally, emulating the methods outlined as part of Chapter 3. However, due to the Covid-19 pandemic, these experiments have been replaced by Monte Carlo simulations.

In this Chapter, I take inspiration from literature experimental studies and observe how the deposition and surface fraction affects the final structure of a binary mixture of interfacial particles. I use Monte Carlo simulations with particles interacting via the screened monopolar interaction described in Chapter 3 and [75] at varying relative concentrations of small and large particles. I find that these particles do not form structures which are as ordered as those observed in the literature for particles interacting via a dipolar potential, which I attribute to the weaker, screened interaction that the particles are subject to here. I mimic both one-step and sequential deposition methods described in previous experimental studies and observe that the deposition method alters the structure in two different manners. At low surface fraction, the sequential deposition leads to more local ordering while at higher surface fraction the sequential deposition leads to a more locally disordered state. I argue that this differing response arises due to a one-step deposition leading to regions of higher concentration of large particles which have greater local ordering than is observed for a sequential deposition.

4.3 Background

In recent years 2-dimensional binary colloidal mixtures have garnered attention due to their potential uses in photonic materials using charged colloidal particles [97], as superhydrophobic surfaces using a combination of hydrogel particles

and charged colloidal particles [98], in plasmonic materials using hydrogel colloidal particles with noble metal cores [99], or in materials with enhanced electronic properties using semiconducting colloidal particles [100]. The potential to alter the structural arrangement of these systems, for instance by controlling the relative number ratios of large and small particles, opens up a larger variety of structures than can be achieved with a system of particles of a single size which typically form hexagonal structures to minimise the system's free energy.

Theoretical investigations have shown that a wide array of structures can be produced by varying the relative concentrations of particles [101–103]. In such studies, they can either vary the interaction strength by varying the dipole moments of the particles directly [101] or by varying the size of particles which indirectly affects the dipole moments [102, 103]. In each case a host of different structures are found to satisfy the condition of minimising the energy of the system, where the ideal structure strongly depends on both the relative concentration of the particles and the relative interaction strength between the particles. Interestingly, in [103] they compare the structures they find to a similar phase diagram for hard discs [104] and observe that every structure which is stable for hard discs also appears to minimise the configurational energy for particles interacting with a dipolar repulsion. These structures occur at similar values for the particles' size ratio, z, in each case, termed "magic values". These magic values are the size ratio at which all neighbouring hard discs are in close contact in the close-packed unit cell for that particular structure. Examples of these structures are shown for low concentration and high concentration of small particles in figures 4.1 and 4.2 respectively.

In addition to "magic values" of size ratio, molecular dynamics simulations have also shown that there are only specific number ratios of particles which lead to equilibrium crystallinity [105]. In these simulations, the large particles are first placed on a hexagonal lattice before the small particles are evenly distributed in the remaining space. The results show that a particle number ratio of 2 small particles for each large particle leads to a well defined crystal where the large particles sit on a hexagonal lattice (e.g. figure 4.2(a)), each having 6 surrounding smaller particles in the interstices. Similarly, a ratio of 6 small particles for each large particle leads to a similar structure but now with 12 small particles surrounding each large particle (e.g. figure 4.2(j)). In each of these cases the smaller particles sit in interstices primarily as far away from large particles as

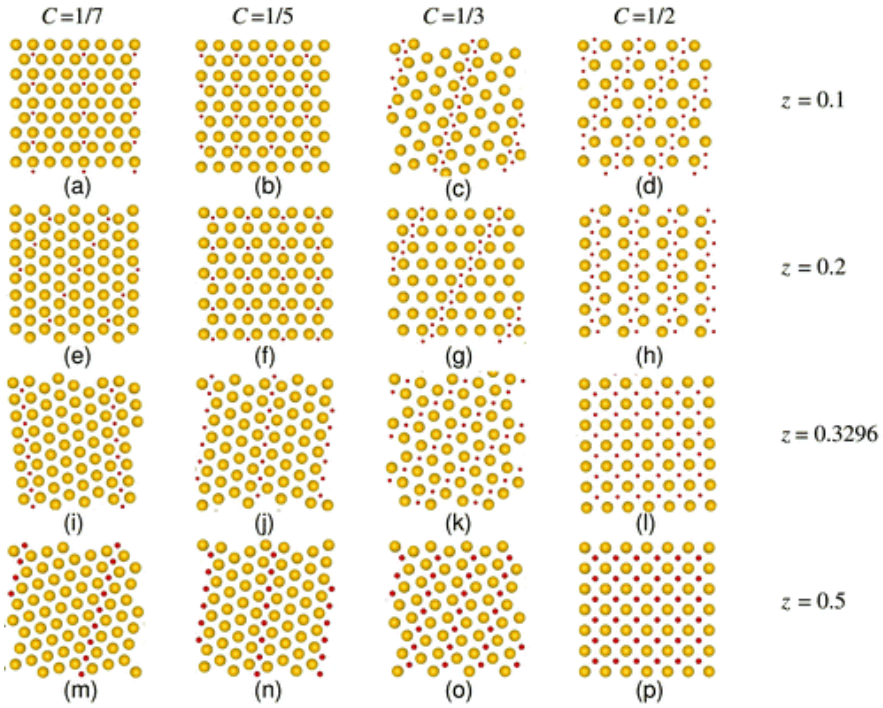

Figure 4.1 *Minimum energy conformations calculated theoretically for a bimodal distribution of particles interacting via a dipolar potential. C, the concentration of smaller particles, is varied and restricted to be less than 0.5. The particle size ratio, z, is also varied. Reproduced from Ref. [102] with permission from The Royal Society of Chemistry.*

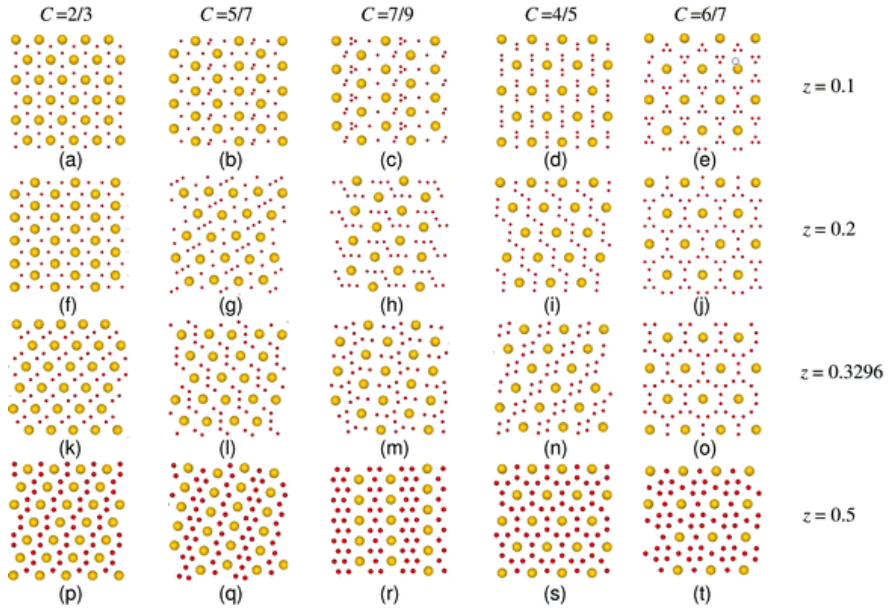

Figure 4.2 *Minimum energy conformations calculated theoretically for a bimodal distribution of particles interacting via a dipolar potential. C, the concentration of smaller particles, is varied and restricted to be greater than 0.5. The particle size ratio, z, is also varied. Reproduced from Ref. [102] with permission from The Royal Society of Chemistry.*

possible, and only once this condition is met do the smaller particles separate from each other. From this it is observed that the large particles control the long range nature of the configuration. In contrast, when the system has 7 small particles for each large particle, the large particles are forced into a disordered state as it becomes impossible for the small particles to be evenly distributed between the large particles - note that in this case the initial arrangement of particles is a random distribution. In addition, while the strength of the interaction has a minimal role in the final structure of the crystalline configurations, for the 7:1 ratio, some long range hexagonal order is observed for a strongly interacting system, while any long-range order is lost for a weakly interacting system. In the weakly interacting regime there is some evidence of phase separation, where the small particles form "rafts" with short range hexagonal ordering.

In the cases described above, the system is considered to be at zero temperature such that the problem can be considered purely through energy minimisation, however clearly finite temperature effects will play a key role in the structure of these systems experimentally. Monte Carlo simulations have been employed at varying temperatures to probe the melting behaviour of 2d binary crystals [106] and the results were compared to structures which minimise the energy and would

be present at zero temperature. The results show that the melting behaviour of these systems is unexpectedly complex. For instance, for binary hexagonal phases with 2 (AB_2) or 6 (AB_6) small particles for every large particle, the melting temperature was found to be three orders of magnitude larger than a phase with 5 small particles for every large particle (AB_5). The authors suggest that the difference in melting temperatures arises as the AB_2 and AB_6 structures melt in a two-stage process: first the small (B) particles become disordered while the large (A) particles maintain long-range hexagonal order, then the system melts into an entirely isotropic phase. On the other hand, the melting behaviour of the AB_5 crystal proceeds first via a melt into a semi-disordered phase with local AB_6 order, then proceeding in the same manner as for the AB_6 crystal. It is noteworthy that the simulations here are performed with the initial conditions being the crystals which minimise the energy, as determined by a lattice sum method, rather than a random distribution of particle positions which may be more relevant for certain experimental methods or weakly interacting systems such as those described in Chapter 3.

So far I have described work considering particles with a dipolar interaction, which is relevant for charged particles at liquid interfaces [7–9], however the interaction between the particles I use throughout this thesis can be described by a screened monopolar potential. Theoretical work has also considered colloidal mixtures in 2d which interact as monopoles. In one study, two equally sized particles are placed in an external field where each type of particle exhibits an opposite effect to that field [107]. This study restricts the mixture to having an equal number of each type of particle and the monopolar interaction between particles is independent of the particles' interaction with the external field. Here, the particles do not form long-range crystalline structures, however the particles do self-assemble into well defined "lanes". The lack of crystalline order is left unmentioned, but may arise due to the effective temperature being above the melting transition or the surface fraction being low enough that the typical interparticle energy is relatively low.

On the other hand, another study considering a binary mixture of particles interacting with a screened monopole potential does focus on 2d crystalline structures [108]. Here, two parameters are varied, the relative charge and the relative concentration of each particle type. Similarly to a study from the same group on stable crystalline lattices with a dipolar potential, there are a rich variety of phases which have been shown to be stable. At a large charge asymmetry

(charge ratio $\lesssim 0.2$) there is a particularly large variety of structures found, similar to the results of a dipole potential, with a lot of the same structures present. However, there are definite differences, both in the position of the phases in the phase diagram and some of the determined structures at a charge/dipole moment ratio $\gtrsim 0.5$. The investigation into the monopolar potential involved probing different surface pressures, with fewer possible crystal structures at progressively lower pressures, which may be experimentally relevant for surfaces with a variable surface concentration as this is closely linked to surface pressure [49, 109].

In the past ten years, significant progress has been made in experimentally producing monolayers of binary colloids, see Figure 4.3. The first report of long-range order in an experimental system produced binary monolayers of hydrophobic silica particles adsorbed at an octane-water interface [110]. As discussed in Chapter 3, charge stabilised particles have been reported as interacting with a dipolar repulsion [8], and it is shown, both in [111] and [110], that the particles used in [110] exhibit the same interaction. Upon a bimodal distribution of these particles adsorbing to the octane-water interface, structures in agreement with zero temperature calculations were observed, where the large and small particles were 3 μm and 1 μm in diameter. Additionally, Monte Carlo simulations were performed to compare finite temperature effects to experimental results. Here, it was found that certain structures, while being minima in the energy landscape, do not form at finite temperature due to thermodynamic effects. They show that this is a thermodynamic effect rather than a kinetic effect (i.e. the system may get stuck in a glassy state) by starting the simulations from the theoretically determined minimum energy configuration. However, while Monte Carlo simulations reveal no AB_5 structure (which would minimise the energy) at the appropriate experimental concentration, unit cells of AB_5 and AB_6 are observed to coexist.

Other experimental studies found less evidence of long-range ordered structures when charge stabilised particles adsorb to a water-oil interface in one step [112]. Interestingly, regardless of the relative concentrations of small and large particles, the authors note that no phase separation was observed. However, the results are at odds with the crystal structures found in [110], indicating that the structure may be sensitive to the experimental conditions, such as the interfacial loading process. Contrasting this, when the particles are sequentially deposited on the interface, i.e. first the larger particles are deposited, allowed to equilibriate, then the smaller particles are deposited, the particles form ordered binary structures

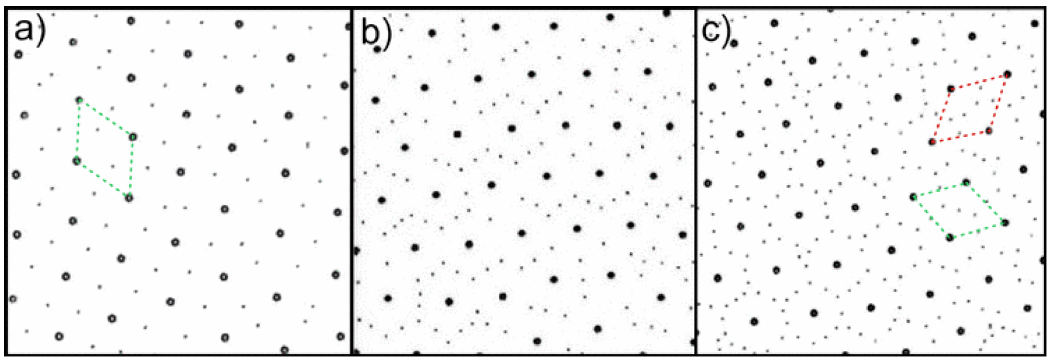

Figure 4.3 *Structures of binary monolayers of hydrophobic silica particles at an octane-water interface. The number concentration of smaller particles (relative to the total number of particles) is (a) 2/3, (b) 3/4, and (c) 5/6. The average separation between large particles is 28 μm, while the large and small particles radii are 3 μm and 1 μm respectively. The rhombi highlight AB_2 (a), AB_5 (c, lower green), and AB_6 (c, upper red) unit cells. Reproduced from Ref. [110] with permission from the American Physical Society.*

such as those predicted in theoretical studies that I have discussed [113].

Thus far I have only discussed purely repulsive potentials. Using oppositely charged particles in mixed monolayers leads to interesting results, especially contrasting the effects of a one-step or sequential deposition. In this instance, the one-step process resulted in aggregation and subsequently gel-like structures at high particle type asymmetry. In the two-step sequential loading the particles formed large distinct crystalline domains, i.e., there was phase separation, with the boundary being a chain of alternating positive and negative particles [114].

The previous work in the literature that I have discussed here shows that the field of binary mixtures of particles in a 2d setting is rich for study, however, there remains a lack of work investigating particles interacting with a screened monopolar interaction, both experimentally and theoretically. Additionally, theoretical work on bimodal systems has primarily focussed on zero temperature calculations, which may not be experimentally relevant for weakly interacting particles, such as those described in Chapter 3 [75].

4.4 Methods

4.4.1 Simulation Algorithm

Monte Carlo simulations were performed with a bimodal distribution of particles interacting with the screened monopolar interaction determined using the RMC method in Chapter 3 for PLMA-PMMA. Here I will describe in detail the algorithm for the simulation as well as the initial conditions used.

For the Monte Carlo simulation a Metropolis algorithm is used. Consider the configuration in a state labelled by μ at step m. A new configuration, ν, is generated where one particle is randomly chosen and its position is changed by a fixed distance δx and an angle $\delta\theta$, taken from a uniformly random distribution. The energy of configuration μ is determined by:

$$U(\mu) = \sum_{i=1}^{N_p-1} \sum_{j=i+1}^{N_p} R_i^2 R_j^2 \frac{A}{r_{ij}} e^{-\kappa r_{ij}}, \tag{4.1}$$

where $r_{ij} = |\vec{r_i} - \vec{r_j}|$, i and j label individual particles, and N_p is the number of particles in the system. R_i and R_j are the ratio of a particle's radius to the smaller particle's radius ($R_s = 1, R_l = 2$), such that the interaction prefactor is modified to represent the difference in area of interface cut out in the neutral holes model, i.e. A becomes $R_i^2 R_j^2 A$. In other words, the interaction between two large particles is R_l^4/R_s^4 larger than the interaction between two small particles as the effective charge Q_{eff} is proportional to the cross-sectional area.

The change in energy between states μ and ν, $\Delta U = U(\nu) - U(\mu)$, can then be determined. At step $m+1$, the new configuration ν is accepted with a probability

$$p = \min\{1, e^{-\Delta U}\}, \tag{4.2}$$

where upon rejection the configuration remains as μ. To implement this probability, a random number, k, is sampled from a uniform distribution between 0 and 1 and the move is accepted if $k \leq p$.

Note that in the calculation of the acceptance probability, p, we have set the thermal energy $k_{\text{B}}T$ to 1, which is equivalent to calculating ΔU in units of $k_{\text{B}}T$. This introduces a more general discussion of simulation units. The interparticle potential used - i.e. the parameter values of A and κ - was determined

experimentally using particles of radius 1.2 μm. The particle radius used in the simulation was set as 0.05 for the smaller particles, therefore a distance of 1 in simulation units is equivalent to 24 μm.

I also consider the length of one simulated time step. One simulation time step is fixed by the number of attempted moves in a sweep, regardless of whether these are accepted or rejected, which is the number of particles in the system, N_p. Note that the particle chosen to move at each step is randomly determined such that there is a very large probability that the same particle is moved more than once in one time step[1]. This allows me to determine how long one time step is relative to the diffusive behaviour of the system. If there were one particle in the simulation every step would be accepted and the particle would move δx per time step in a 2 dimensional random walk. Now, the distance moved in a 2 dimensional random walk is given by:

$$x(t)^2 = 4Dt, \tag{4.3}$$

where D is the diffusion constant of the system. Therefore, in simulation units

$$\delta x^2 = 4D\delta t, \tag{4.4}$$

which allows me to determine the length of one time step in SI units as

$$\delta t = \frac{\delta x^2}{4D}. \tag{4.5}$$

In my simulation, δx is set to 0.01 simulation units, or 0.24 μm. Using the value for diffusion constant of similar particles in [10], 0.10 $\mu m^2 s^{-1}$, the length of one time step is therefore found to be 0.144 s. It is useful to note that this value for diffusion constant is for particles of radius 0.5 μm, whereas the particles modelled here have a radius of 1.2 μm for the smaller particles and 2.4 μm for the larger particles. Note also that in the simulations performed here δx is the same for the smaller and larger particles, whereas the diffusion constant should be proportional to $1/R$, where R is the particle radius. However, for the purposes of this work the most important aspect is that a simulation timestep is much shorter than the Brownian time, the average time taken for a particle to diffuse its own diameter, which for these particles is ~ 10 s.

After the initial conditions are set, particle positions are output after 200 timesteps for the system to equilibriate, and then subsequent particle position

[1]In fact, when the number of particles is $\sim$100, this is practically guaranteed

data are output every 1000 timesteps to ensure there is no correlation between timesteps. The time to equilibrium is equivalent to ~ 30 s, i.e. much longer than 1 Brownian time. 1000 particle position datasets are found to mimic experiments such as those performed in Chapter 3 where data is averaged over many frames.

Initial conditions are set in one of two ways. The first method is every particle is assigned a random starting position[2], independent of the particle's size. The second method mimics methods to create bimodal arrays in experimental studies [113]; firstly, the large particles are assigned a random starting position before they are allowed to equilibriate over 200 timesteps. Subsequently, the small particles are assigned random starting positions and given 200 timesteps to equilibriate before measurements are taken.

The simulations were run for 10 different ratios of large to small particles, $n = N_{\text{large}}/N_{\text{small}}$; $n = \{0.125, 0.143, 0.16666, 0.2, 0.25, 0.286, 0.33, 0.5, 0.667, 0.75\}$. Two different surface coverages were investigated, firstly the large particles were dispersed at a surface fraction of 5%, with the number of small particles added depending on the value of n. Secondly, the particles were dispersed such that the total surface coverage was 20%, regardless of the value of n. The number of large particles was fixed at 60, with the number of small particles determined by n and the size of the simulation box, L, determined by the surface fraction. The simulation was subject to periodic boundary conditions.

4.4.2 Analysis Methods

The 1000 snapshots from the Monte Carlo simulation were analysed by measuring $g(r)$:

$$g(r) = \frac{N_{\text{sim}}(r)}{N_{\text{rand}}(r)}, \tag{4.6}$$

where $N(r)$ is the number of particles separated by a distance between r and $r + \mathrm{d}r$, and 'sim' and 'rand' denote the simulated particles and a random distribution of particles. $g(r)$ were measured considering only large particles, only small particles, and the separations between large and small particles ($g_l(r)$, $g_s(r)$, and $g_{ls}(r)$). The analysis assumed periodic boundary conditions and avoided double counting particle pairs due to periodic boundary conditions by setting a

[2]Due to the repulsive potential and the initial time to reach equilibrium the particles do not need to be prevented from overlapping. In fact, in experiments one can imagine a particle depositing "on top" of another particle before being pushed aside.

maximum separation of $L/2$.

Additionally, the bond order parameter, ψ_6, was measured for the snapshots. This parameter measures local 6-fold symmetry of a system and can be calculated using:

$$\psi_6 = \frac{1}{N_n} \sum_{i=1}^{N_n} e^{i6\theta_{ij}}, \tag{4.7}$$

where j is the central particle, N_n is the number of nearest neighbours of the j^{th} particle, and θ_{ij} is the angle between the i^{th} and j^{th} particle relative to an arbitrary axis (chosen as the x-axis here). The nearest neighbours are found using a Delaunay triangulation from the `scipy` package in Python. Any neighbours separated by more than a threshold being discarded. The threshold was taken as 1.2 times the average particle separation. The magnitude of ψ_6, $|\psi_6|$, is a number ranging between 0 and 1, where a value of 0 denotes no local six-fold symmetry and a value of 1 denotes perfect local 6-fold symmetry[3].

4.5 Results

4.5.1 Lower Surface Coverage

I begin by showing simulated snapshots of the particle laden interface where the surface fraction is fixed such that the large particles occupy 5% of the area. Firstly, I note that there is little qualitative difference between the one-step deposition of particles (figure 4.4a) and the sequential deposition of particles (figure 4.4b).

One observation which can be made in the one-step deposition data is "lanes" of small particles between the larger particles at $n \geq 0.5$. "Lanes" such as these have been previously observed theoretically [102, 107] and experimentally in 3 dimensions for particles interacting with a screened monopolar potential driven in an external electric field [115]. Qualitatively, these "lanes" are less obvious in the results from a sequential deposition.

From series of these data, $g(r)$ are found for different pairs of particles, e.g. g_{ls} is

[3]Note that 2- and 3-fold symmetry will also return a value of 1

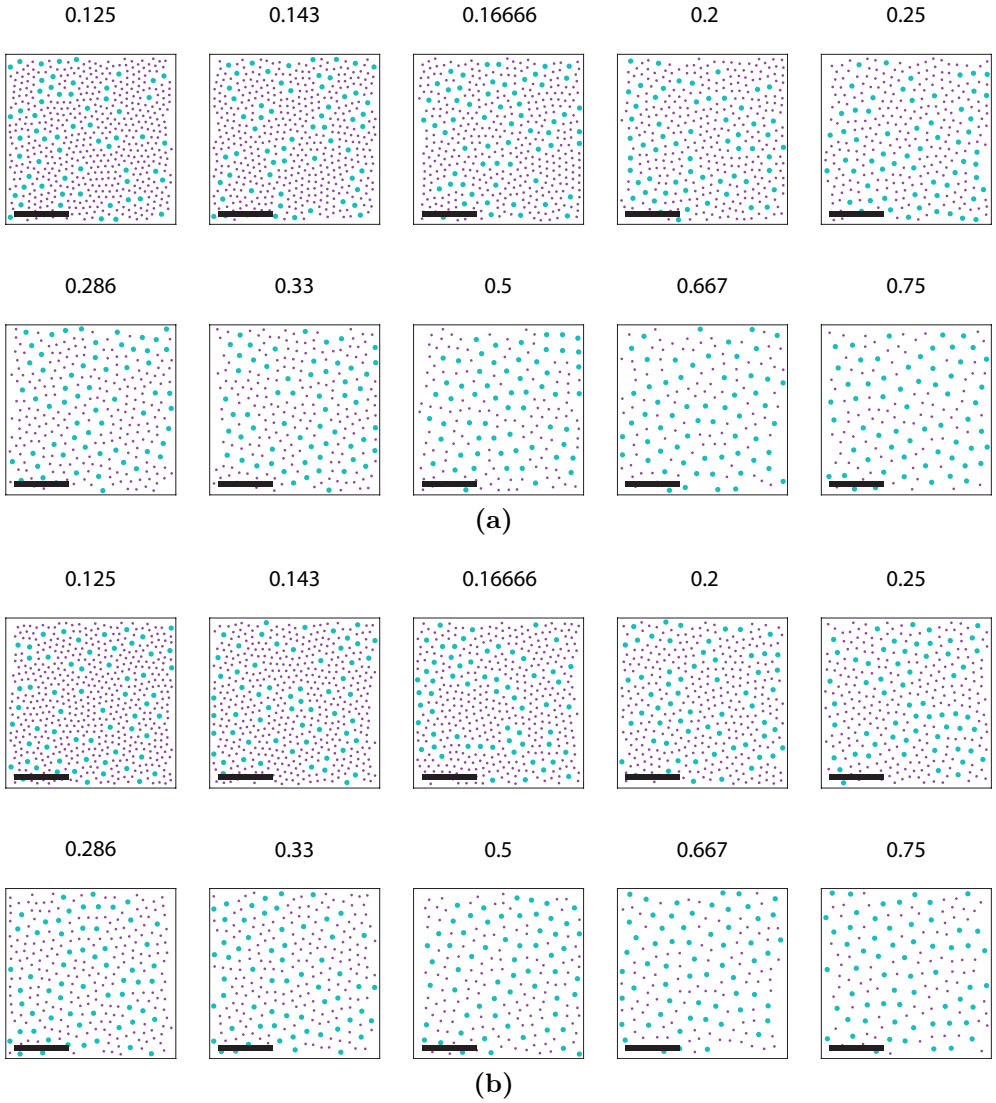

Figure 4.4 *Simulated snapshots of a bimodal distribution of large and small particles interacting with a screened monopolar potential. The number above each snapshot indicates the ratio of large to small particles. (a) Particles are deposited in a one-step process where each particle is initialised with a random position. (b) Particles are deposited in a two-step process, first large particles are randomised and allowed to equilibriate, before the small particles are initialised with random positions. The surface fraction of the large particles if 5%. Scale bars are 50 μm.*

the radial distribution function when only considering separations between large and small particles. Representative $g(r)$ ($g_{\mathrm{l}}(r)$, $g_{\mathrm{s}}(r)$ and $g_{\mathrm{ls}}(r)$) are shown for a relatively low n (figure 4.5) and a relatively high n (figure 4.6) for both initial conditions.

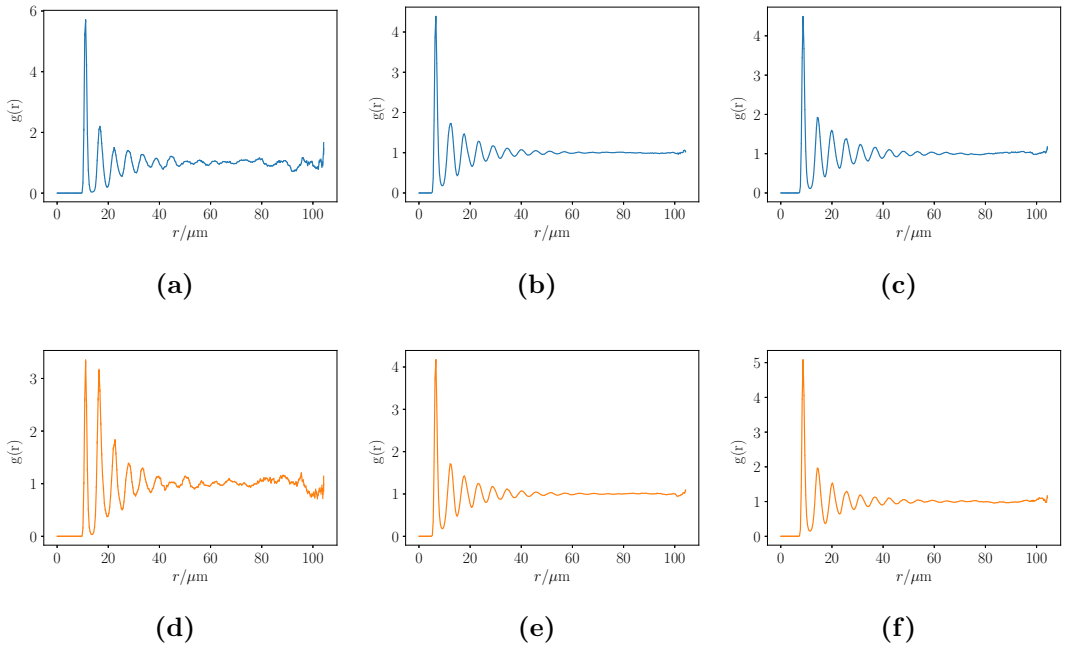

Figure 4.5 *$g(r)$ for simulations of a bimodal distribution of large and small particles at a ratio of 1 large particle for every 7 small particles ($n = 0.143$). The surface fraction of the large particles if 5%. Top row [(a), (b), (c)] is a one step deposition of particles, bottom row [(d), (e), (f)] is a sequential deposition of particles. (a), (d) $g(r)$ when only large particles are considered ($g_{\mathrm{l}}(r)$); (b), (e) $g(r)$ when only small particles are considered ($g_{\mathrm{s}}(r)$); (c), (f) $g(r)$ for the separations between large and small particles ($g_{\mathrm{ls}}(r)$).*

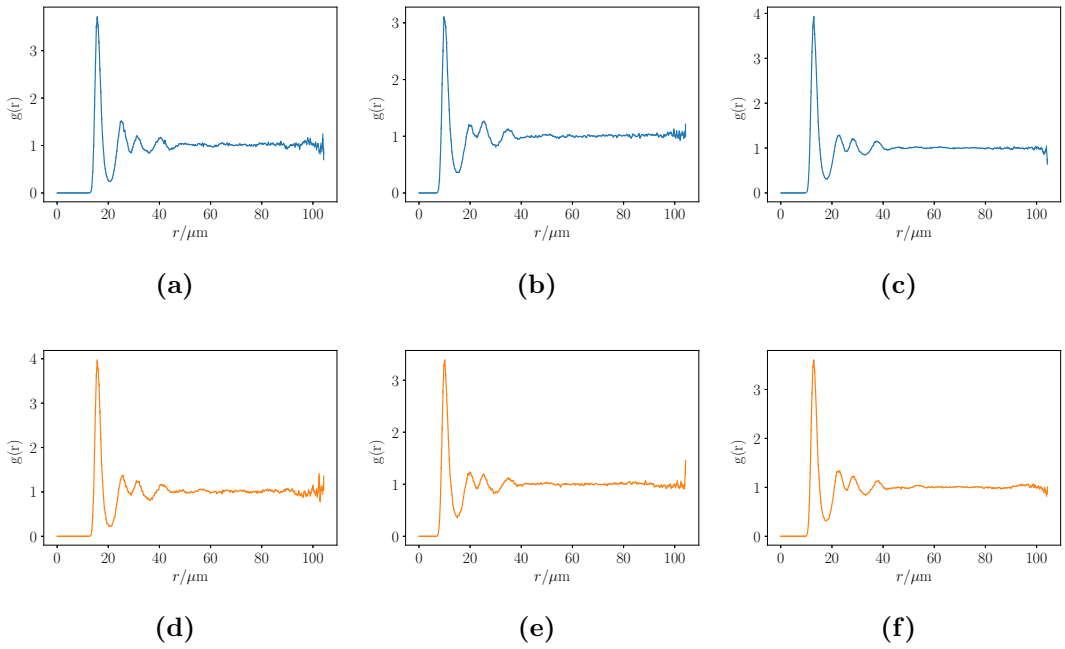

Figure 4.6 *$g(r)$ for simulations of a bimodal distribution of large and small particles at a ratio of 2 large particle for every 3 small particles ($n = 0.667$). The surface fraction of the large particles if 5%. Top row [(a), (b), (c)] is a one step deposition of particles, bottom row [(d), (e), (f)] is a sequential deposition of particles. (a), (d) $g(r)$ when only large particles are considered ($g_{\mathrm{l}}(r)$); (b), (e) $g(r)$ when only small particles are considered ($g_{\mathrm{s}}(r)$); (c), (f) $g(r)$ for the separations between large and small particles ($g_{\mathrm{ls}}(r)$).*

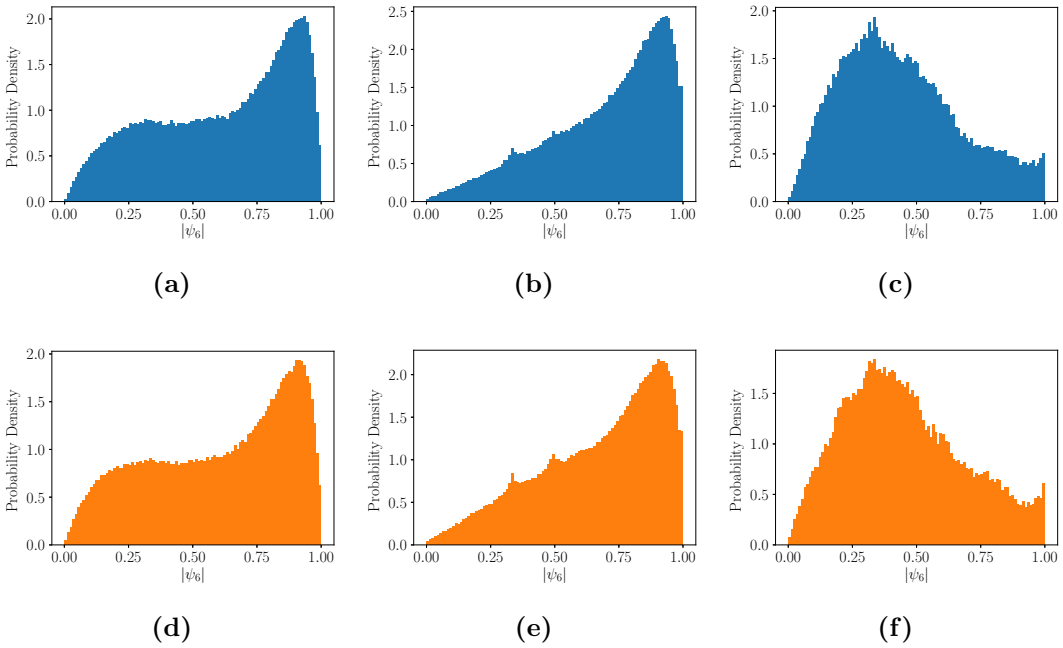

Figure 4.7 *Distribution of $|\psi_6|$ for simulations of a bimodal distribution of large and small particles at a ratio of 1 large particle for every 7 small particles ($n = 0.143$). The surface fraction of the large particles if 5%. Top row [(a), (b), (c)] is a one step deposition of particles, bottom row [(d), (e), (f)] is a sequential deposition of particles. (a), (d) when all particles are considered; (b), (e) when only small particles are considered; (c), (f) when only large particles are considered.*

There are a few things to note here. The deposition method plays a larger role than could be qualitatively observed, specifically in the arrangement of the larger particles which are more ordered in the sequential deposition method for low n; this is seen from the larger second and third peaks in $g(r)$ (figure 4.5a vs figure 4.5d). However, at higher n, there is less distinction between the two deposition methods. In every other $g(r)$ measurement there is little quantitative difference between the two deposition methods.

I now present the average bond order parameter over 1000 simulated frames. I show the probability distribution of $|\psi_6|$ which can range from 0 to 1. Figures 4.7 and 4.8 show representative histograms at different values of n and with different deposition methods in a similar way as the $g(r)$ presented; these present data considering all particles, considering only small particles and considering only large particles.

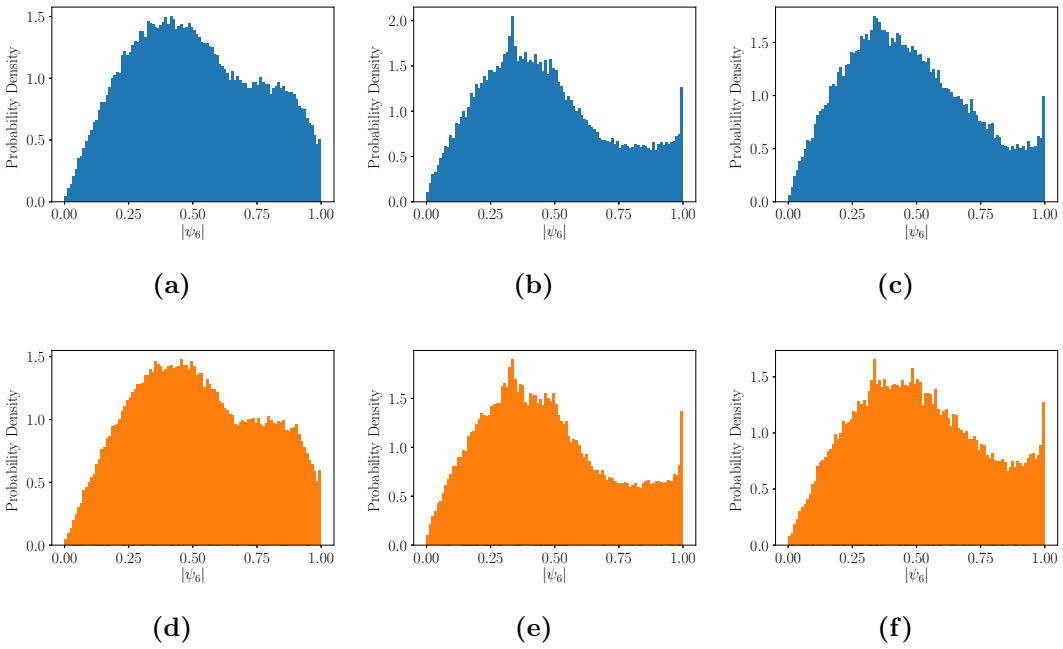

Figure 4.8 *Distribution of $|\psi_6|$ for simulations of a bimodal distribution of large and small particles at a ratio of 2 large particle for every 3 small particles ($n = 0.667$). The surface fraction of the large particles if 5%. Top row [(a), (b), (c)] is a one step deposition of particles, bottom row [(d), (e), (f)] is a sequential deposition of particles. (a), (d) when all particles are considered; (b), (e) when only small particles are considered; (c), (f) when only large particles are considered.*

At low n, where there is a high surface fraction of small particles, the bond order parameter peaks close to 1 when considering only the smaller particles. In contrast, the bond order parameter peaks at a much lower value, ~ 0.33 when only the large particles are considered. Finally note that there are two subtle peaks in the data when only considering the smaller particles at $|\psi_6| \sim 0.5$ and 0.33. When comparing the deposition methods, there is little difference between the one-step and sequential depositions. However, the secondary peaks at 0.33 and 0.5 are more pronounced in the sequential deposition.

At higher n, each of the probability distributions has a peak at 0.33, regardless of deposition method or which particle bonds are considered. Notably, when only considering small particles or large particles, there is a secondary peak at $|\psi_6| = 1$. Here, I can observe a difference between the deposition methods, where the peak at 1 is larger when the particles are deposited sequentially.

Considering these results together, I have also plotted a snapshot of the simulated interface with the particles colour coded to reflect their value of $|\psi_6|$, see figure 4.9. Despite the quantitative differences between the two deposition methods observed in $|\psi_6|$ or $g(r)$, it is difficult to note significant differences when looking at colour coded snapshots. The main notable feature is the high likelihood of smaller particles having a $|\psi_6|$ close to 1 when surrounded by other smaller particles, while the presence of the larger particles disrupts this symmetry.

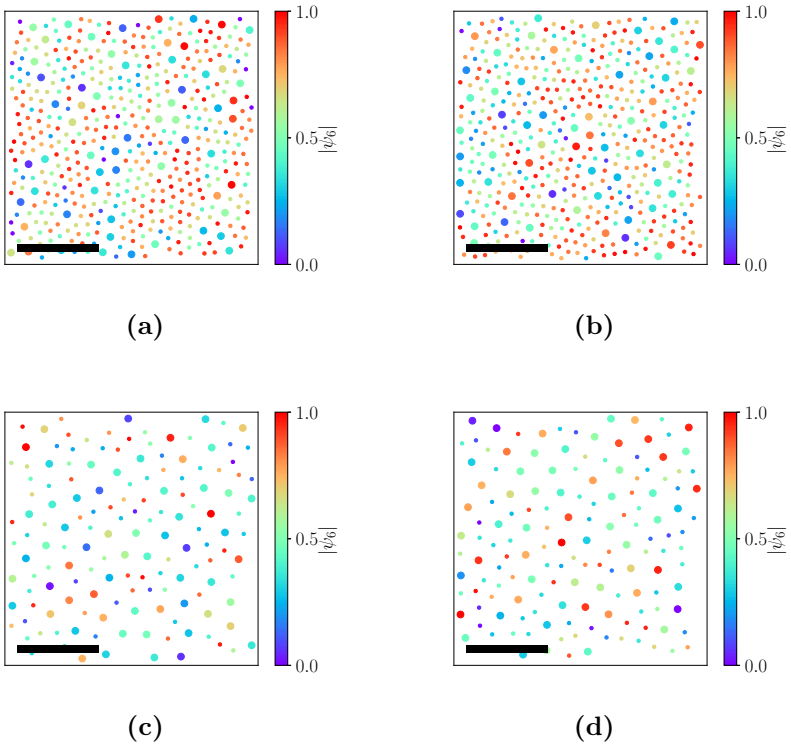

Figure 4.9 *Snapshots with each particle colour coded with the value of* $|\psi_6|$ *when considering only other particles of the same size. (a)* $n = 0.143$ *with a one step deposition of particles, (b)* $n = 0.143$ *with a sequential deposition of particles, (c)* $n = 0.667$ *with a one step deposition of particles, and (d)* $n = 0.667$ *with a sequential deposition of particles. In all cases the surface fraction of large particles is 5%.*

4.5.2 Higher Surface Coverage

Snapshots comparing the deposition method of particles at varying number ratios at a higher, fixed surface fraction of 20% again show little qualitative difference between the one-step deposition method and the sequential deposition method (figure 4.10). At high n the absolute difference in surface fraction between the simulations at lower and higher surface coverage is greatest[4], however, we can still observe "lanes" at this surface fraction. Above $n = 0.286$ we can begin to qualitatively observe some hexagonal ordering in the system.

Again, $g(r)$ are found for different pairs of particles, e.g. g_{ls} is the radial distribution function when only considering separations between large and small particles. Representative $g(r)$ ($g_{\mathrm{l}}(r)$, $g_{\mathrm{s}}(r)$ and $g_{\mathrm{ls}}(r)$) are shown for a relatively low n (figure 4.11) and a relatively high n (figure 4.12) for both initial conditions.

Similarly to the results at the lower surface fraction, there is a considerable quantitative difference in $g(r)$ between deposition methods when only large particles are considered, especially at the lower value of n, where larger secondary peaks indicate greater local order from a sequential deposition. At the higher n there is less difference in $g(r)$ and in fact the secondary peaks are slightly more pronounced in the one step deposition method.

[4]Because of the different methods of fixing surface fraction, the lower surface fraction results have a fixed fraction of large particles but a variable total surface fraction. At a high value of n these two measures have a larger difference.

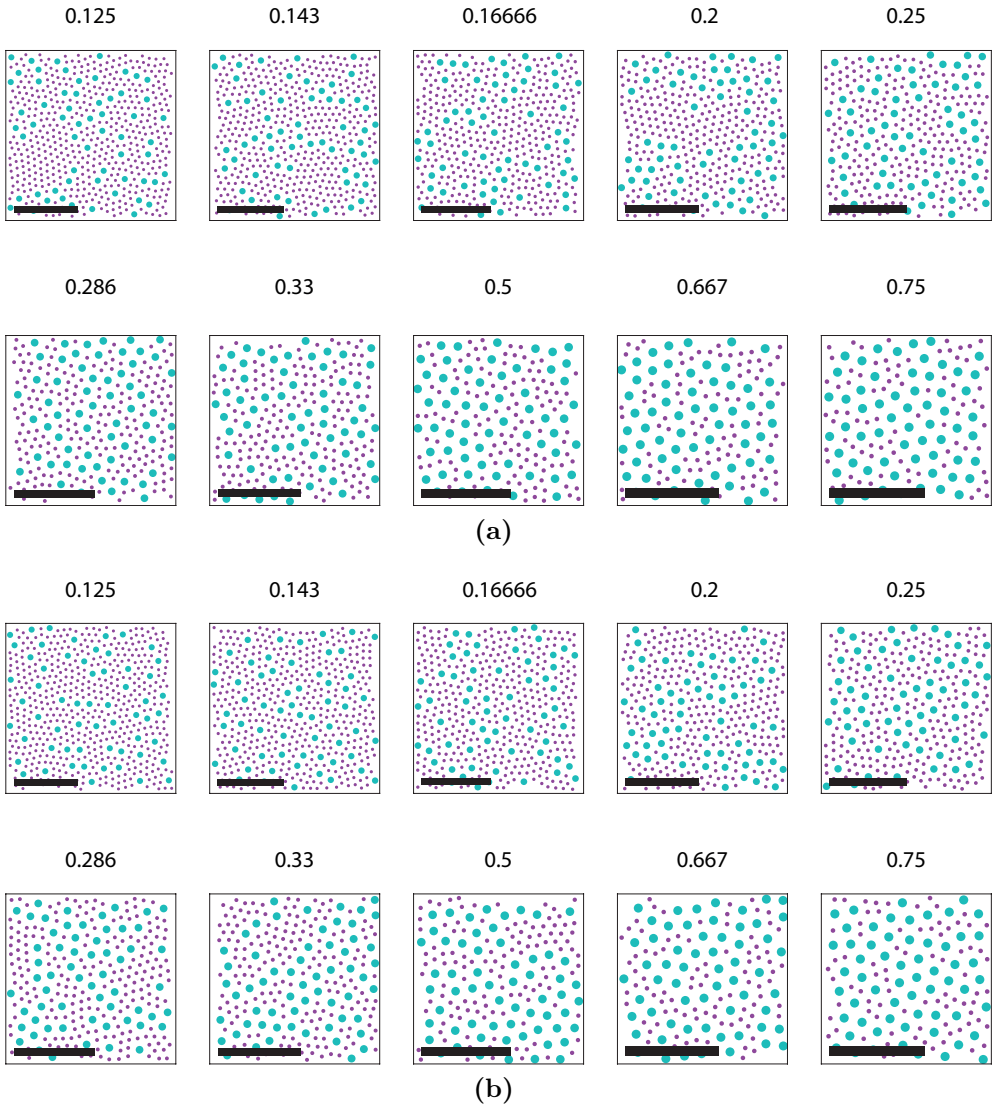

Figure 4.10 *Simulated snapshots of a bimodal distribution of large and small particles interacting with a screened monopolar potential. The number above each snapshot indicates the ratio of large to small particles. (a) Particles are deposited in a one-step process where each particle is initialised with a random position. (b) Particles are deposited in a two-step process, first large particles are randomised and allowed to equilibriate, before the small particles are initialised with random positions. The total surface fraction is 20%. Scale bars are 50 μm.*

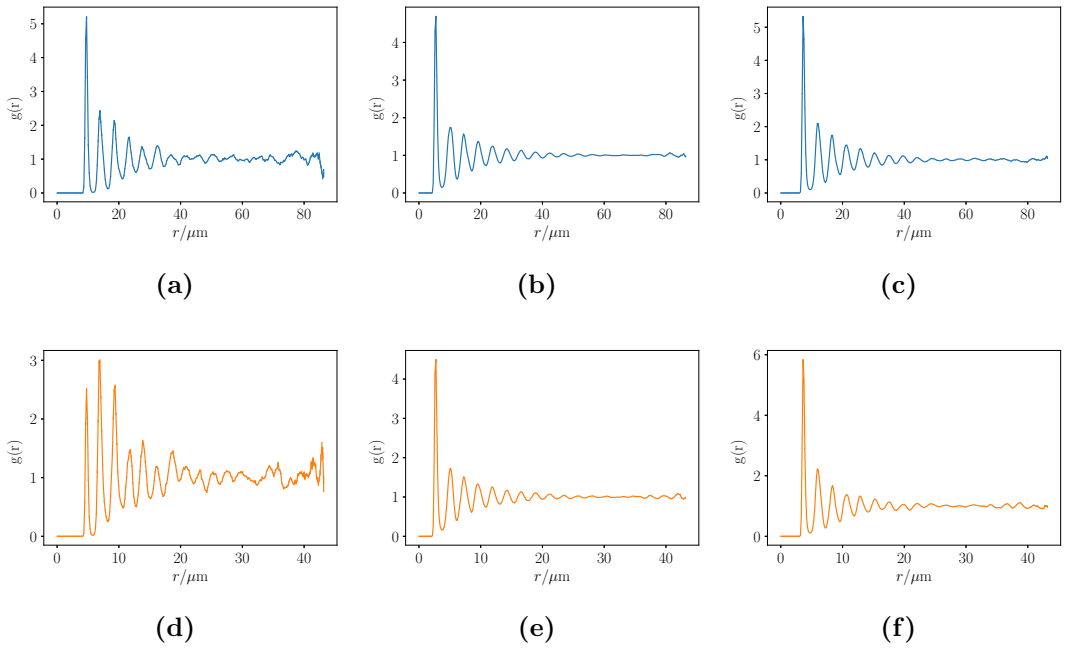

Figure 4.11 *$g(r)$ for simulations of a bimodal distribution of large and small particles at a ratio of 1 large particle for every 7 small particles ($n = 0.143$). The total surface fraction is 20%. Top row [(a), (b), (c)] is a one step deposition of particles, bottom row [(d), (e), (f)] is a sequential deposition of particles. (a), (d) $g(r)$ when only large particles are considered ($g_{\mathrm{l}}(r)$); (b), (e) $g(r)$ when only small particles are considered ($g_{\mathrm{s}}(r)$); (c), (f) $g(r)$ for the separations between large and small particles ($g_{\mathrm{ls}}(r)$).*

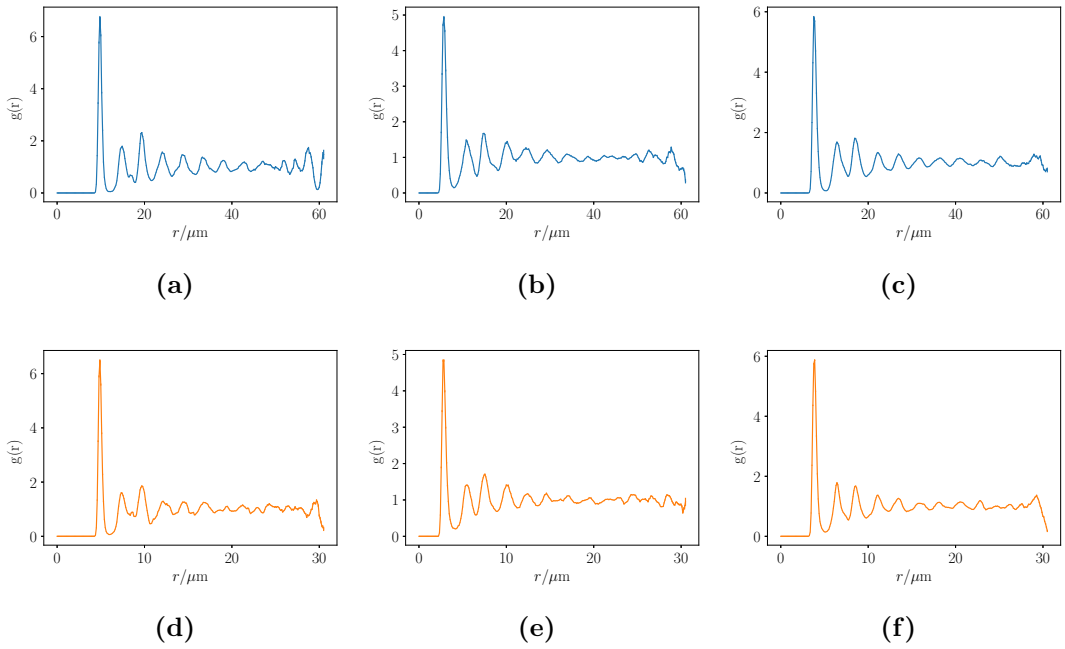

Figure 4.12 *$g(r)$ for simulations of a bimodal distribution of large and small particles at a ratio of 2 large particle for every 3 small particles ($n = 0.667$). The total surface fraction is 20%. Top row [(a), (b), (c)] is a one step deposition of particles, bottom row [(d), (e), (f)] is a sequential deposition of particles. (a), (d) $g(r)$ when only large particles are considered ($g_{\mathrm{l}}(r)$); (b), (e) $g(r)$ when only small particles are considered ($g_{\mathrm{s}}(r)$); (c), (f) $g(r)$ for the separations between large and small particles ($g_{\mathrm{ls}}(r)$).*

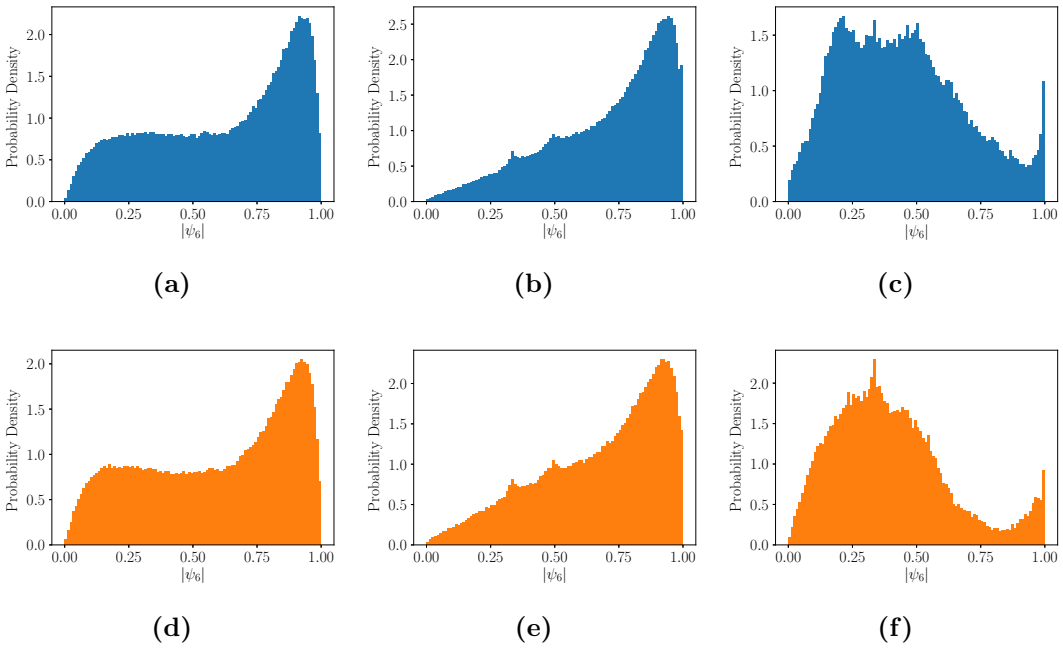

Figure 4.13 *Distribution of $|\psi_6|$ for simulations of a bimodal distribution of large and small particles at a ratio of 1 large particle for every 7 small particles ($n = 0.143$). The total surface fraction is 20%. Top row [(a), (b), (c)] is a one step deposition of particles, bottom row [(d), (e), (f)] is a sequential deposition of particles. (a), (d) when all particles are considered; (b), (e) when only small particles are considered; (c), (f) when only large particles are considered.*

Finally I present the average bond order parameter over 1000 simulated frames at the higher surface fraction. I show the probability density of $|\psi_6|$, where $|\psi_6|$ can range from 0 to 1. Figures 4.13 and 4.14 show representative histograms at different values of n and with different deposition methods in the same way as the $g(r)$ presented; these present data considering all particles, considering only small particles and considering only large particles.

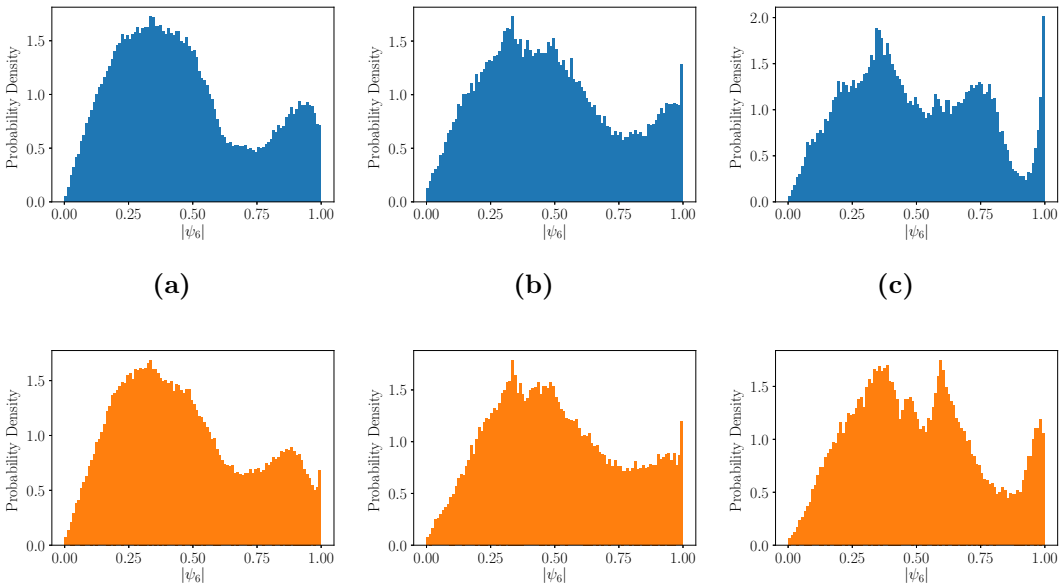

Figure 4.14 *Distribution of $|\psi_6|$ for simulations of a bimodal distribution of large and small particles at a ratio of 2 large particles for every 3 small particles ($n = 0.667$). The total surface fraction is 20%. Top row [(a), (b), (c)] is a one step deposition of particles, bottom row [(d), (e), (f)] is a sequential deposition of particles. (a), (d) when all particles are considered; (b), (e) when only small particles are considered; (c), (f) when only large particles are considered.*

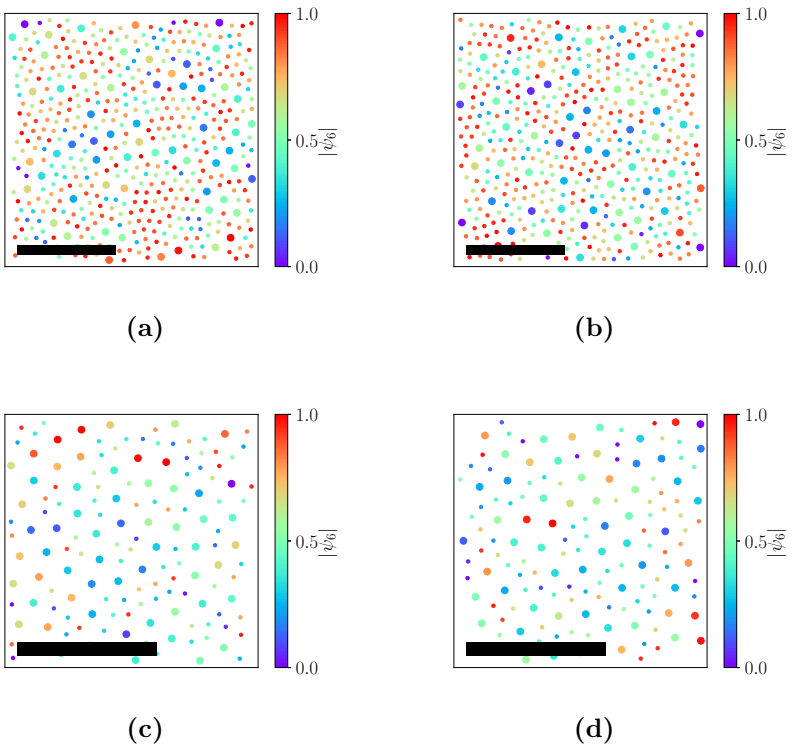

Figure 4.15 *Snapshots with each particle colour coded with the value of* $|\psi_6|$ *when considering only other particles of the same size. (a)* $n = 0.143$ *with a one step deposition of particles, (b)* $n = 0.143$ *with a sequential deposition of particles, (c)* $n = 0.667$ *with a one step deposition of particles, and (d)* $n = 0.667$ *with a sequential deposition of particles. In all cases the total surface fraction is 20%. Scale bars are 50* μm.

Similarly to the results at the lower surface fraction, there are peaks at or near 0.33, 0.5 and 1 in the different cases shown. Additionally, at the higher n, the distribution of $|\psi_6|$ when only large particles are considered exhibits some peaks ≥ 0.5 and < 1. Finally, the peak at 1 when considering only large particles is much more pronounced in the one-step deposition method rather than the sequential deposition method.

Considering these results together, I have also plotted a snapshot of the simulated interface with the particles colour coded to reflect their value of $|\psi_6|$, see figure 4.15. Again the main results are similar to those at lower surface fraction: it is difficult to ascertain features which would give rise to the observed differences in the $|\psi_6|$ distribution, and the smaller particles local structure is hexagonal when there are no larger particles nearby which disrupt the smaller particles from that structure.

4.6 Discussion

I will now move on to discuss various aspects of these simulations such as: the degree of order observed, a comparison of deposition methods, and a comparison to literature studies using dipolar repulsions. I will then discuss future work which could be performed to compare experimental studies to the results displayed here, and some of the challenges this work might pose.

Firstly, the snapshots shown in figure 4.4 do not qualitatively exhibit long-range order, although at higher surface fractions there is some evidence of local order. A qualitative aspect of my results that does match with literature studies [102, 107] is the presence of "lanes" of smaller particles which lends some confidence to the results presented here. Comparisons to literature theoretical studies is tricky as these are often at effectively zero temperature where crystallisation is almost guaranteed. Notably, the well-ordered structure presented in figure 4.2 at $C = 4/5$ and $z = 0.5$ [102] (these values correspond to $n = 0.25$ using my parameters) is not observed at either surface fraction investigated here (figures 4.4 and 4.10), regardless of deposition method. However, even when comparing to experimental studies (such as figure 4.3 from [110]) the structures obtained via simulation from a screened monopolar repulsion can be seen to be more disordered than experimental studies with particles interacting via a dipole.

The clearest difference that can be seen qualitatively is the lack of long-range hexagonal order for the large particles interacting with a screened monopole, whereas in the dipolar case the smaller particles seemingly do little to disrupt the hexagonal ordering of the larger particles. This may arise because the dipolar interaction is effectively unscreened, such that good hexagonal order is observed even when the particle separation is ~ 10 times the particle diameter when only one particle size is adsorbed to the interface [110]. This is in contrast to the screened interaction studied in Chapter 3 (also [75]) where hexagonal order is only weakly present when the particles are separated by ~ 7 particle diameters (see fig. 3.5a).

Two deposition methods have been studied to mimic possible experimental procedures. Experimentally, one could mix the two particle sizes together and then load the pre-mixed particles on to an interface, although this could lead to species adsorbing at different rates due to different adsorption and diffusion dynamics. Alternatively, one could load just the large particles on to the

interface [110], let the particles equilibriate, then load the smaller particles on to the interface after some time has passed [113, 114]. While it is difficult to observe differences between these two methods from simulated snapshots (figures 4.4 and 4.10), quantitative measures of $g(r)$ and $|\psi_6|$ indicate there is some difference in the particles' ordering.

As previously noted, at each surface fraction probed the sequential deposition method leads to larger secondary peaks in $g(r)$ at low n for the case where only larger particles are considered. This implies that the sequential method leads to the larger particles having a more ordered structure, which is expected as the particles are allowed to be in a more ordered position in their initial conditions. On the other hand, at higher n there is no greater order of larger particles evident in the $g(r)$ for the sequential deposition. In fact, there is some evidence that there is more order in the large particle system in the one-step process.

This greater order in the one-step deposition is perhaps even more evident when comparing the bond orientational order parameter (figure 4.14c vs figure 4.14f) where there is a larger spike in the distribution of $|\psi_6|$ at 1 in the one-step deposition process. At the lower surface fraction (figure 4.8c vs figure 4.8f) this observation cannot be made as the shapes of the $|\psi_6|$ distribution are very similar, with the sequential deposition method leading to a slightly larger peak at 1.

I have observed that, at low surface fraction, the sequential deposition method leads to greater order in the system, especially of the larger particles. On the other hand, at high surface fraction, the one-step deposition leads to slightly more order amongst the larger particles. These observations might indicate that it is relatively easy for the interface to exist in a glassy state, i.e. there is no kinetic route for the particles to reach an energy minimum (as has been observed previously for certain particle ratios, e.g. [105]); at higher surface fraction, the particles may be stuck in this state. With this in mind, a route to greater disorder would be: the large particles first equilibriate into hexagonal order, the smaller particles are then deposited and subsequently perturb the larger particles away from equilibrium, the large particles then get stuck in this disordered state, with the large particles maintaining a large separation but without a fixed order.

For either deposition method there are likely to initially be areas of higher concentrations of large particles due to the random nature of the deposition. In the sequential deposition case, the concentration of large particles would "smooth out" as they repel each other, before the small particles are introduced. However,

in the one step deposition case, these areas of higher concentration could be jammed in place by the presence of the smaller particles. Areas of large particles with few smaller particles to interrupt the structure would exhibit greater local hexagonal order than a situation with a uniform large particle concentration where smaller particles lie in the interstices and perturb the larger particles from a hexagonal array. This would imply that the sequential deposition would lead to greater long range order if long range order were present in the system. However, in no case is good long range order observed and therefore any differences in long range order cannot be observed. Having given a possible explanation for these trends it is worth noting that the colour coded snapshots of $|\psi_6|$ (figures 4.9 and 4.15) are not conclusive in proving or disproving this theory, possibly because these are snapshots of one simulation frame whereas the distributions of $|\psi_6|$ are taken from 1000 simulation frames.

Finally, it is important to consider the observed peaks in $|\psi_6|$ at values other than 1. Note that, for any n-fold symmetry other than 2-, 3- or 6-fold symmetries, $|\psi_6|$ should be 0 for each particle. Therefore a peak at a value other than 1 or 0 indicates a finite degree of 6-fold symmetry, e.g. 0.5 could mean that half of a particle's neighbours are hexagonally ordered while the other half are either disordered or have a different symmetry. The colour coded simulation snapshots in figures 4.9 and 4.15 provide examples of points at which $|\psi_6|$ is neither 0 nor 1. An example from a theoretical viewpoint can be found in [116], which describes some structures which are compatible with a peak near 0.5.

I have observed that, in contrast to particles interacting with a dipolar repulsion, particles interacting via a screened monopole exhibit no long range order and relatively little local structure as well. Additionally, the deposition method affects the structure of the binary monolayer in different ways: (i) at low surface fraction a sequential deposition leads to greater order of the larger particles and (ii) at high surface fraction a sequential deposition leads to less local order of the larger particles.

4.7 Conclusion

In conclusion, this chapter has reviewed some of the field of binary arrays of particles at fluid interfaces. Previous literature has focussed on dipolar interactions whereas I have investigated particles interacting via a screened

monopolar interaction as described in Chapter 3. I have observed that the screened interaction leads to less ordered structures than those that have been previously reported, both experimentally, e.g. [110, 113], and theoretically, e.g. [102, 105]. Additionally, I have shown that the deposition method plays a role in the structure of these systems. Perhaps surprisingly this dependence is shown to be different at low and high surface fraction. At low surface fraction, a sequential deposition leads to more local ordering whereas at a higher surface fraction a sequential deposition leads to less local ordering. I attribute this behaviour to the idea that the particles at a high surface fraction get stuck in a disordered state as it has been observed that systems of particles at a fluid interface can exist in glassy states [105], where the smaller particles jam the larger particles into a structure which is perturbed from a hexagonal lattice.

Further work in this regard could look to compare experimental work to the simulations performed here. Additionally, these results have opened questions in regards to the bond orientational order parameter and what the local structural arrangements look like for peaks at values other than 1. Greater structural control may be achieved by gradually increasing the surface fraction by compression in a Langmuir trough setup, either in experiment or simulation. However, experimentally these results may prove challenging to achieve. For instance, while aggregation does not occur in simulation (because the model has a purely repulsive potential) for the relatively weak interaction of a screened monopolar potential aggregation can be hard to avoid. Spreading the particles at a very low surface fraction and then compressing the interface slowly with a Langmuir trough could go some way to mitigating this issue as well as possibly allowing the interface to reach a minimum energy configuration.

Chapter 5

Interfacial Rheology using an Indirect Shear Geometry

5.1 Abstract

I have developed an experimental method to perform interfacial rheology on liquid/liquid interfaces with no tool attached directly to the interface. This is achieved by shearing one of the liquid phases and measuring the interfacial response via confocal microscopy. Using this method I have measured steady shear material parameters such as the interfacial viscosity for fluid-like interfaces, and the interfacial elastic modulus for interfaces with solid-like behaviour. These measurements are in line with recent measurements made on the same system using a conventional probe. Moreover, using my method I am able to measure lower interfacial viscosities than those that have previously been reported. This indirect method lends itself to microscopic structural analysis, as well as macroscopic rheological analysis, due to simultaneous microscopy. My analysis shows that the interfacial behaviour is strongly dependent on the surface coverage and surface structure, and steady shear can have an irreversible effect on the structure of an interface.

5.2 Introduction

Interfacial rheometry is essential when characterising systems with large interfacial area, such as emulsions or foams [2, 3]. As mentioned in Chapter 3, these systems are ubiquitous in industries such as the cosmetics, pharmaceutical or the food industries [18, 30, 77, 78]. In order to probe the rheological properties, one can use shear rheology [2, 3, 10, 57, 117, 118], or dilational rheology [2, 3, 119–121], or simultaneously image the interface as a deformation is applied to connect the rheological properties to the interfacial microstructure [15, 16, 118]. In this work I focus on shear rheology, using an indirect probe with simultaneous imaging, in order to minimally disturb the interface before and during characterisation. I observe rheological properties consistent with previous measurements in the literature, and using this system I am able to simultaneously measure the interfacial structure and link this to the flow behaviour at the interface. Additionally, my setup has the advantages of being industrially relevant due to the indirect nature of the shear, and being able to measure lower interfacial viscosities than those that have been previously reported.

Previous work on interfacial shear rheology has used probes which directly attach to an oil/water or air/water interface, such as the magnetic rod interfacial stress rheometer [54], or the double wall ring (DWR) geometry attached to a rotational rheometer [15, 57]. These experimental setups are both based on the maximisation of the Boussinesq number [2] given in equation (5.1):

$$Bq = \frac{\eta_S}{\eta L}, \tag{5.1}$$

where η_S is the surface viscosity, η is the subphase viscosity and L is a characteristic length scale roughly equal to the ratio of contact area to contact perimeter. Bq can be rewritten as the ratio of the surface drag force to the subphase drag force. In order to accurately measure the surface properties without unintentionally probing the subphase, this ratio must be maximised for the surface to contribute at least an order of magnitude more than the bulk. Of the two setups mentioned, the magnetic rod has the larger Bq, while both have a Bq an order of magnitude larger than that of a rotating disk, due to a much smaller L [122]. This maximisation of Bq can be considered as optimising the signal to noise ratio. Even though the magnetic rod set-up has higher sensitivity, the DWR does have some advantages over the magnetic rod rheometer: it can be

attached to a conventional rotational rheometer and has a larger dynamic range.

In my work, I take a different approach where rather than affixing a probe directly to the interface, I shear the upper phase, indirectly deforming the interface, and measure the response using confocal microscopy. This technique has two main advantages: (i) the interface I probe is purely a particle laden, liquid-liquid interface, with no large probe immersed therein, and (ii) this setup models general applications of these large interfacial area systems, where the interface is indirectly sheared by shearing the continuous phase. A clear example of this second point is in the application of skin creams, where upon application, the continuous phase is sheared which indirectly deforms the large area of interface present in the system. As there is no contact area or contact perimeter in my set-up, considerations of Bq are less tangible; in § 5.3.6 I introduce an analagous Bq^*.

I investigate the efficacy of this method by studying a weakly interacting system of interfacially adsorbed colloidal particles. This system has been studied previously, both looking into its interfacial rheology using a direct probing technique [10], and considering the interparticle interactions of the interfacial colloidal particles (Chapter 3, [75]).

5.3 Materials and Methods

The materials and methods not specific to this chapter are described in chapter 2. In this section methods which are specific to this chapter are described. The particles used in this section are labelled as ASM628. For the particle properties see Table 2.1. Interfaces were prepared following § 2.3.1 with surface fractions of $\sim$30% and $\sim$50%.

5.3.1 Measuring Surface Coverage

I use two methods for measuring surface fraction, ϕ, from interfacial micrographs: 1) I measure the fraction of white pixels to total pixels after performing a thresholding procedure. The thresholding is performed using the Otsu method of the Auto Local Threshold function in ImageJ [123]; 2) I obtain a count of the number of particles in a frame and using the particle size, R_p and image size, A_{im}

I calculate the surface fraction as

$$\phi = \frac{N_p \pi R_p^2}{A_{\text{im}}}, \tag{5.2}$$

where N_p is the number of particles in the frame. I will refer to these methods as 1) pixel fraction method, and 2) particle counting method.

Using the particle counting method, one could also incorporate the contact angle into the calculation of ϕ, defining the surface fraction as the area of fluid interface removed from the system by the presence of the particle. While this definition may be more practical for studies concerning interfacial tension, for shear rheology particle-particle contacts are of more interest and so the definition in equation 5.2 is chosen here.

In each case, high magnification images are recorded using the confocal digital zoom with a 10× objective. The magnification level was chosen to strike a balance between individual particle resolution, which improves upon magnification (to a point), and statistics of particle counting, which decreases upon magnification.

5.3.2 Measuring Surface Structure

Structural properties of interfaces were measured using four different methods. These four methods were chosen to provide comprehensive information on the image data with some methods being complementary (e.g. real space analysis and fourier analysis) and some providing double checks on interpretations (e.g. comparing two real space analyses). The first of these is the autocorrelation function (ACF(r)). Similar to $g(r)$, this is a measure of the likelihood of finding a feature a distance r away from another feature. In the case of $g(r)$ these features are particles, whereas for the ACF I consider here, these features are pixel intensities. The ACF is computed using a Python code written in house based on the equation

$$\text{ACF}(r) = \langle \mathcal{F}^{-1}(\mathcal{F}(I(-\vec{r})\mathcal{F}(I(\vec{r})))\rangle_\theta, \tag{5.3}$$

where $\mathcal{F}$ ($\mathcal{F}^{-1}$) denotes the (inverse) 2d Fourier transform, I is a matrix of pixel intensities for the image and I average over angle θ as I assume there is isotropy in the system. In words this amounts to finding the product of the Fourier transformed image with the Fourier transform of the mirrored image and

subsequently taking the inverse Fourier transform of that product. Equivalently, this is the convolution of an image with its own mirror.

The second measurement of structure is considering cluster size polydispersity. Histograms of cluster sizes are found showing the number of pixels in regions of different sizes, using the `skimage` Python package. The polydispersity can be found from these data as the ratio of the standard deviation in region size, s, to the mean region size, $\langle A \rangle$:

$$\mathcal{D} = \frac{s}{\langle A \rangle}. \tag{5.4}$$

The third measurement of structure is simply the size of the largest region, found using the same histograms described previously. Finally, I compare power spectra of images, $P(r)$, again averaged over polar angle. Key differences in power spectra include the shape of the curve and features corresponding to typical lengthscales. The power spectrum of an image is found as

$$P(r) = \langle |\mathcal{F}(I(\vec{r}))|^2 \rangle_\theta, \tag{5.5}$$

where I average over the polar angle θ.

5.3.3 Experimental Setup

The experimental setup is shown in Figure 5.1. The cup in which the interface is prepared is shown in more detail in Figure 2.1.

A 25 mm diameter parallel plate geometry (Anton Paar PP25/S) was used with an Anton Paar MCR301 rheometer. The geometry was attached to the oil/air interface in the centre of the PTFE cup. Using a similar rheoimaging setup described by Besseling *et al.* [34] (although my rheometer setup lies directly on top of the confocal providing greater stability), rheometry could be conducted while the interface was simultaneously imaged using a Leica SP8 confocal microscope. The imaging setup was such that the motion of the interface under shear was horizontally oriented. Velocimetry of the confocal images was performed using C code written by Dr Michiel Hermes. This splits the images into 10 equally spaced bands. Each band is correlated with the previous image at various horizontal offsets. The distance moved between that frame and the previous is then the horizontal offset which maximises this correlation.

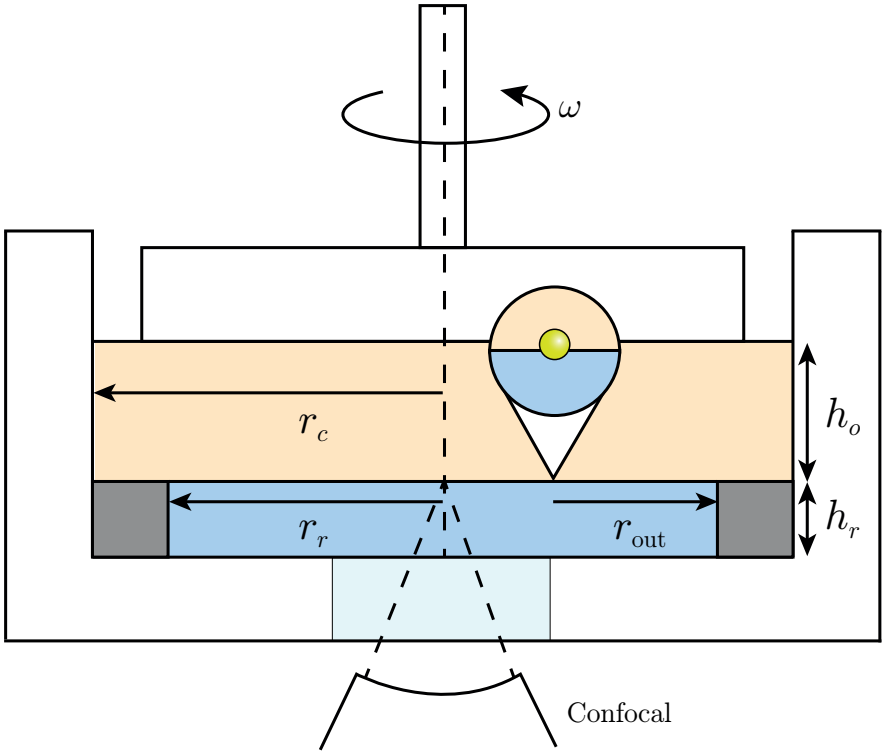

Figure 5.1 *Schematic of the setup for performing indirect interfacial rheology using a parallel plate geometry attached to a stress controlled rheometer. The rheometer head is rotated at a fixed angular velocity, ω. Imaging of the interface is done using a confocal microscope. $r_c = 21$ mm, $r_r = 10$ mm, $h_r = 3$ mm, and h_o and ω are varied for different experiments. r_{out} is the radial distance from the measurement window to the outer, roughened edge of the aluminium ring. Note that the distances drawn are not to scale.*

5.3.4 Steady Shear Rheology

To measure the steady shear properties of the interface, fixed rotation speeds, ω, were applied to the geometry for 2 minutes before a further 30 s period of fixing the rotation of the rheometer to 0 to ensure the rheometer head stops moving. A schematic for this protocol is given in figure 5.2. To test the dependence on the height of the oil phase, three heights were used at comparable, low surface fractions.

The interfacial strain rate is calculated as $\frac{v}{r_{\text{out}}}$, where v is the measured velocity of the interface and r_{out} is the distance from the measurement to the outer, pinned wall. The velocity is measured by applying the velocimetry described above to the central 50% of the experiment, i.e. from 37.5 s to 112.5 s. To measure strain at a high surface fraction, the size of the elastic recoil upon cessation of shear is

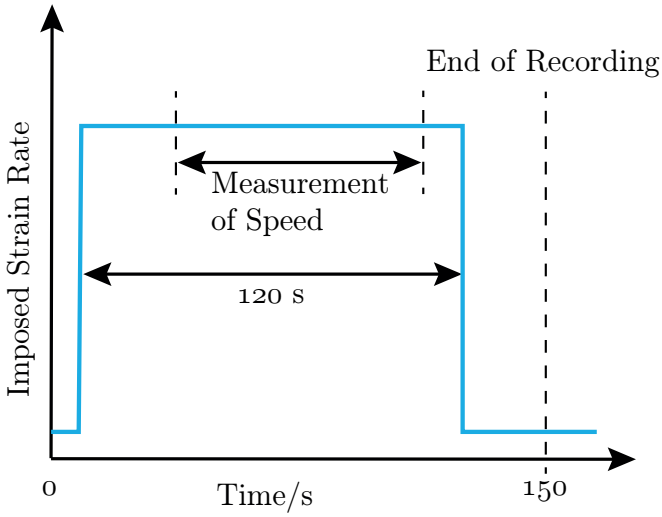

Figure 5.2 *Schematic representation of the shear protocol to perform steady shear rheology. The recording begins at time 0 and ends as indicated at 150 s.*

found. This is converted to strain by dividing by r_{out}. The stress is measured following § 5.3.6.

5.3.5 Oscillatory Rheology

To perform oscillatory rheology, it is important to synchronise the interfacial response with the driving stress[1] from the rheometer plate. However, as the rheometer and microscope are controlled by separate PCs, this requirement poses a problem. To circumvent this, a well defined oscillation is applied to the rheometer, the response of the interface is then recorded as usual and during the same oscillation the rheometer head is tracked at a later time, again via confocal microscopy. The well defined sinusoidal motion of the rheometer head is then extrapolated backwards in time to coincide with the interfacial response.

Once the stress and strain are calculated they can be plotted against time on the same plot and G^*, the complex shear modulus, can be obtained by fitting a single sinusoidal function to both the driving stress, σ_d, and the strain response, γ,

$$\sigma_d = \sigma_0 \cos(\omega_\sigma(t + \Delta t_\sigma)) \tag{5.6}$$

$$\gamma = \gamma_0 \cos(\omega_\gamma(t + \Delta t_\gamma)), \tag{5.7}$$

[1]Note that the driving stress is imposed by a fixed rotation speed of the rheometer, see equation (5.18)

where σ_0, γ_0, Δt_σ, and Δt_γ are fitting parameters. σ_0 is the amplitude of the driving stress and γ_0 is the amplitude of the strain response; a physical interpretation of Δt_σ and Δt_γ is discussed below. The driving and response frequencies, ω_σ and ω_γ respectively, should be identical and equal to the imposed frequency of oscillation. However, due to start-up effects of the oscillation, these are input as fit parameters to ensure that results are only taken when start-up effects have been overcome and $\omega_\sigma = \omega_\gamma$.

The key material parameters are the storage and loss moduli, G' and G'', and the phase lag between stress and strain δ. From the fits in equation (5.6), the phase lag can be found as

$$\delta = \omega(\Delta t_\sigma - \Delta t_\gamma), \tag{5.8}$$

where I use ω as the imposed oscillation frequency of the rheometer. This then allows the storage and loss modulus to be calculated as

$$G' = \frac{\sigma_0}{\gamma_0}\cos(\delta) \tag{5.9}$$

$$G'' = \frac{\sigma_0}{\gamma_0}\sin(\delta), \tag{5.10}$$

such that the complex modulus $G^* = G' + iG''$. G' is the in phase response of the interface, which represents the elastic properties, and G'' is the out of phase response of the interface, which represents the viscous properties. For a purely elastic material, $\delta = 0$ while for a purely viscous material $\delta = \pi/2$.

These measurements were made at a strain amplitude of the oscillation of the rheometer of 0.1% and the frequencies, ω were from 1.0 rad/s to 16 rad/s. The frequencies were logarithmically spaced with 5 points per decade. The strain amplitude was chosen such that it was below the yielding point found in [10].

5.3.6 Measuring Stress

To make meaningful statements on the rheological properties of the interface, the interfacial stress must first be found. It is well known that for a parallel plate setup, the stress is independent of the height through the sample upon reaching a steady state [124]. It can be shown that the timescale to reach steady state is on the order of 10 s for my setup, discussed in more detail in § 5.4.4 [124], for this reason I only measure interfacial strain rates at times > 30 s. Considering the upper phase as a Newtonian fluid allows us to therefore find the stress on the

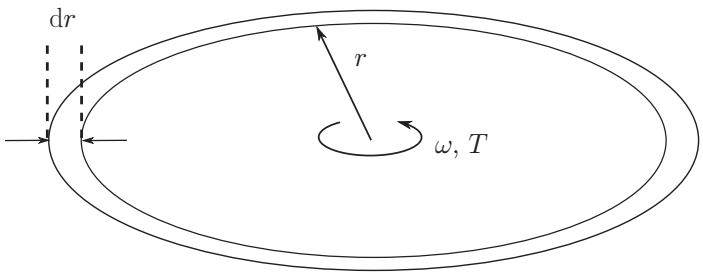

Figure 5.3 *Thin ring at oil/water interface. The interfacial stress applied to the ring's perimeter can be equated with the bulk stress from above applied to the ring's area.*

interface from the upper fluid using the applied rotational speed of the geometry.

If the rheometer is rotated at a fixed angular velocity of ω then the strain rate of the upper fluid at a radius r of the parallel plate geometry is given by

$$\dot{\gamma} = \frac{\omega r}{h_o}, \tag{5.11}$$

where h_o is the depth of the oil phase. This definition relies on the interface having zero speed. This is therefore a first approximation if the speed of the geometry is much larger than the speed of the interface. If this is not the case then ω can be rescaled by the angular speed of the interface, ω_i, at the radius r, leading to

$$\dot{\gamma} = \frac{(\omega - \omega_i)r}{h_o}. \tag{5.12}$$

The stress needed to induce this rotation is simply given by the product of strain rate with the bulk viscosity of the upper phase η_o, such that the stress is given by

$$\sigma = \frac{\eta_o(\omega - \omega_i)r}{h_o}. \tag{5.13}$$

To convert this bulk stress into an interfacial stress I consider the torque applied from the bulk on an area element of a ring in the interface at r of width dr as shown in figure 5.3.

I write the torque element, $\mathrm{d}T$, as a product of the force element, $\mathrm{d}F = \sigma \mathrm{d}A$, and the radius, where $\mathrm{d}A = 2\pi r \mathrm{d}r$ is the area of the inifinitesimal ring,

$$\mathrm{d}T = \sigma 2\pi r^2 \mathrm{d}r, \tag{5.14}$$

$$\mathrm{d}T = 2\pi\frac{\eta_o(\omega-\omega_i)}{h_o}r^3\mathrm{d}r. \tag{5.15}$$

This torque then gives rise to the interfacial stress, where I write a torque balance such that $\mathrm{d}T = T_s(r+\mathrm{d}r) - T_s(r)$, where T_s is the torque at the interface in terms of interfacial stress. This torque is the product of the perimeter, P, the interfacial stress, σ_s and the radius r, $T_s(r) = P(r)\sigma_s(r)r$.

$$\begin{aligned}\mathrm{d}T =& T_s(r+\mathrm{d}r) - T_s(r)\\ =& 2\pi(r+\mathrm{d}r)(\sigma_s(r+\mathrm{d}r))(r+\mathrm{d}r) - 2\pi r\sigma_s(r)r\\ =& 2\pi r^2\sigma_s(r+\mathrm{d}r) + 4\pi r\sigma_s(r+\mathrm{d}r)\mathrm{d}r\\ & - 2\pi r^2\sigma_s(r),\end{aligned} \tag{5.16}$$

where terms in $(\mathrm{d}r)^2$ have been dropped. Equating equations (5.15) and (5.16) and rearranging terms leads to a first order ordinary differential equation

$$\frac{\mathrm{d}\sigma_s}{\mathrm{d}r} + \frac{2\sigma_s}{r} = \frac{\eta_o(\omega-\omega_i)}{h_o}r, \tag{5.17}$$

where upon taking $\mathrm{d}r \to 0$ I have equated $\sigma_s(r+\mathrm{d}r) = \sigma_s(r)$, equivalent to dropping terms of order $\mathrm{d}r^2$.

This can be readily solved to give

$$\sigma_s = \frac{\eta_o(\omega-\omega_i)}{4h_o}r^2. \tag{5.18}$$

It is evident that this expression yields the correct dimensions for interfacial stress as Pa.m, as well as physically reasonable dependencies on viscosity, applied rotation, the height of the oil phase, and the radius. In order to vary the interfacial stress, I vary the rotation speed of the rheometer while observing the interface at a fixed radius. From a practical point of view, varying the rotation speed is much simpler than varying r.

It is worth noting that in solving equation (5.17) I have assumed that ω_i is slowly varying. I can quantify this assumption by considering a dimensionless number analogous to the Boussinesq number,

$$Bq^* = \frac{\eta_s h_o}{\eta_o r^2}, \tag{5.19}$$

where η_s is the interfacial viscosity. For the solution in equation (5.18) to be accurate, Bq^* must be $\gg 1$. The numerator and denominator can be considered to be $\eta_s r$ and $\frac{\eta_o r^3}{h_o}$ respectively. These are, up to geometric factors, the force per unit strain rate due to the interface and the force per unit strain rate due to the bulk. Typical values for these parameters from previous work [10] on a similar system gives $Bq^* \simeq 100$. Given the above consideration, $Bq^* \gg 1$ means that the interface dominates the rheological response in my set-up. One should be careful, however, when considering experiments done at lower surface fractions where one would expect a much lower surface viscosity and therefore a lower Bq^*.

5.4 Results and Discussion

5.4.1 Measuring Surface Coverage

Figure 5.4 shows the initial interface at two different surface coverages. For Figure 5.4a the pixel fraction method gives $\phi = 31.0\%$ while the particle counting method gives $\phi = 23.0\%$. For Figure 5.4b the pixel fraction method gives $\phi = 56.7\%$ while the particle counting method gives $\phi = 46.1\%$. For conciseness, references to these experiments will only refer to the results from the pixel fraction method.

Note the significant difference in the two measurement methods of surface coverage, highlighting flaws in one or both methods leading to inaccurate measures. With perfect particle resolution, the particle counting method should yield the exact answer *for that particular region of the interface*, however, perfect particle resolution is rarely achieved for this system especially at high ϕ, i.e. a particle locating algorithm might label a cluster of particles as one larger particle. The pixel fraction method is also flawed in that it assumes a direct match between area of emitted light and area of the particle. This however is not true due to the point spread function, a question over whether the particles are exactly in the focal plane, and the brightness of the fluorophore itself.

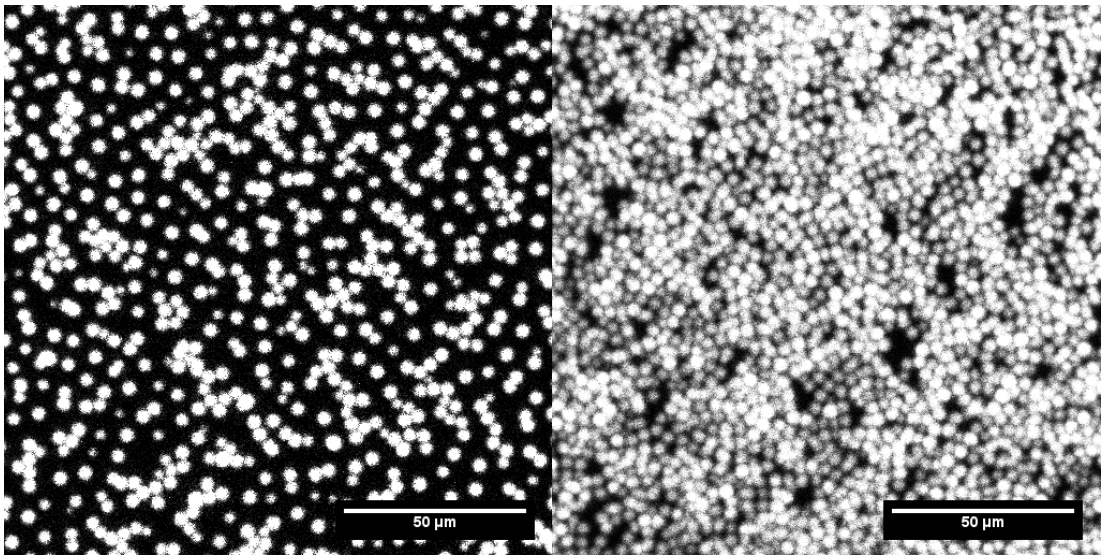

(a) **(b)**

Figure 5.4 *Fluorescent confocal micrographs of PMMA-PLMA particles (white) at a water-oil interface at two initial conditions. (a) Surface fraction of 31.0%, (b) surface fraction of 56.7%. As well as a difference in surface fraction, the structure of these surfaces are markedly different, with (a) being dominantly separated particles with some aggregation, while (b) has a percolating structure but is not fully close packed.*

5.4.2 Structural Response to Shear

Image analyses reveal that the interfacial structure changes markedly upon shear, specifically above some critical shear rate. Initially the interfaces were quite well ordered, with some aggregation due to the high surface coverage, and inherent attractive capillary or van der Waals forces. While capillary forces should be negligible, due to a vanishingly small Bond number and the use of spherical particles [18], there will be a certain roughness to the particles and the effect of variable lengths of the steric stabiliser "hairs" on the particles' surfaces may cause contact line undulations which lead to short range capillary attraction [125, 126]. Qualitatively, I see from the images taken before and after shear is applied (figure 5.5) that the interface changes from a relatively homogeneous structure, with some small local variations in surface fraction, to an inhomogeneous structure with most particles forming one large aggregate which percolates across the region imaged.

The structures in these images have also been analysed in a more quantitative manner. The most noticeable differences between the pre-shear ACF (figure 5.6a)

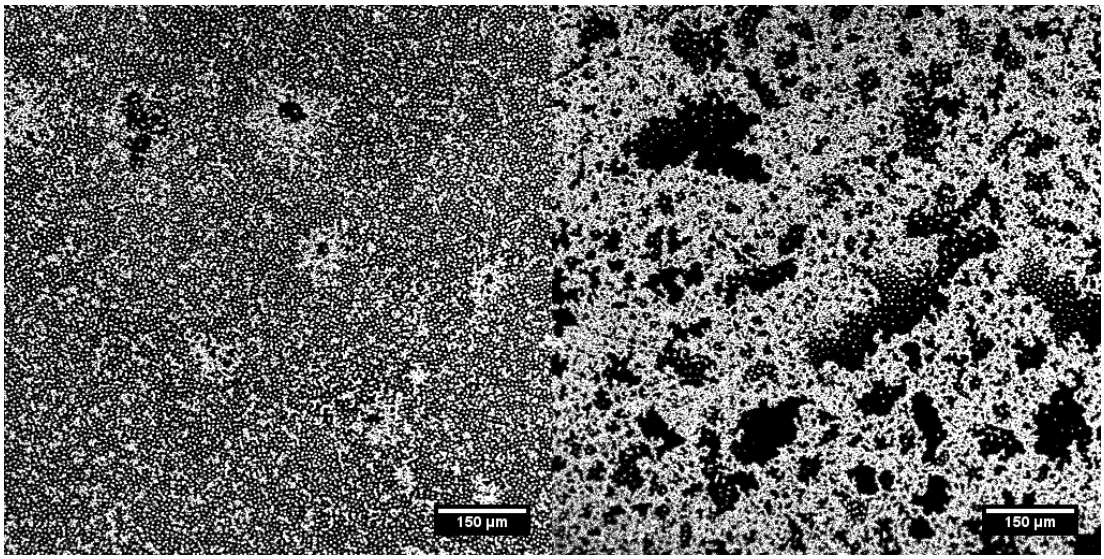

(a) **(b)**

Figure 5.5 *Fluorescent micrographs of PMMA-PLMA particles (white) at a water-oil interface (a) before and (b) after applying shears up to a rotation speed of the rheometer of 25.0 rev/min, $\sigma_s = 0.02$ mPa.m. Comparing the two panels shows that the interfacial structure has changed markedly, becoming more heterogeneous after shear has been applied. The surface fraction determined from high magnification images of the same experiment is 31.0%.*

and the post-shear ACF (figure 5.6b) are the brief oscillatory behaviour pre-shear, and the magnitude of the characteristic decay length. Short range oscillations in the ACF imply a degree of order, which can be seen from the real space image as, in general, particles are isolated from others, with the characteristic separation being able to be read from the ACF as the first maximum, occurring at 7.3 μm. If one were to calculate the average interparticle separation based on the surface fraction one would find either 4.8 μm or 5.5 μm depending on which value of surface fraction is used (particle counting or pixel fraction). This discrepancy is caused by a relatively poor resolution (compared to the particle size) in the image, each point in the ACF being separated by $\sim$ 2 μm, and the lack of a hexagonal structure which is assumed for the estimate of average interparticle separation from surface fractions. In contrast, the post-shear ACF shows purely a decay, implying that the particles are commonly found in aggregates, or even a single, percolating structure, as, no matter how far from one particle one checks, it is always more likely to find another particle there than at infinity[2].

[2]Although the ACF should asymptotically level off at a constant value for a given area fraction of particles.

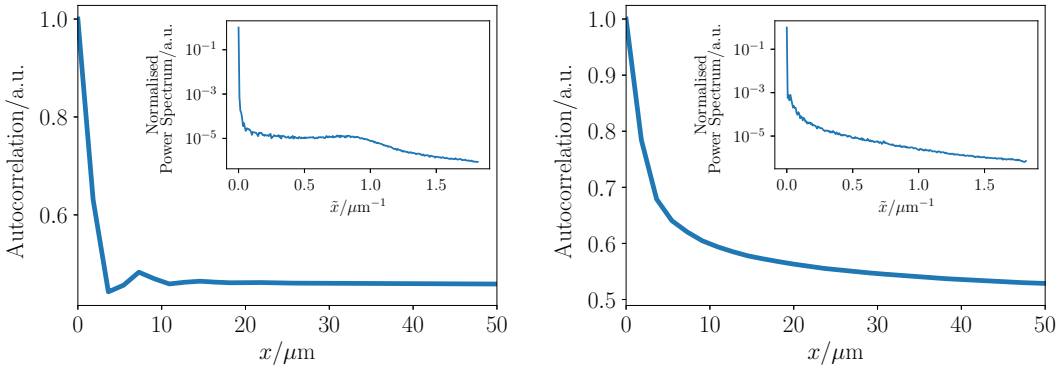

(a) **(b)**

Figure 5.6 *Autocorrelation function and power spectrum (inset) of the images in figure 5.5 (a) preshear and (b) post shear. x is the separation of pixels in the correlation and $\tilde{x}$ is the equivalent separation in reciprocal space. Note that x here represents the magnitude of the position vector $\vec{x}$.*

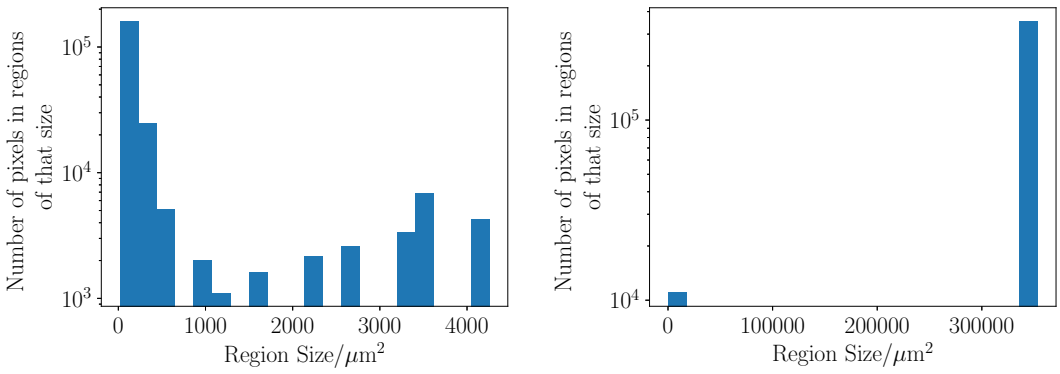

(a) **(b)**

Figure 5.7 *Histograms for number of pixels in regions of a certain size for the images in figure 5.5 (a) preshear and (b) post shear. The shapes of these indicate that in figure 5.5(a) there are many small regions showing little aggregation, while in figure 5.5(b) there is one large region with a few small regions, showing a large amount of aggregation.*

Power spectra calculated from interfacial micrographs also highlight the drastic change in structure after shear is applied. The change in behaviour of the pre-shear power spectrum (figure 5.6a inset) at $\tilde{r} \simeq 1\ \mu\text{m}^{-1}$ indicates a characteristic lengthscale in the image at around a separation of 6.3 μm, in agreement with the ACF. There is no such characteristic lengthscale post-shear (figure 5.6b inset), implying that there is no repeating structure.

In addition, region size analyses quantitatively show shear induced aggregation. These have been summarised in a histogram of the number of pixels which are in a region of a specific size against that region size (figure 5.7). These histograms make clear the distinction between the two images. Pre-shear, I see pixels are mostly in very small regions, with some larger, aggregated regions. This contrasts the post-shear results, where almost every pixel is in a very large region, the bin being at 344,000 μm^2, with the image size being $932\mu\text{m}\times932\mu\text{m}$ or 868,624 μm^2, so 40% of the image is taken up by a single region. I can use these histograms to measure polydispersity, defined by equation (5.4) [10]. I find for the homogeneous, preshear surface, $\mathcal{D} = 2.49$ while for post-shear I find $\mathcal{D} = 13.5$.

I have observed that applying shear leads to considerable aggregation in this system. For aggregation to occur the shear force must exceed the maximum repulsive force between these particles. In Chapter 3 I observed that these particles interact via a repulsive screened Coulomb potential. In order to overcome this repulsion I assume that they must overcome the maximum repulsive force, which for this potential is the point at which these particles are in contact, i.e. $r = 3.0\mu m$. This maximum force can be found to be 9.88×10^{-13} N, where I have rescaled the parameters from Chapter 3 as in this chapter I use larger particles. This force can then be converted to an interfacial stress by dividing by the particle diameter to give a critical aggregation stress of 3.3×10^{-7} Pa.m. Experimentally, I found that aggregation occurs starting at a stress of 2.6×10^{-6} Pa.m, which is in some agreement, discrepancies can arise from geometric factors or uncertainties in the fitting parameters of the interparticle potential. This agreement between experiment and prediction lends confidence to the use of equation (5.18) when calculating interfacial stress in my unique geometry. In order to aggregate, the applied stress must also overcome the steric repulsion, however the steric barrier is considerably smaller (for a similar particle) than the electrostatic barrier I have measured [127]. Once these particles come into close contact, attractive capillary forces and van der Waals forces are large enough such that this is an irreversible state. The strength of the van der Waals force

if the particles with radius ~ 1 μm come within 0.1 μm, i.e. approximately the resolution of the microscope, can be found to be approximately 2 $k_{\mathrm{B}}T$ [125]. The capillary forces at a surface to surface separation of 0.1 μm due to contact line undulations of 10 nm, which may be caused by heterogeneity in the stabiliser distribution over the particles' surfaces, can be found to be approximately 200 $k_{\mathrm{B}}T$ [111]. We can therefore see that these contributions are sufficient to induce particle aggregation at the water-oil interface.

To summarise the interfacial structure section of my results, I have observed from these interfacial structure analyses that, upon shearing the interface there is a clear transition from a relatively ordered state to a highly aggregated state which percolates across the field of view of the microscope. This behaviour is in line with estimates that show the energy input during shear can overcome the long-range repulsion between these particles, pushing the particles into an energy minimum which I argue is due to attractive capillary and van der Waals interactions.

5.4.3 Steady Shear Rheology

Having measured the surface fraction and surface structure in each case, I now turn to interfacial rheology measurements. Strain vs time plots show a smooth flowing behaviour at a lower surface fraction (31%), with a constant strain rate over the duration of the shear being applied (figures 5.8a and 5.8b). As expected, at larger imposed shear rates from the rheometer a larger interfacial shear rate is measured in response. Note that, when shear starts the interface appears to immediately (within temporal resolution of the analysis method) begin flowing at a constant shear rate. Similarly, when the shear ends the interface immediately stops flowing. This implies that the response of the interface to shear in this regime is purely viscous with no measurable elastic behaviour.

At the higher surface fraction I observe markedly different behaviour, with elastic behaviour being evident from the strain vs time plots (figures 5.8c and 5.8d). Focussing on the low stress behaviour initially (figure 5.8c) an initial jump to a higher strain is observed, indicative of an elastic material. There is then some erratic motion in the direction of shear (i.e. the strain is always positive), indicating that there is some frustrated motion and rearrangements of the interfacial structure [128]. While the initial elastic response is difficult to measure precisely due to background noise in the flow, upon cessation of the shear the interface clearly recoils, allowing the elastic strain to be readily

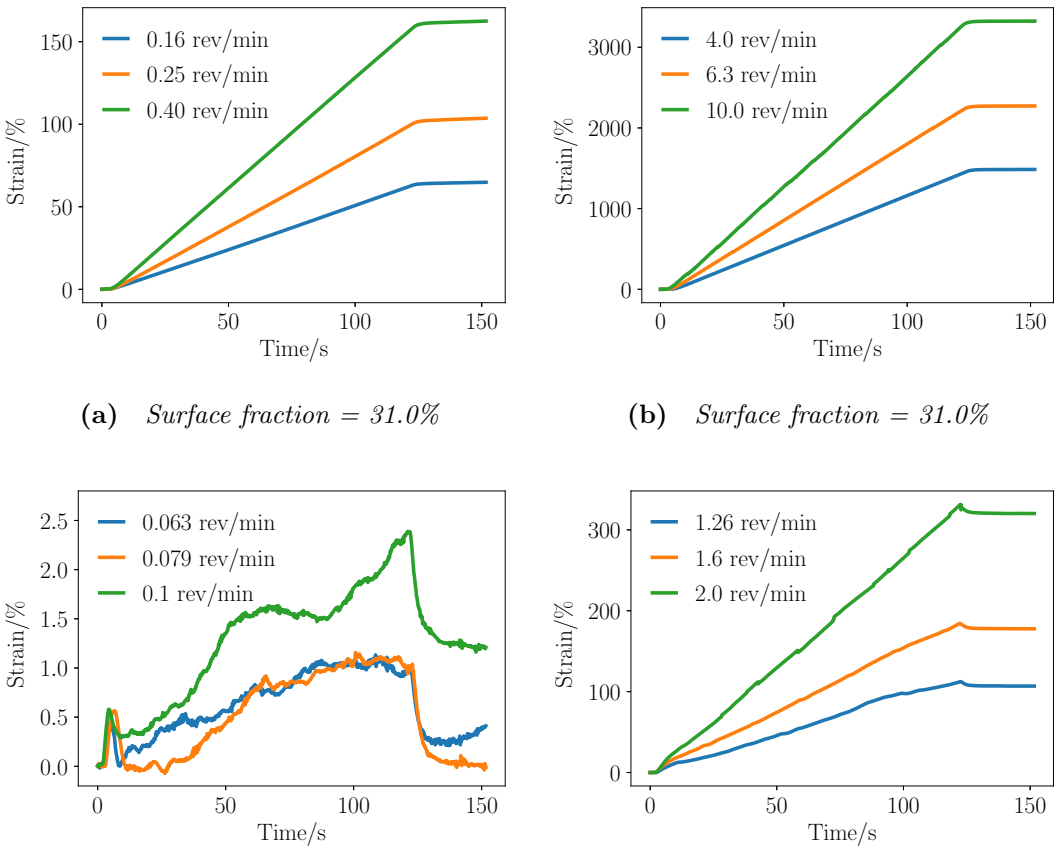

(a) *Surface fraction = 31.0%*

(b) *Surface fraction = 31.0%*

(c) *Surface fraction = 56.7%*

(d) *Surface fraction = 56.7%*

Figure 5.8 *Plots of strain vs time for experiments performed at $\phi = 31.0\%$ at (a) low imposed strain rate and (b) high imposed strain rate, and $\phi = 56.7\%$ at (c) low imposed strain rate and (d) high imposed strain rate. The rheometer rotation speeds are given in the legend of each figure. The plateaus in these plots, at 0 s and 130 s are due to video recording starting before and ending after the shear is applied.*

measured [129]. This statement becomes even more apparent when looking at higher applied stresses, as at these large stresses the flowing behaviour completely dominates the strain response and the initial elastic jump is barely visible in the data. However, once the shear has been stopped, the elastic recoil is clear.

To quantify the rheological properties of these particle laden interfaces I plot stress vs strain rate to obtain a flow curve for each experiment at a different height of the oil phase. As expected, for relatively low surface coverages I observe a Newtonian response (figure 5.9). I can therefore attribute one constant value for interfacial viscosity for each oil phase height. These are consistent with what is measured using the DWR setup on the same system [130]. The measurements obtained

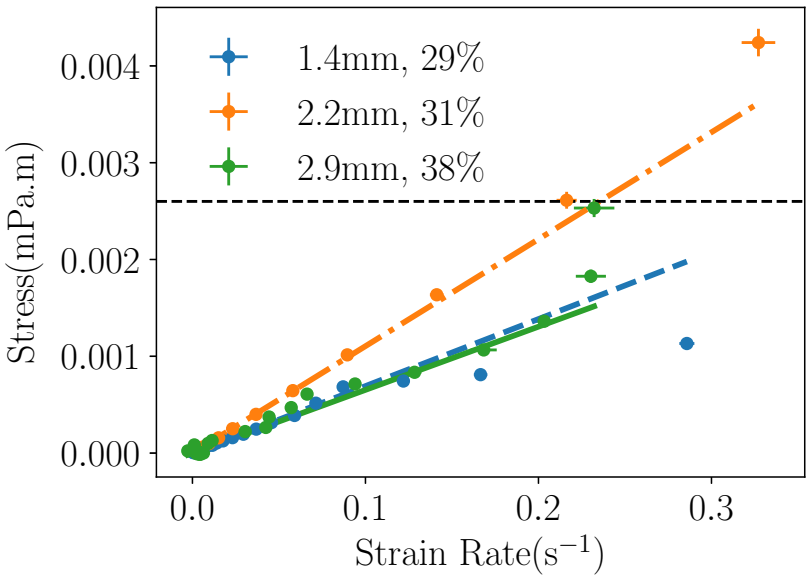

Figure 5.9 *Rheological behaviour of a particle laden interface at relatively low surface coverages (exact values given in figure legend). The three lines are measurements made at different oil layer thicknesses, which can be seen in the figure legend. Points are measured data, lines are fits to a linear model of constant viscosity. Interfacial viscosities are measured as* $6.9(3) \times 10^{-6}$ *Pa.m.s (blue solid line),* $1.1(2) \times 10^{-5}$ *Pa.m.s (orange dot-dashed line) and* $6.5(7) \times 10^{-6}$ *Pa.m.s (green dashed line). Differences in interfacial viscosity arise due to different interfacial structures which can be quantified by polydispersity,* $\mathcal{D}$*.* $\mathcal{D}$ *are measured to be 23.4 (blue solid line), 2.49 (orange dot-dashed line), and 24.7 (green dashed line). Note that the data points are logarithmically spaced such that points at lower strain rate appear to have a disproportionate affect on the fit when plotted on linear axes. The horizontal dashed line shows the experimentally determined critical aggregation stress.*

using the DWR yielded larger values for interfacial viscosity, one explanation for this difference is that the DWR measurements were taken at a surface coverage of 78%, while these measurements here were taken at surface coverages from 29% to 38%.

I have performed repeats of these experiments while varying the thickness of the oil phase to test the robustness of my technique, observing some agreement across the three oil thicknesses tested (figure 5.9), suggesting that the height of the oil phase does not seem to have an effect (as expected). However, there is some variation across the three measurements which the respective surface fractions I measure do not explain. Because of this I also measure the polydispersity at the

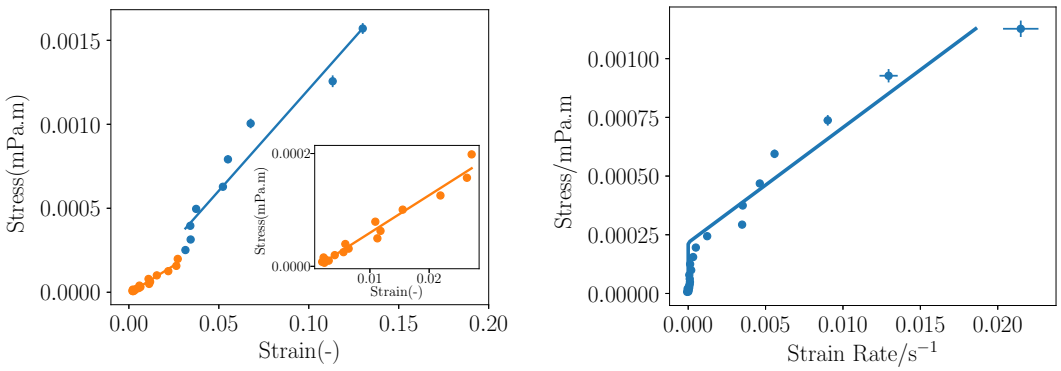

(a) **(b)**

Figure 5.10 *Rheological behaviour of a dodecane-water interface laden with PMMA-PLMA at a surface fraction of 56.7%. (a) Elastic response of the interface to applied stress with the data (points) fitted to a linear model (line) of stress vs. strain, i.e. a Hookean response. The strain here is measured from the elastic recoil from velocimetry data. (b) Viscous response of the interface with the data (points) fit to a 2 dimensional Bingham fluid model (line).*

interface using equation 5.4. For the data at 1.4 mm and 2.9 mm I find $\mathcal{D} = 23.4$ and 24.7 respectively. Contrasting these numbers, I find for the data at 2.2 mm that $\mathcal{D} = 2.49$.

Both these measures of aggregation, combined with the values for the viscosity which were measured, indicate that the surface structure plays a significant role in the rheological properties of these interfaces; a more aggregated interface leads to a lower viscosity. I finally note that, while the viscosities do vary for different oil thicknesses, the magnitudes of the stresses and strains are comparable across all thicknesses.

At higher ϕ I observe a more complex rheological response, where the interface behaves as a yield stress fluid. Similarly to previously fitting a Newtonian, viscous response at lower ϕ, at higher ϕ I fit a linear dependence of the elastic strain response to the imposed shear stress (figure 5.10a). This modelled Hookean behaviour gives us a shear modulus of $1.17(3) \times 10^{-5}$ Pa.m, consistent with previous measurements on a similar system [10].

I fit the data to a straight line as a first approximation for the elastic behaviour that is seen both in the videos, and in the tracking (figure 5.8). This allowed me to measure one value for elastic modulus, which as noted, is consistent with previous measurements in the literature [10]. However, I do note that there is

a feature in the data in figure 5.10a around a strain of 0.03 which correlates almost exactly with the point at which the yielding behaviour in figure 5.10b can be observed. I could therefore attribute (at least) two values of elastic modulus to this interface, one value before the interface yields and one after. While one would think that upon yielding the interface should have zero elastic modulus, here I still measure elastic, recoiling behaviour after yielding so can still attribute a value for the elastic modulus.

I also infer that this interface behaves as a yield stress fluid (figure 5.10b), as has been observed previously using the DWR geometry [10]. By fitting a simple piecewise function to these data, I obtain both a yield stress and an effective viscosity. I model the interface as a Bingham fluid described by:

$$\begin{aligned} \dot{\gamma} &= 0 && : \sigma < \sigma_y \\ \sigma &= \sigma_y + \eta_S \dot{\gamma} && : \sigma \geq \sigma_y, \end{aligned} \tag{5.20}$$

where σ_y is the yield stress and η_S is an effective interfacial viscosity. Here I measure a yield stress of $2.2(3) \times 10^{-7}$ Pa.m, which is an order of magnitude lower than the yield stress quoted in [10], where the surface coverage is 78% in [10] and 56.7% for my measurements.

I feel that this is an appropriate model as the parameter which I am most interested in comparing to the literature is the yield stress. As noted, the yield stress I measure is an order of magnitude lower than the yield stress measured in [10]. However, here I measure a steady shear yield stress whereas the literature value is an oscillatory shear value, so a direct comparison of these is not necessarily appropriate [131]. Also, I am measuring at a surface fraction of 56.7%, while the surface fraction used in [10] was estimated at 78%. The smaller elastic modulus I measure would be expected considering this difference in surface fraction, e.g. [132, 133]. The effective interfacial viscosity that I measure, $4.9(3) \times 10^{-5}$ Pa.m.s is, as expected, larger than what was measured at the lower surface fraction.

5.4.4 Oscillatory Rheology

Firstly, it is important to measure the surface fraction in this experiment. Using the white pixel method the surface fraction is found to be 60.0%. Note that this surface fraction has a much lower variability than those measured in the

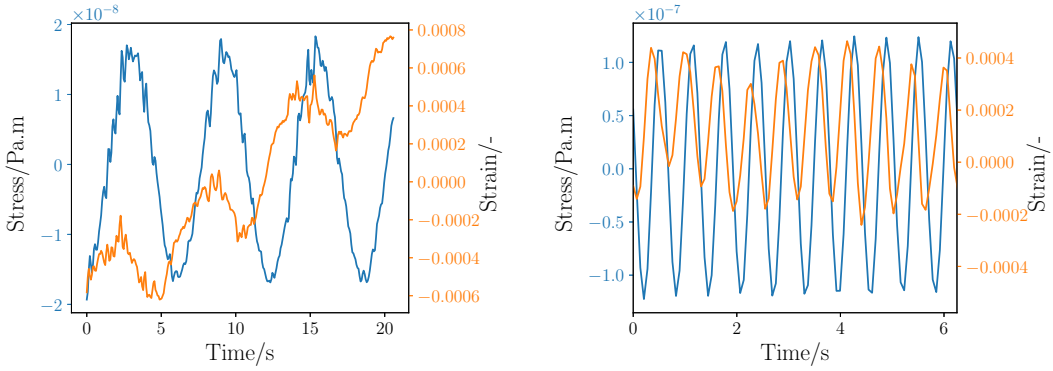

(a) **(b)**

Figure 5.11 *Results of oscillatory rheology of a dodecane-water interface laden with PMMA-PLMA particles at 60% surface coverage showing the driving stress (blue curves) and the strain response (orange curves). (a) is at a driving frequency of 1.0 rad s^{-1} and (b) is at a driving frequency of 10 rad s^{-1}. Both experiments are performed with a strain amplitude of the rheometer head of 0.1%.*

steady state experiments. This is because, while the steady state experiments sample a full ring of the interface, in oscillatory measurements, the same part of the interface is only ever visible, with some variation due to the oscillation. Therefore, the value of 60.0% here is only the value of surface fraction which is observable in the microscopy setup.

The comparison of stress and strain versus time shows a puzzling discrepancy (representative results are shown in figure 5.11). The first thing to note is the agreement in driving frequency and response frequency, both of which align with the imposed frequency of the rheometer. There is also a deviation of the response curves (strain, orange curves) from a perfect sinusoid, this systematic drift can arise from, for example, thermal gradients in the sample or air flows in the laboratory. Nevertheless, the fitting procedure captures the important aspects of the curve, namely the frequency, phase, and amplitude of the oscillation. However, qualitatively it is apparent that the response is ahead of the drive (stress, blue curves). Clearly, this is an unphysical situation which is confirmed by fitting the curves to sinusoids and measuring δ; in all but one set of data δ is found to be negative.

Clearly, a negative value for δ is unphysical, however I note that δ has a periodicity of 2π, and so it must be the case that the response lags behind the driving force with a surprisingly large phase. Physically, the phase lag must be between 0 and

$\pi/2$, the extra lag that I measure comes from the time taken for the stress to propagate through the oil phase from the rheometer to the oil-water interface. *A priori* this extra phase lag is not known however the measured δ values fall in a range which can be shifted towards $0 < \delta < \pi/2$ which will give some indication of the phase lag due to the stress propagation. Values of δ and the corrected phase lag to preserve physicality, δ^*, are given in Table 5.1, where errors are given for the corrected phase lag based on the maximum and minimum possible values.

The correction factor, φ, to obtain δ^* from δ must then be the phase lag arising from the stress propagation through the oil phase. I can measure this to be $\delta^* - \delta$, up to any addition of 2π, leading to a propagation phase lag of 5.0±0.2. In other words, in order for the data to be physically possible, the strain response must first be shifted by φ such that

$$\gamma^* = \gamma_0 \cos(\omega_\gamma(t + \Delta t_\gamma) + \varphi) \tag{5.21}$$

and therefore

$$\delta^* = \omega(\Delta t_\sigma - \Delta t_\gamma) - \varphi + 2k\pi, \tag{5.22}$$

where k is an integer such that $0 < \delta^* < \pi/2$. Using the value for δ^* in equation (5.9) leads to a plot of G' and G'' against frequency at a strain amplitude of 0.1% (figure 5.12). There seems to be no obvious correlation between G' and G'', particularly at low frequency. However, if one considers that the data point at 1.6 rad s^{-1} is an outlier on the curve, then there is consistency in that $G'' < G'$ up to 6.3 rad s^{-1} where G'' becomes larger than G'. In addition, G' remains roughly constant throughout the frequencies probed other than the outlier at 1.6 rad s^{-1} already mentioned.

Table 5.1 *Apparent values for the phase lag, δ, during oscillatory rheology at an oscillation amplitude of 0.1% strain and an oscillation frequency as given. δ^* is the phase lag after being corrected to ensure all values of δ fall between 0 and $\pi/2$.*

Frequency/rad s^{-1}	δ	δ^*
1.0	4.25	0.5±0.2
1.6	5.07	1.3±0.2
2.5	4.49	0.7±0.2
4.0	4.00	0.2±0.2
6.3	4.63	0.8±0.2
10	4.95	1.2±0.2
16	5.13	1.3±0.2

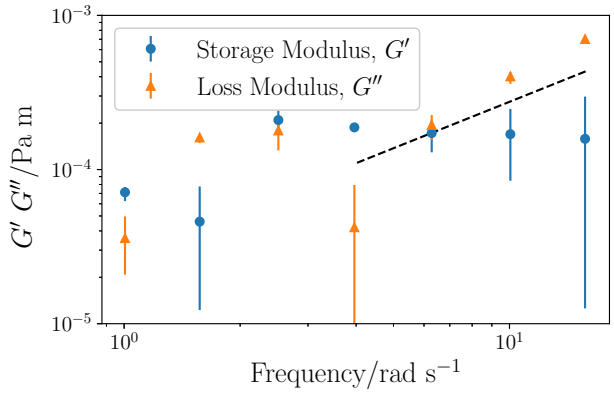

Figure 5.12 *Storage modulus (blue ○) and Loss modulus (orange △) versus frequency for a PMMA-PLMA laden dodecane-water interface at a surface fraction of 60%. The dashed line is a line of gradient 1 to show that G'' approaches a linear dependence on frequency at high frequency.*

It is worth considering here the physical origin for the magnitude of these moduli. Taking a value of 10^{-4} Pa m from figure 5.12, we can convert this to an energy scale by multiplying by an area. The relevant areas here are the particle surface or the cross-sectional area which are both on the order of 10^{-11} m^2. Therefore we find an energy scale of 10^{-15} J, or 2.5×10^5 $k_\mathrm{B}T$. There are two possible sources for this energy; firstly, the interparticle interactions measured in Chapter 3 which have not been measured at very close contact, at a core to core separation of 2 particle diameters this energy has been measured as 120 $k_\mathrm{B}T$. This is considerably lower than the energy required to provide the measured storage modulus, however the interparticle energy will be much larger at separations close to contact. The second source of energy is in contact line sliding or deformations of the liquid interface which have recently been shown to contribute to surface pressure measurements in these systems [109]. In this case, the energies are on the order of the product of the water-oil surface tension and typical deformation areas (which will be on the order of a particle if particle-particle contacts cause deformations normal to the interface). Typical values of this would then correspond to $10^5 - 10^6$ $k_\mathrm{B}T$.

Here I have assumed that the φ to bring δ into the range $0 < \delta < \pi/2$ is constant across all frequencies measured. However, I can also consider that it takes finite time for stress to propagate through a height. This time can be found using [124]

$$\tau \simeq \frac{10\rho h^2}{\eta}, \tag{5.23}$$

where ρ is the density of the fluid, h is the depth of the fluid, and η is the viscosity of the fluid. This relationship is applicable for narrow gap flows. Using the values for dodecane in my setup, I find that $\tau \simeq 20$ s. Then, considering that δ leads to equivalent fits to the data presented in figure 5.11 up to an additive contribution of 2π, a reasonable assumption would be that

$$\delta + 2n\pi = -\omega\tau, \tag{5.24}$$

where n is an unknown integer. Crucially, τ should give the same value across all δ values. Indeed, when finding τ via

$$\tau = -\frac{\delta + 2n\pi}{\omega}, \tag{5.25}$$

for different ω, each dataset leads to a similar value of τ of ~ 20 s, as predicted. This lends confidence to the applicability of using equation 5.23 as I get good agreement between experimental and calculated values for τ. The n required for each ω is given in Table 5.2.

It is noteworthy that the value of n required to measure τ increases with the same geometric spacing as the value of driving frequency. This is because n measures the number of periods of the oscillation over which the lag time occurs where the number of periods is also proportional to ω^{-1}. With the large value of lag time relative to one period of oscillation in mind, it seems that the results in figure 5.12 should be taken cautiously. While the value for $|G^*|$ should be measurable in this setup, appropriate values for δ are not easily determined.

Table 5.2 *Calculated time lag, τ, based on the idea that the time lag should not depend on the oscillation frequency. This is found by adding $2n\pi$ to the values for the phase lag before dividing by the driving frequency.*

Frequency/rad s^{-1}	n	τ/s
1.0	-4	20.8
1.6	-6	20.8
2.5	-9	20.7
4.0	-14	21.2
6.3	-22	21.3
10	-34	20.8
16	-53	20.9

I have shown here that, while oscillatory rheology may be possible, to understand the results an inference has to be made on the effect of the finite time for the stress to propagate from the rheometer head to the oil-water interface. It would be interesting for further studies to look at how altering the height of the oil phase would affect the measured propagation phase lag. Other physical parameters which could be altered would be the density and viscosity of the oil phase, however these may change the intrinsic rheological properties of the particle laden interface itself and therefore any such studies should be attempted with caution.

5.5 Conclusion

In this chapter, I have described the development of a novel method to perform interfacial rheology without an interfacial geometry. This allows interfaces to be probed in a less intrusive and more industrially relevant manner than other, more direct methods. This method is relevant to applications where a system of large interfacial area is sheared, the shear being applied to the continuous phase and indirectly deforming the interface. I have demonstrated that this method allows me to measure rheological properties such as interfacial viscosity or yield stress depending on the surface fraction and the results align favourably with literature values. My contactless setup allows me to measure interfacial viscosities at much lower surface fractions than have been previously observed, owing to the high sensitivity achieved by having no probe attached directly to the interface.

The setup allows me to link the rheological behaviour to the structural behaviour of the interface. I showed that, at low surface coverage, the interface behaves as a two dimensional Newtonian fluid and is subject to aggregation above a certain shear threshold. At higher surface coverage the interface begins to behave as an elastic sheet with a measurable shear modulus, up to a yield stress where the interface begins to flow. Interestingly, I observed that even above this yield stress, there is still some elastic behaviour present in the interface. In addition, I have shown that at low surface coverage, the interfacial structure has a strong effect on the rheology.

This chapter has focussed on the motion of the particles in the plane of the interface under steady shear. The effect of the interface on how shear is propagated from the oil to the water phase will be the topic of the next chapter, this can relatively easily be achieved through this setup, unlike systems where a

probe is attached directly to the interface.

Chapter 6

Speed Profile across a Particle Laden Interface

6.1 Abstract

In this chapter, I use the indirect interfacial shear rheometer described in Chapter 5 to measure stress propagation across a particle-laden oil-water interface. Using this setup, I shear the upper phase and observe the response at the interface as well as in the lower water phase using a low volume fraction of fluorescently labelled, charge stabilised PMMA particles. I show that the rheological behaviour of the liquid-liquid interface strongly affects the propagation of stresses across that interface. Using a velocimetry technique, the interface can be characterised as either viscous, where the interface flows in the direction of shear, or elastic, where the interface resists any deformation and returns to its original position upon cessation of shear. For a viscous interface, there is considerable flow in the lower phase, implying that a viscous interface does little to prevent stress propagation. However, for an interface with a yield stress the response of the lower phase follows that of the interface, where there is no apparent viscous behaviour up to the yield stress, i.e. the interface "shields" the lower phase from stresses. This has important consequences for droplet-like systems in external flow fields where the internal phase of a droplet or cell may need to be shielded from external stresses.

6.2 Introduction

The flow behaviour of systems with large interfacial area is affected by the rheological properties of the interface itself [2, 3]. Previous studies have considered the rheological properties of an emulsion, for instance to measure how these systems differ from solid-particle dispersions [34], or to investigate the stability of emulsions based on oscillatory rheology measurements [134]. As well as investigations on the rheology of emulsions, numerous studies have investigated the rheology of the interface itself, as described in more detail in Chapter 5 [10, 54, 57].

Emulsions can be used for transport purposes, moving hydrophobic substances through a water continuous phase. This allows emulsions to be used for various surface treatments, such as painting, paper coating or road surfacing, where the continuous water phase is allowed to evaporate leaving behind a hydrophobic coating [135]. Moreover, these systems are well suited for drug delivery [136], for example, controlled delivery of caffeine to the skin has been shown previously to be 3 times faster from a Pickering emulsion rather than a surfactant stabilised emulsion [137]. In some cases, drug delivery is based on the response of the active ingredient to external stresses, for example, aggregates of nanoparticles have been designed to break up under high shear stresses for targeted drug delivery in blood vessels [138] and there have been studies looking at the shear dependence of antithrombotic drug efficacies [139]. Therefore, understanding how external shear flows, such as in blood vessels or applied to topical medications, affect the internal shear in an emulsion droplet used for drug delivery is essential to fully understand the efficacy of this delivery method.

Another area where interfaces play a key role is in biological cells. These consist of an internal phase separated from an external phase by a lipid bilayer. As opposed to emulsions, the internal and external phases in cells have the same fluid background, namely water, with different molecular constituents. The cytoskeleton is primarily responsible for the structure and mechanical properties of a cell, it consists of numerous entangled protein filaments which act together to provide structural integrity and rigidity [140]. However, cells can be subjected to large mechanical stresses and the response of the cytoskeleton, even before considering the complexities of how those stresses are propagated across the lipid bilayer into the cell, can be particularly complex [141].

One aspect of the response of interfaces to external shears has previously been observed via "tank treading", so called as the interface moving around a curved surface resembles tank treads in motion. In lipid vesicle systems or red blood cells, the interface flows under external shear [37–39]. However, for particle stabilised droplets, the "tank treading" behaviour is no longer observed [40]. In order to probe these systems in a systematic manner, it is useful to consider a planar interface, where the rheological behaviour can be tuned by varying the particle surface coverage.

In this chapter, I will describe a method for characterising how stresses propagate across a complex fluid interface. I use a planar interface to model the surface of an emulsion droplet and apply a stress to the upper phase which models the continuous phase. The response of the lower phase is then measured using tracer particles and confocal microscopy. I find that the rheology of the interface plays a key role in how stresses propagate across that interface. If the interface undergoes flow, then the lower phase is also subject to that flow; the interface does little to "shield" the lower phase from external stresses. However, if the interface behaves as a 2 dimensional elastic sheet, it "shields" the lower phase from external stresses and the lower phase exhibits no apparent viscous behaviour. This helps understand observations in emulsions science, where it has been observed that particle stabilised emulsion droplets have a stiff interface which resists motion [40], whereas the surfaces of vesicles made from lipid solutions [39] or the surfaces of red blood cells [37, 38] flow under external stresses.

6.3 Materials and Methods

The materials and methods not specific to this chapter are described in chapter 2. In this section methods which are specific to this chapter are described.

6.3.1 Materials

The interfacial particles used in this section are labelled as ASM628. The particles used as tracer particles in the water phase are labelled as ASMMAF5. For the particle properties see Table 2.1.

6.3.2 Sample Preparation

Interfaces were prepared following § 2.3.1 with surface fractions of $44.5 \pm 1.4\%$ and $36.5 \pm 6.8\%$ of particles from batch number ASM629, measured using the pixel fraction method, described in § 5.3.1. The water phase was a dispersion of fluorescent charge stabilised PMMA particles (ASMMAF5) at a volume fraction of $\sim 0.003\%$.

6.3.3 Image Acquisition

Images were acquired in one of two ways. For the lower surface fraction experiments, a logarithmically spaced shear rate between 0.010 revolutions per minute (rev/min) and 2.5 rev/min with 5 shear rates per decade was applied for 5 minutes at the oil-air interface. z-stack videos were taken with a step size of 15 μm and 7 slices for 50 s each, the small step size was used to make use of the piezzo z-control, allowing for high frame rate z-stacks. Videos were first taken at the interface to capture the start of the shear, then videos 600 μm below the interface were taken, and finally another video at the interface was taken to capture the end of the shear.

For the higher surface fraction experiments, a logarithmically spaced shear rate between 0.10 rev/min and 4.0 rev/min with 5 shear rates per decade was applied for 30 s at the oil-air interface. Videos of a single plane were taken for 40 s to capture the start and end of the flow. The focus was then changed to inside the water phase and again a video of a single plane was taken for 40 s. The separation between subsequent planes in the water phase was 150 μm. During the experiment, the z-position of the interface gradually decreased due to evaporation so the gap between the interface and the higher plane in the water phase gradually decreased from 259 μm to 175 μm. 5 planes were imaged: 1 at the water-oil interface and 4 at subsequent heights in the water phase. For the highest speed of rotation, 9 planes were imaged in the water phase, rather than 4, with the separation maintained at 150 μm between subsequent planes.

In both cases, for each z-position videos were analysed using C code written by Dr Michiel Hermes. This code first splits the frames into 10 horizontal bands. Each band is correlated with the previous frame with a horizontal offset; the offset which maximises the correlation is then the horizontal displacement, x_h, between

that frame and the previous frame. This algorithm was also applied in the vertical direction to measure the vertical displacement, x_v. The total displacement is then found by summing these in quadrature, i.e. the total displacement is

$$x_T = \sqrt{x_h^2 + x_v^2}. \tag{6.1}$$

Instantaneous speeds were also found from $x_T(t)$ plots using the gradient function in numpy. To remove artefacts of the image analysis code, any speed, $v(t)$, more than 3 standard deviations from the mean of the surrounding 10 speeds was discarded, i.e. if

$$|v(t) - \overline{v_{t10}}| > 3\sqrt{\frac{1}{9}\sum_{n=-5,n\neq 0}^{5}(v(t+n\delta t) - \overline{v_{t10}})^2}, \tag{6.2}$$

with

$$\overline{v_{t10}} = \frac{1}{10}\sum_{n=-5,n\neq 0}^{5} v(t+n\delta t), \tag{6.3}$$

where δt is the time between frames. This ensures that only data outwith a 99% confidence interval will be discarded. In addition, speeds were averaged over 3 neighbouring data points to smooth out the data.

6.4 Results

6.4.1 Lower Surface Coverage

I have measured x_T versus time for the start of shear near the interface, the middle of shear in the bulk water phase, and the end of shear near the interface. Example plots at two rotation speeds of the rheometer (0.10 rev/min and 1.6 rev/min) are shown in figure 6.1.

Especially at the lower rotation speed, there are some artefacts of the analysis which appear (e.g. large jumps in x_T), so I have also plotted the instantaneous speed as a function of time, using the filtering procedures described in the methods. Example plots at two rotation speeds of the rheometer (0.10 rev/min and 1.6 rev/min) are shown in figure 6.2.

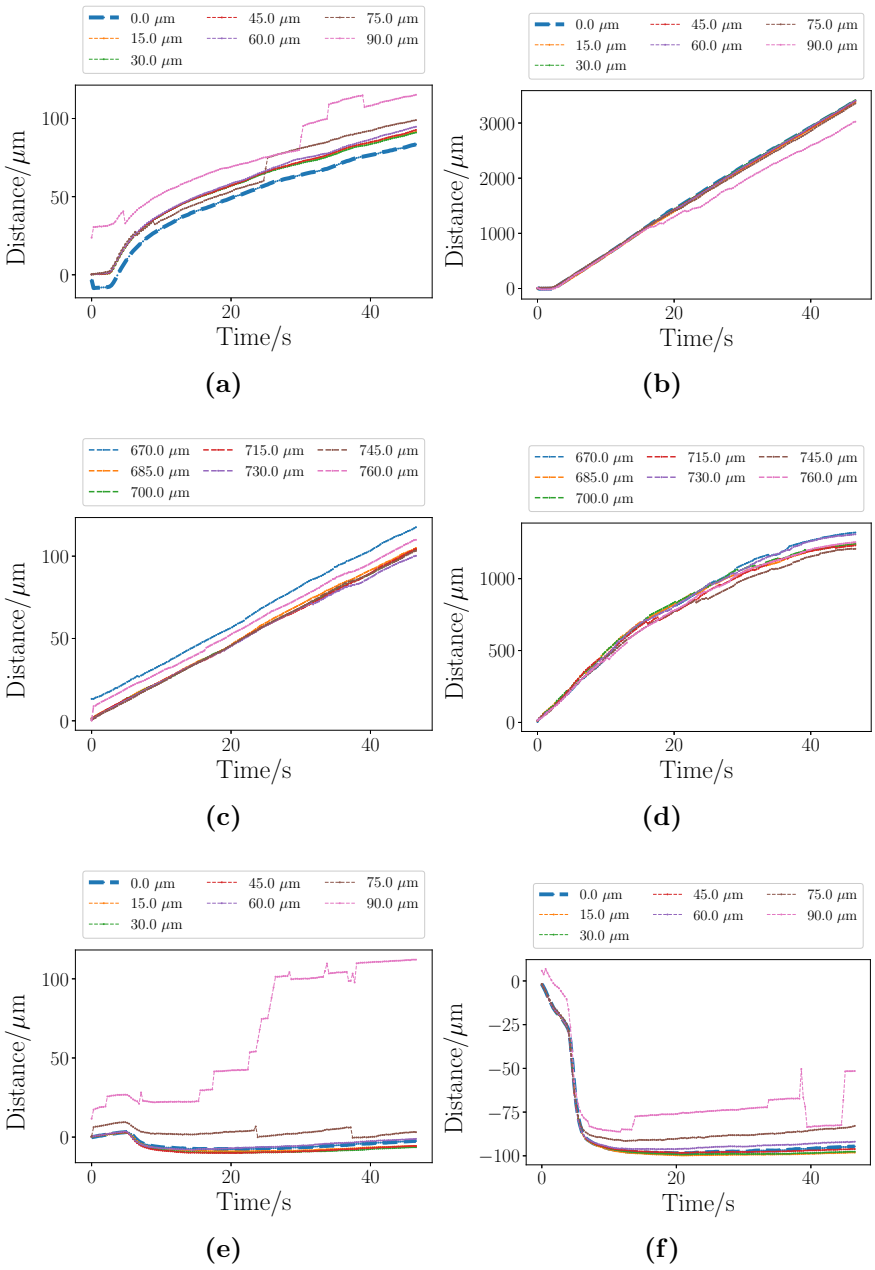

Figure 6.1 *(a)-(b) Plots of distance versus time at the beginning of the shear at the particle-laden water-oil interface (thicker line) and at 6 slices below the interface spaced 15 μm apart; (a) at a rheometer rotation speed of 0.10 rev/min, and (b) at a rheometer rotation speed of 1.0 rev/min. (c)-(d) Plots of distance versus time during shear at 7 slices 700–790 μm into the water phase; (c) at a rheometer rotation speed of 0.10 rev/min, and (d) at a rheometer rotation speed of 1.0 rev/min. (e)-(f) Plots of distance versus time at the end of the shear at the water-oil interface (thicker line) and at 6 slices below the interface spaced 15 μm apart; (e) at a rheometer rotation speed of 0.10 rev/min, and (f) at a rheometer rotation speed of 1.0 rev/min. The legend refers to the depth below the water-oil interface. The particle surface fraction was 36.5%. Note that in each panel distances are such that $x(0) = 0$ in that panel.*

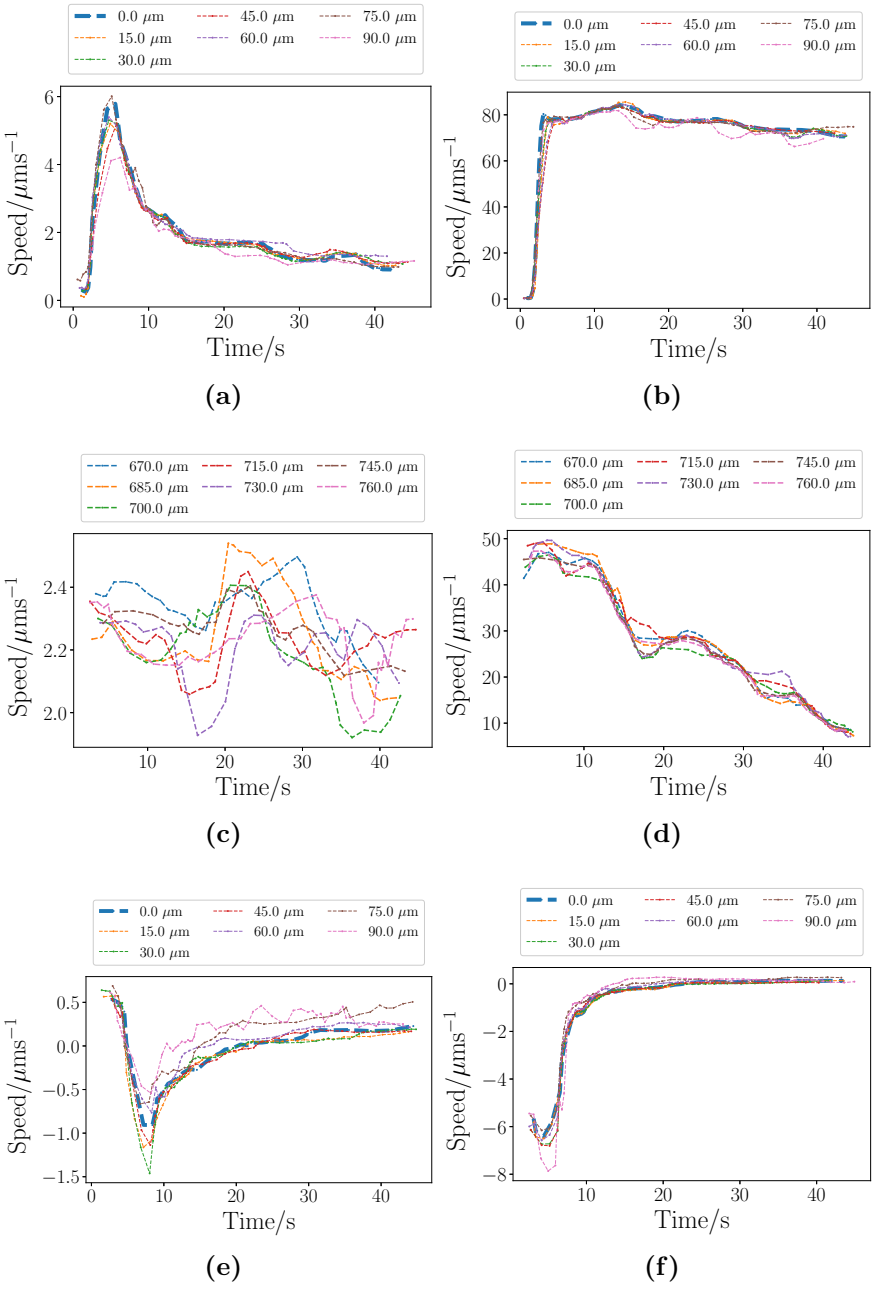

Figure 6.2 *(a)-(b) Plots of speed versus time at the beginning of the shear at the particle-laden water-oil interface (thicker line) and at 6 slices below the interface; (a) at a rheometer rotation speed of 0.10 rev/min, and (b) at a rheometer rotation speed of 1.0 rev/min. (c)-(d) Plots of speed versus time during shear at 7 slices 700–790 μm into the water phase; (c) at a rheometer rotation speed of 0.10 rev/min, and (d) at a rheometer rotation speed of 1.0 rev/min. (e)-(f) Plots of speed versus time at the end of the shear at the water-oil interface (thicker line) and at 6 slices below the interface spaced 15 μm apart; (e) at a rheometer rotation speed of 0.10 rev/min, and (f) at a rheometer rotation speed of 1.0 rev/min. The legend refers to the depth below the water-oil interface. The particle surface fraction was 36.5%.*

The $x(t)$ plots in the middle of the experiment (figures 6.1c and 6.1d) show that the lower phase has a finite flow speed, i.e. the lower phase acts as a viscous fluid rather than an elastic material. However, recoiling behaviour seen at the end of the flow (figures 6.1e and 6.1f) imply that the interface has some elastic properties as well [129]. This combination of viscous and elastic behaviours in steady shear experiments has been seen previously in Chapter 5. The plots of $v(t)$ verify this, with peaks of speed at the start of shear, finite speeds in the lower phase in the middle of the shear, and troughs in speed (negative "peaks") at the end of shear. The peak height at low rotation speed in $v(t)$ slightly decreases as I measure deeper into the lower water phase.

6.4.2 Higher Surface Coverage

Again, at the higher surface coverage I have measured $x(t)$ curves. In this case, the elastic behaviour of the interface makes measurements of speed less useful so these are not included here. Example plots at four rotation speeds of the rheometer (0.10 rev/min, 0.40 rev/min, 1.0 rev/min and 2.5 rev/min) are shown in figure 6.3.

At each rotation speed shown, the $x(t)$ curves show "frustrated motion", i.e. the interface and the lower phase exhibit both forwards and backwards motion when subjected to shear in only one direction. Especially at the 2.5 rev/min, there is evidence of initial elastic "jumps" at the beginning of shear, and also elastic recoils at the end of shear. Note that the responses are not perfectly correlated as each $x(t)$ line is taken from a separate application of shear, and due to the stochastic nature of the rearrangements each separate application is not correlated.

6.5 Discussion

6.5.1 Lower Surface Coverage

Firstly, we note that the $x(t)$ data exhibits large, unphysical jumps in the data which arise due to errors in the velocimetry code, e.g. in the $x(t)$ curve 90.0 μm below the interface in figure 6.1e. As the image data can be quite noisy for highly covered interfaces, there can be cases where a large horizontal offset coincidentally

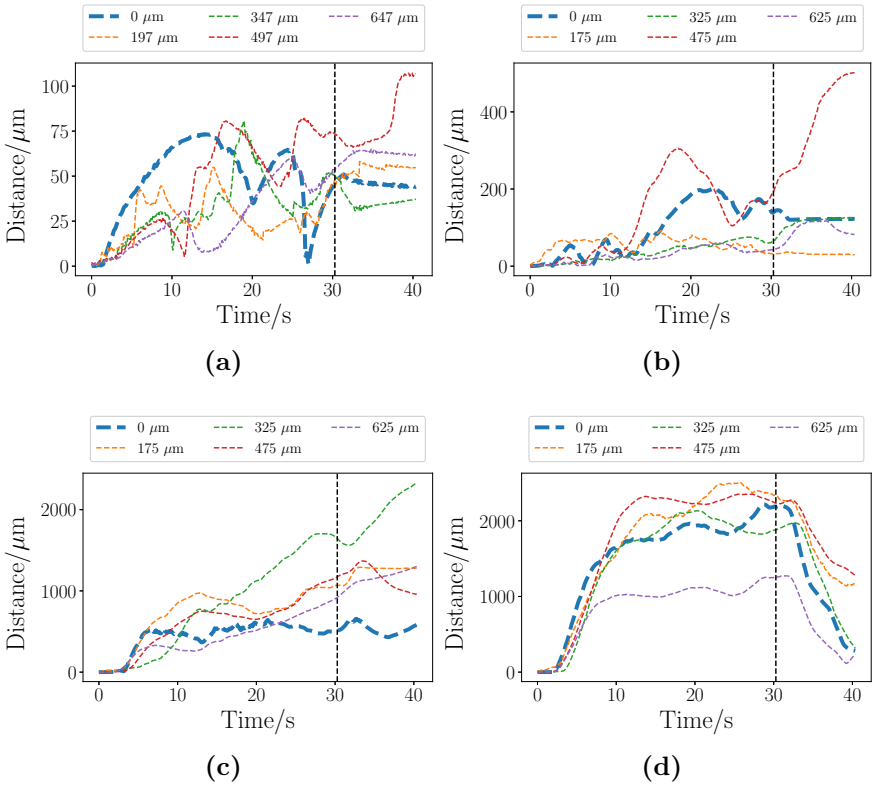

Figure 6.3 *Plots of distance versus time at the particle-laden water-oil interface (thicker line) and 4 distances into the water phase. The rheometer rotation speed was fixed at (a) 0.10 rev/min, (b) 0.40 rev/min, (c) 1.0 rev/min, and (d) 2.5 rev/min. The dashed vertical line represents the approximate time at which the rheometer rotation speed is set to 0. The legend refers to the depth below the water-oil interface. The particle surface fraction was 44.5%.*

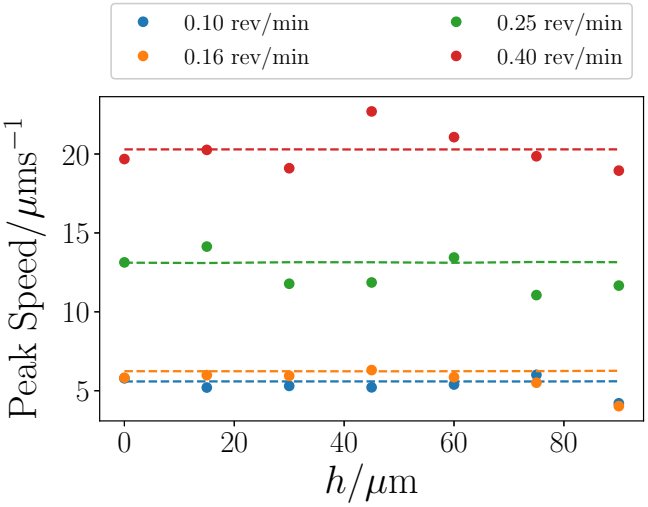

Figure 6.4 *Subtle negative trends in peak speed against depth into the water phase, h, are present as indicated by the linear fits to the data. The gradients of the trendlines are: -0.007±0.007 (0.10 rev/min), -0.015±0.008, -0.021±0.012, -0.002±0.018.*

has a higher correlation than the actual horizontal offset. This could be corrected for by limiting the distance moved to values based on neighbouring distances. Here, we correct for this by considering speed versus time plots, rather than distance versus time, using the gradient function in numpy, then filtering out gradients outwith 3 standard deviations of the neighbouring points.

The velocimetry data at the start of the shear at low rotation speed shows no discernible trend as we observe further into the water phase. I would expect the maximum speed to decrease as I measure deeper into the water phase, however a plot of peak speed against depth into the water phase at low rheometer rotation speeds (figure 6.4) only shows a subtle negative correlation, with the gradients of the best fit being negative but often within error of zero. The combination of elastic and viscous behaviour, i.e. an initial elastic response before flow takes over, has previously been observed in Chapter 5. The surface fraction here is between the surface fractions where pure viscous behaviour is observed and where yield stress behaviour is observed. The combination of elastic and viscous behaviour observed here is more comparable to the higher surface fraction, i.e. yield stress behaviour, than the lower surface fraction. This might indicate that this interface does have a finite yield stress which is lower than the lowest stress applied.

As well as the possible trend present in these plots, an important qualitative note is that the behaviour in the water phase follows closely the behaviour of the interface. While the interface has some elastic properties, i.e. the peak in

speed, the water phase, which is Newtonian, also acquires some elastic strain. This strain must be supported entirely by the interface as a Newtonian liquid cannot support a finite shear strain, only a shear strain rate. At the end of shear this elastic behaviour, both of the interface and of the bulk, is also present, clearly visible from the negative speed, i.e. a recoil effect [129]. Here again I see that there is a small trend as we observe further into the water phase, with a shallower trough depth further into the water phase. I also see the elastic behaviour in figure 6.1a from the flattening of the $x(t)$ curve, indicating an initial jump in x followed by a transition to a lower constant flow speed, and additionally in figure 6.1e from the recoil, the relative distance measured moving to negative values. In fact, this recoil is seen across all rotation speeds of the rheometer ($v(t)$ curves not shown).

Considering the data regarding the bulk water phase, there is very little that can be inferred, with no real trend present as we look at different slices (figure 6.2c). It is interesting to note that, while the speeds in the water phase are significantly lower than the peak in figure 6.2a, the speeds are comparable, if not higher, than the plateau value in figure 6.2a. This might indicate that there was some rearrangement of the interface on timescales longer than the 40 s presented here, or that there is some systematic drift caused by, for example, temperature variations in the sample. While the laboratory is air conditioned, the confocal microscope's laser might locally heat parts of the sample.

At higher rotation speeds different behaviour is observed. At the start of shear, the $v(t)$ curve shows no observable elastic response of the interface implying that this rotation speed is above the yield stress of the interface. Here I observe no particular trend over the ~ 90 μm z-range that is probed. The lowest depth into the water phase appears to have a slightly lower speed than the other z-depths; this single depth being separate from the rest seems to occur more often across data sets implying that there is some typical lengthscale over which stresses do not decay beyond the interface.

In the bulk water phase there is again no particular trend. In the example shown in figure 6.2d, the speed varies over time, with a decreasing trend, however this data set appears to be anomalous. The rest of the data at different rotation speeds (not shown) also exhibits variation in speeds over the experimental time frame, but none are as large as the factor of 5 decrease seen in figure 6.2d, with the next largest change being a factor of $\sim$2. This variation over the experimental time frame could arise due to heterogeneities in the interfacial structure, or changes in

the interfacial structure over time. As discussed in Chapter 5, structural changes to the interface have an effect on the interfacial rheology at low surface fraction (see figure 5.9).

At the end of the rotation, the interface seems to have a recoil similar to that seen at the lower rotation speed (figure 6.2e). Similarly to the start of rotation and the bulk data, there is no obvious trend across the depth of the water phase in this case.

These observations indicate that, in the case of an emulsion droplet, there would be significant internal droplet flow if the surface of that droplet can also flow. This would be the case for interfaces where tank treading is observed, such as lipid vesicles [39], red blood cells [37, 38], or partially coated emulsion droplets, where I have shown that the interface can flow at low surface coverage in this chapter and in Chapter 5[1].

6.5.2 Higher Surface Coverage

At the higher surface coverage at every rotation speed up to 2.5 rev/min of the rheometer the interface behaved in an elastic fashion, i.e. the data are taken below the yield stress of the interface. While the $x(t)$ curves do not necessarily show *ideal* elastic behaviour (where the position returns to 0 after ending the stres), the erratic motion and the lack of flow (i.e. a constant flow speed) infer elastic behaviour rather than viscous behaviour. In general there is no obviously discernable trend as the depth into the water phase varies. Especially at low rotation speeds, there is a lot of frustrated motion implying that under moderate shear the interfacial particles can rearrange to relieve stress. The frustrated motion is seen in the $x(t)$ curves, which show random motion where the system often moves against the applied stress from the rheometer. This is more obvious at this high surface fraction than the previously observed frustrated motion in Chapter 5 in the elastic regime.

Considering the results in the bulk water phase, the interface shields the water phase from the stress in the oil phase and then propagates stress dependent on the interfacial response. There are two convincing pieces of information from these data to confirm this statement. First, at a rheometer rotation of 2.5 rev/min the

[1] In practice, partially coated Pickering droplets can be transient as they are unstable against coalescence

$x(t)$ plots are reminiscent of an elastic solid. Considering that the phase here is water and so should behave as a Newtonian liquid, I can infer that the behaviour of the water phase is entirely based on the interface. Note that, while the lower phase does not flow (relative to the interface) under the external stress, there is still motion in the lower phase, however this is purely an elastic motion mimicking the elasticity of the interface - an important distinction here is that motion does not necessarily mean flow. This has important consequences for applications where an emulsion system is sheared and the response of the internal phase to deformation affects the desired behaviour of the emulsion.

The second piece of information that confirms the bulk rheology is almost entirely dependent on the interfacial rheology comes from the frustrated motion that can be seen. The frustrated motion due to rearrangements leads to the interface sporadically moving both with and against the direction of shear, although the dominant direction is with the shear, especially the initial elastic response. This forward and backward motion of the interface is reflected in the response of the water phase, which may be unexpected when we consider the water phase as a bulk Newtonian fluid. Recall that the bulk response and the interfacial response are not perfectly correlated as each $x(t)$ line is measured from a separate application of shear in this methodology.

Finally, the data at 4.0 rev/min, shown in figure 6.5, aligns with the results from the lower surface coverage experiments. At this rotation speed, the interface appears to have yielded, leading to flow at all measured depths into the water phase. The distinction between whether an external stress causes the lower phase to flow relies on the yield stress of the "shielding" interface, rather than simply a question of the surface coverage.

The result of the planar interface completely resisting an external shear aligns with the lack of "tank treading" behaviour seen in [40]. The unique planar geometry I use allows me to infer that, under the conditions of no tank treading, an external shear results in limited shear internal to the droplet. This might have implications for delivery applications, for example, using bijel capsules where the internal bijel has a low yield stress so requires further protection from external stresses until arriving at the delivery target [142]. These results imply that the only internal response would be elastic, matching that of the droplet surface. To verify this, similar experiments would be required in a counter rotating rheometer with a particle coated emulsion droplet centred on the plane of zero motion, while simultaneously imaging with a confocal microscope.

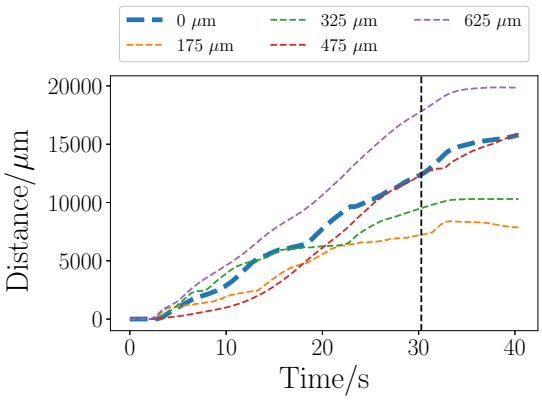

Figure 6.5 *Plot of distance moved by the interface vs time for a particle-laden oil-water interface at a surface fraction of 44.5% showing the flowing behaviour at all heights into the lower phase. The interface (thicker line) and 4 depths into the water phase are shown. The rheometer attached to the oil-air interface is rotated at 4.0 rev/min. The legend refers to the depth below the oil-water interface.*

6.6 Conclusion

In this chapter I have shown that the rheological behaviour of a particle laden interface strongly affects the propagation of stresses across that interface. Quantitative measures of speed at different depths show that if the interface behaves as an elastic fluid then the stresses from the upper phase have little effect on the flow of the lower phase, although there is still elastic motion in the lower phase following the elastic interface. On the other hand, if the interface flows, then there is considerable flow in the phase below the interface, this may be as the interface does little to "shield" the lower phase from external stresses. On the other hand, this could be because, as in the case of an elastic interface, the lower phase follows the interface; as the interface is viscous in this instance the lower phase is also observed to be viscous. The results have not been conclusive in finding trends in speed profiles as measurements are made deeper into the water phase. One possible trend is in the highest reached speed, which decreased as measurements were made further into the lower phase.

The qualitative observation of the interface "shielding" the lower phase from external stresses has large consequences for systems with an interface that can resist flow. This has obvious consequences for emulsions where the internal phase has a stress-sensitive ingredient, which may be the case in certain drug delivery applications. In addition, this behaviour would have important consequences

for biological cells, where the internals of the cell may be protected from large external stresses which can occur in the body if the interface can resist deformation.

Chapter 7

Conclusions and Outlook

In this thesis I have investigated the structural and rheological behaviour of a particle laden fluid interface. Firstly I have characterised the interface in a quiescent system, before probing the rheological response using a novel, industrially relevant contactless interfacial rheology technique.

In Chapter 3 I presented experimental results measuring the interparticle potential between (uncharged) sterically stabilised PMMA particles adsorbed at a water-oil interface. I showed, using complementary techniques of $g(r)$ inversion and a blinking optical trap (BOT), that the interaction can be well described by a single screened monopolar potential, rather than a dipolar potential which has been previously reported for charge stabilised particles at fluid interfaces. Additionally, theoretical work has shown that either a screened monopolar or a screened $\frac{1}{r^2}$ potential can be shown to hold at different lengthscales for point charges at a liquid-liquid interface. I argue that this model holds for uncharged interfacial particles as they behave as neutral holes in the charged plane of the interface. Bayesian analyses of experimental data showed that the theoretically derived screened $\frac{1}{r^2}$ term also provides a decent fit, and can quantitatively outperform the screened monopolar model at larger separations. Additionally, the screened $\frac{1}{r^2}$ term provides more physically reasonable trends in screening length, κ^{-1}, and the strength of the interaction.

While some work was presented on the effect of salt concentration and pH of the water phase, further work could investigate any trends in these parameters more closely. For instance, the pH results presented here were at comparably low surface fraction, leading to limited data at low separation. Additionally, it could

be enlightening to perform direct measurements of the interparticle potential (e.g. using a BOT) under conditions of changing salt concentration and/or pH. However, the results presented in this regard remain consistent with the physical model of neutral holes adsorbed to a charged interface.

Following these results, in Chapter 4 I presented Monte Carlo simulations of a bimodal size distribution of particles in a 2d plane interacting via the screened monopolar potential found in Chapter 3. I showed that particles interacting with the potential described by the neutral holes model show no long range order and little short range order. This is in contrast to particles interacting with a dipolar potential which have been shown in the literature to have well-ordered binary structures. I also investigated the effect of the loading conditions on the final structures observed. I found that at low surface fraction, a sequential deposition of particles lead to a greater local hexagonal ordering than the particles all being loaded at one time. On the other hand, at higher surface fraction the sequential deposition method lead to less local hexagonal ordering. I attribute this effect to particles becoming stuck in areas of the same size particle at high surface fraction in a one step deposition, while in a sequential deposition the larger particles can first rearrange to have larger spacings before the smaller particles are introduced. This phase separation would lead to greater local hexagonal arrangements but little long-range order. Experimental work investigating the structure of these simulated bimodal interfaces would be useful to lend confidence to the simulated results presented here. Additionally, comparisons of these simulations against dipolar potentials with similar interaction strengths as the screened monopolar potential used here would be helpful for further comparison with literature studies.

In Chapter 5 I described a novel method which I developed to probe the rheological response of the particle laden interface which requires no probe attached directly to the interface. I have argued that this method is relevant for many applications of systems with large interfacial areas, such as the application of skin creams, where the continuous phase is sheared which indirectly transfers shear on to the interface. Additionally, the interface probed is purely a particle-laden interface with no probe attached which can affect rheological measurements. The technique I have employed uses a standard rotational rheometer attached to a confocal microscope such that the response of the interface to shear of the upper, oil phase can be tracked.

Using this technique I have measured steady shear material properties of a

PMMA particle laden interface. My results for interfacial viscosity and interfacial shear modulus are consistent with previous literature studies and I show that my technique can measure viscosities significantly lower than those previously reported. The inherent simultaneous imaging means that my technique lends itself to simultaneous structural analysis. I showed that the structural properties of the interface have an effect on the shear behaviour and therefore the results from Chapter 4 become particularly relevant. I also showed that shearing the interface can lead to irreversible structural changes which will therefore irreversibly change the rheology of the interface.

Chapter 5 also described some preliminary measurements of oscillatory rheology using the indirect interfacial rheometer. I showed that the physical interpretation of these results is difficult due to the finite time for stresses to propagate through the oil phase, which while not important for steady shear experiments given enough time, is inherently important for oscillatory measurements. Further work looking at this effect could determine a method for extracting important information, for instance decreasing the height of the oil phase might bring the results more in line with traditional oscillatory rheology.

Finally, in Chapter 6, I used the indirect interfacial rheometer to measure how stresses propagate across a complex liquid-liquid interface. By tracking a low concentration of fluorescent particles in the water phase, the flow behaviour at both the interface and in the lower phase was measured. I observed that the rheological properties of the interface play a key role in the transfer of stresses across that interface. While the interface behaves as a fluid, there appears to be no barrier to stress propagation and the lower phase flows as expected. This may be as the interface does little to "shield" the lower phase from external stresses. On the other hand, this could be because, as in the case of an elastic interface, the lower phase follows the interface; as the interface is viscous in this instance the lower phase is also observed to be viscous. However, if the interface behaves as a solid, the response of the lower phase closely follows that of the interface such that it appears that the lower water phase behaves as an elastic material, i.e. the elastic interface "shields" the lower phase from external stresses. This has profound implications for droplet-like systems in external flows, where the internal phase may need to be protected to maintain functionality. The development of this technique might open up a route to investigate the effect of external flows in other systems, such as phospholipid laden interfaces which are especially relevant for, e.g., blood cells.

In summary, I have investigated the interactions and rheology of particle laden fluid interfaces. Using complementary techniques I have improved the understanding of these systems by adding the behaviour of interfacially adsorbed (uncharged) sterically stabilised particles to the existing literature. I have demonstrated theoretically new physics in this field which has not been observed previously, and have backed up these theories with experimental data. Furthermore, I have demonstrated the applicability of a novel interfacial rheology technique which can probe systems in an industrially relevant manner and allows measurements of interfacial viscosities at lower values than have previously been achieved. This technique has then been extended to measure how stresses propagates across a complex fluid-fluid interface which is important for many droplet-like systems in an external flow field.

Appendix A

Bayesian Model Comparison

The following derivation of the posterior probability ratio is an edited version of chapter 4 in Sivia, D.S. [91].

Consider 2 models, monopole (m) and dipole (d). These are described by the two equations for interparticle potential, $U(r)$, given below:

$$U_m(r) = \frac{A}{r}e^{-\lambda r} \qquad \text{and} \qquad U_d(r) = \frac{A}{r}e^{-\lambda r} + \frac{B}{r^3}. \tag{A.1}$$

Here, λ is the inverse screening length and A and B are the relative strengths of the monopole or dipole interactions.

I can compare how well these two models fit a dataset by taking the posterior ratio

$$\text{posterior ratio} = \text{PR} = \frac{P(m|D,I)}{P(d|D,I)}, \tag{A.2}$$

where P is the probability, D is the data (here the data consists of measured interparticle potentials $U_i(r_i)$) and I is any initial belief I hold before making any measurements.

I can use Bayes' theorem,

$$P(X|Y,I) = \frac{P(Y|X,I)P(X|I)}{P(Y|I)}, \tag{A.3}$$

to rearrange this to give

$$\mathrm{PR} = \frac{P(D|m,I)P(m|I)}{P(D|d,I)P(d|I)}, \tag{A.4}$$

where the term $P(D|I)$ is the same in the numerator and denominator so cancels out.

I begin by assuming no prior knowledge of which model is more likely, that is to say

$$P(m|I) = P(d|I). \tag{A.5}$$

Now, I focus on the numerator and can make generalisations to write down a similar form for the denominator with no extra work. I note, however, that m has 2 parameters while d has 3.

Using marginalisation, I can write the numerator as

$$P(D|m,I) = \int\int P(D,A,\lambda|m,I)\mathrm{d}A\mathrm{d}\lambda. \tag{A.6}$$

In words this statement says that the probability of the data given our model, m, is the probability of that data with specific parameters A and λ, integrated over every possible realisation of A and λ. Note that the integrand involves the probability of our model m and the parameters A and λ, not the probability of m given parameters A and λ.

I can re-express the integrand by noting the product rule: the probability of two events, X and Y, happening is the probability of Y happening multiplied by the probability of X happening given that Y has already happened. In mathematical terms this means

$$P(X,Y|I) = P(Y|I)P(X|Y,I). \tag{A.7}$$

Applying this to A.6 twice I find

$$P(D|m,I) = \int\int P(D|A,\lambda,m,I)P(A|m,I)P(\lambda|m,I)dAd\lambda. \tag{A.8}$$

To continue further, I therefore need to come up with some prior probability for

a value of A (and λ). The simplest argument I can make is that it is a uniform probability distribution below some maximum value but above zero as I know this is a repulsive potential ($P(\lambda|m,I)$ will have the same properties). I can write the probability distribution for A as

$$P(A|m,I) = \begin{cases} \frac{1}{A_{\max}} & \text{if} \quad 0 \leq A \leq A_{\max} \\ 0 & \text{otherwise} \end{cases} . \tag{A.9}$$

So I find

$$P(D|m,I) = \frac{1}{\lambda_{\max} A_{\max}} \int_0^{A_{\max}} dA \int_0^{\lambda_{\max}} \mathrm{d}\lambda \; P(D|A,\lambda,m,I). \tag{A.10}$$

Now I must make an assumption for the form of $P(D|A,\lambda,m,I)$. I assume there are some best fit parameters to describe this model A_0 and λ_0 so I can take this probability distribution as the probability of this data given those best fit parameters with a Gaussian distribution of those parameters, i.e.

$$P(D|A,\lambda,m,I) = P(D|A_0,\lambda_0,m,I) e^{\left(-\frac{(\lambda-\lambda_0)^2}{2\delta\lambda^2}\right)} e^{\left(-\frac{(A-A_0)^2}{2\delta A^2}\right)}. \tag{A.11}$$

If I assume the uniform distribution completely encompasses the Gaussian shape (to a good approximation), i.e. $e^{\left(-\frac{(A_{\max}-A_0)^2}{2\delta A^2}\right)} \sim 0$ and $e^{\left(-\frac{(A_0)^2}{2\delta A^2}\right)} \sim 0$, and similarly for λ then I can take the limits of the Gaussian integrals to $\pm\infty$ and perform the integrals to get

$$P(D|m,I) = \frac{P(D|A_0^{(m)},\lambda_0^{(m)},m,I) 2\pi \delta\lambda^{(m)} \delta A^{(m)}}{A_{\max}\lambda_{\max}}, \tag{A.12}$$

where I have introduced the monopole superscript label to distinguish from any dipole fits that I make. The $A_{\max}$ and $\lambda_{\max}$ parameters have no such label as there is no *a priori* reason to take these as different to the dipole case.

Through the same reasoning I can now write down the denominator of PR

$$P(D|d,I) = \frac{P(D|A_0^{(d)},B_0,\lambda_0^{(d)},d,I)(2\pi)^{\frac{3}{2}} \delta\lambda^{(d)} \delta A^{(d)} \delta B}{A_{\max}\lambda_{\max}B_{\max}}. \tag{A.13}$$

If, however, I have a situation where the error on the parameter is much

larger than the best estimate of the parameter, I are forced to reconsider the approximation of taking the integral to $\pm\infty$. I can often get around this by taking the limits as 0 to $+\infty$, leading to an extra factor of 0.5 in equation A.13 if I were to find $B_{\max} \gg \delta B \gg B_0$.

Ignoring this minor detail, putting equation A.13 back into the posterior ratio I find

$$\mathrm{PR} = \frac{P(D|A_0^{(m)}, \lambda_0^{(m)}, m, I)}{P(D|A_0^{(d)}, B_0, \lambda_0^{(d)}, d, I)} \frac{B_{\max}\delta\lambda^{(m)}\delta A^{(m)}}{(2\pi)^{\frac{1}{2}}\delta\lambda^{(d)}\delta A^{(d)}\delta B}. \tag{A.14}$$

The δX values will come out of the fitting procedure to obtain best fit values for the parameters in each model. The probabilities can be taken as a product of normal distribution for the probability of each point, that is

$$P(D|A_0\lambda_0, m, I) = \prod_{i=1}^{N} \frac{1}{\sigma_i\sqrt{2\pi}} \exp\left(-\frac{1}{2}\frac{(U_i(r_i) - U_m(r_i; A_0, \lambda_0))^2}{\sigma_i^2}\right), \tag{A.15}$$

where σ_i is the measurement error on data point i. I have a very similar expression for the dipole model.

I can take $B_{\max}$ as the mean value for the dipole prefactor in (Park, 2010)[1] which gives a value of 5.1×10^5 $k_\mathrm{B}T\mu\mathrm{m}^3$. This can be taken as, *a priori*, I expect sterically stabilised particles, which I use, to have a weaker interaction than charge stabilised particles, used by Park, et al.

[1] B. J. Park, J. Vermant, and E. M. Furst, Soft Matter 6, 5327 (2010)

Bibliography

[1] E. Dickinson. Hydrocolloids at interfaces and the influence on the properties of dispersed systems. *Food Hydrocolloids*, 17(1):25–39, 2003.

[2] G. G. Fuller and J. Vermant. Complex Fluid-Fluid Interfaces: Rheology and Structure. *Annual Review of Chemical and Biomolecular Engineering*, 3(1):519–543, 2012.

[3] J. H. J. Thijssen and J. Vermant. Interfacial rheology of model particles at liquid interfaces and its relation to (bicontinuous) Pickering emulsions. *Journal of Physics Condensed Matter*, 30:023002, 2018.

[4] B. P. Binks. Particles as surfactants—similarities and differences. *Current Opinion in Colloid and Interface Science*, 7(1-2):21–41, 2002.

[5] W. Ramsden. Separation of solids in the surface-layers of solutions and suspensions (Observations on surface-membranes, bubbles, emulsions, and mechanical coagulation. Preliminary account. *Proceedings of the Royal Society of London*, 72(477-486):156–164, 1903.

[6] S. U. Pickering. Emulsions. *Journal of the Chemical Society, Transactions*, 91:2001–2021, 1907.

[7] P. Pieranski. Two-dimensional interfacial colloidal crystals. *Physical Review Letters*, 45(7):569–572, 1980.

[8] R. Aveyard, B. P. Binks, J. H. Clint, P. D. Fletcher, T. S. Horozov, B. Neumann, V. N. Paunov, J. Annesley, S. W. Botchway, D. Nees, A. W. Parker, A. D. Ward, and A. N. Burgess. Measurement of long-range repulsive forces between charged particles at an oil-water interface. *Physical Review Letters*, 88(24):2461021–2461024, 2002.

[9] K. Masschaele, B. J. Park, E. M. Furst, J. Fransaer, and J. Vermant. Finite ion-size effects dominate the interaction between charged colloidal particles at an oil-water interface. *Physical Review Letters*, 105(4):048303, 2010.

[10] R. van Hooghten, V. E. Blair, A. Vananroye, A. B. Schofield, J. Vermant, and J. H. J. Thijssen. Interfacial Rheology of Sterically Stabilized Colloids at Liquid Interfaces and Its Effect on the Stability of Pickering Emulsions. *Langmuir*, 33:4107–4118, 2017.

[11] P. N. Pusey and W. van Megen. Phase behaviour of concentrated suspensions of nearly hard colloidal spheres. *Nature*, 320(6060):340–342, 1986.

[12] E. J. Stancik, A. L. Hawkinson, J. Vermant, and G. G. Fuller. Dynamic transitions and oscillatory melting of a two-dimensional crystal subjected to shear flow. *Journal of Rheology*, 48(1):159–173, 2004.

[13] S. Reynaert, P. Moldenaers, and J. Vermant. Interfacial rheology of stable and weakly aggregated two-dimensional suspensions. *Physical Chemistry Chemical Physics*, 9(48):6463–6475, 2007.

[14] P. J. Yunker, T. Still, M. A. Lohr, and A. G. Yodh. Suppression of the coffee-ring effect by shape-dependent capillary interactions. *Nature*, 476(7360):308–311, 2011.

[15] S. Barman and G. F. Christopher. Simultaneous interfacial rheology and microstructure measurement of densely aggregated particle laden interfaces using a modified double wall ring interfacial rheometer. *Langmuir*, 30(32):9752–9760, 2014.

[16] S. Barman and G. F. Christopher. Role of capillarity and microstructure on interfacial viscoelasticity of particle laden interfaces. *Journal of Rheology*, 60(1):35–45, 2016.

[17] T. S. Horozov, R. Aveyard, J. H. Clint, and B. P. Binks. Order-disorder transition in monolayers of modified monodisperse silica particles at the octane-water interface. *Langmuir*, 19(7):2822–2829, 2003.

[18] B. P. Binks and T. S. Horozov, editors. *Colloidal Particles at Liquid Interfaces*. Cambridge University Press, 2006.

[19] P. S. Clegg, E. M. Herzig, A. B. Schofield, S. U. Egelhaaf, T. S. Horozov, B. P. Binks, M. E. Cates, and W. C. K. Poon. Emulsification of partially miscible liquids using colloidal particles: Nonspherical and extended domain structures. *Langmuir*, 23(11):5984–5994, 2007.

[20] A. D. Law, M. Auriol, D. Smith, T. S. Horozov, and D. M. A. Buzza. Self-assembly of two-dimensional colloidal clusters by tuning the hydrophobicity, composition, and packing geometry. *Physical Review Letters*, 110(13), 2013.

[21] I. Buttinoni, Z. A. Zell, T. M. Squires, and L. Isa. Colloidal binary mixtures at fluid–fluid interfaces under steady shear: structural, dynamical and mechanical response. *Soft Matter*, 11(42):8313–8321, 2015.

[22] W. H. Hager. Wilfrid Noel Bond and the Bond number. *Journal of Hydraulic Research*, 50(1):3–9, 2012.

[23] D. Vella. Floating Versus Sinking. *Annual Review of Fluid Mechanics*, 47(1):115–135, 2015.

[24] R. Aveyard, B. P. Binks, and J. H. Clint. Emulsions stabilised solely by colloidal particles. *Advances in Colloid and Interface Science*, 100-102:503–546, 2003.

[25] K. Stratford, R. Adhikari, I. Pagonabarraga, J-C. Desplat, and M. E. Cates. Colloidal jamming at interfaces: a route to fluid-bicontinuous gels. *Science*, 309(5744):2198–2201, 2005.

[26] E. M. Herzig, K. A. White, A. B. Schofield, W. C. K. Poon, and P. S. Clegg. Bicontinuous emulsions stabilized solely by colloidal particles. *Nature Materials*, 6(12):966–971, 2007.

[27] M. Reeves, K. Stratford, and J. H. J. Thijssen. Quantitative morphological characterization of bicontinuous Pickering emulsions via interfacial curvatures. *Soft Matter*, 12(12):4082–4092, 2016.

[28] K. L. Dickinson, U. K. Wiegand, and J. H. J. Thijssen. Soft Meets Hard – How Does Freeze-Thaw Cycling Affect the Microstructure of Particle-Stabilised Emulsions? arxiv:1902.08531, 2019.

[29] K. L. Dickinson. *Microscopic study of the freeze-thaw stability of particle-stabilised emulsions*. PhD thesis, The University of Edinburgh, 2020.

[30] J. W. Tavacoli, J. H. J. Thijssen, and P. S. Clegg. CHAPTER 6. Bicontinuous Emulsions Stabilized by Colloidal Particles. In *Particle-Stabilized Emulsions and Colloids: Formation and Applications*, pages 129–168. Royal Society of Chemistry, 2015.

[31] L. Maurice, R. A. Maguire, A. B. Schofield, M. E. Cates, P. S. Clegg, and J. H. J. Thijssen. Squeezing particle-stabilized emulsions into biliquid foams – equation of state. *Soft Matter*, 9(32):7757–7765, 2013.

[32] S. Arditty, V. Schmitt, J. Giermanska-Kahn, and F. Leal-Calderon. Materials based on solid-stabilized emulsions. *Journal of Colloid and Interface Science*, 275(2):659–664, 2004.

[33] M. Destribats, S. Gineste, E. Laurichesse, H. Tanner, F. Leal-Calderon, V. Héroguez, and V. Schmitt. Pickering emulsions: What are the main parameters determining the emulsion type and interfacial properties? *Langmuir*, 30(31):9313–9326, 2014.

[34] R. Besseling, L. Isa, E. R. Weeks, and W. C. K. Poon. Quantitative imaging of colloidal flows. *Advances in Colloid and Interface Science*, 146(1-2):1–17, 2009.

[35] M. Hermes and P. S. Clegg. Yielding and flow of concentrated Pickering emulsions. *Soft Matter*, 9(31):7568, 2013.

[36] D. J. French, P. Taylor, J. Fowler, and P. S. Clegg. Making and breaking bridges in a Pickering emulsion. *Journal of Colloid and Interface Science*, 441:30–38, 2015.

[37] T. M. Fischer, M. Stöhr-Lissen, and H. Schmid-Schönbein. The red cell as a fluid droplet: tank tread-like motion of the human erythrocyte membrane in shear flow. *Science (New York, N.Y.)*, 202(4370):894–896, 1978.

[38] S. R. Keller and R. Skalak. Motion of a tank-treading ellipsoidal particle in a shear flow. *Journal of Fluid Mechanics*, 120:27–47, 1982.

[39] V. Kantsler and V. Steinberg. Orientation and Dynamics of a Vesicle in Tank-Treading Motion in Shear Flow. *Physical Review Letters*, 95(25):258101, 2005.

[40] A. B. Subramaniam, M. Abkarian, L. Mahadevan, and H. A. Stone. Mechanics of interfacial composite materials. *Langmuir*, 22(24):10204–10208, 2006.

[41] R. A. L. Jones. *Soft Condensed Matter*. Oxford University Press, 2002.

[42] G. Bosma, C. Pathmamanoharan, E. H. A. de Hoog, W. K. Kegel, A. van Blaaderen, and H. N. W. Lekkerkerker. Preparation of monodisperse, fluorescent PMMA-latex colloids by dispersion polymerization. *Journal of Colloid and Interface Science*, 245(2):292–300, 2002.

[43] G. Bryant, S. R. Williams, L. Qian, I. K. Snook, E. Perez, and F. Pincet. How hard is a colloidal "hard-sphere" interaction? *Physical Review E - Statistical, Nonlinear, and Soft Matter Physics*, 66(6):3–6, 2002.

[44] P. A. Kralchevsky and K. Nagayama. Capillary interactions between particles bound to interfaces, liquid films and biomembranes. *Advances in Colloid and Interface Science*, 85(2):145–192, 2000.

[45] P. A. Kralchevsky and K. Nagayama. Capillary forces between colloidal particles. *Langmuir*, 10(1):23–36, 1994.

[46] K. D. Danov and P. A. Kralchevsky. Capillary forces between particles at a liquid interface: General theoretical approach and interactions between capillary multipoles. *Advances in Colloid and Interface Science*, 154(1-2):91–103, 2010.

[47] A. J. Hurd. The electrostatic interaction between spherical colloidal particles. *Journal of Physics A: Mathematical and General*, 18(18):L1055–L1060, 1985.

[48] F. H. Stillinger. Interfacial solutions of the poisson-boltzmann equation. *The Journal of Chemical Physics*, 35:1584–1589, 1961.

[49] R. Aveyard, J. H. Clint, D. Nees, and V. N. Paunov. Compression and structure of monolayers of charged latex particles at air/water and octane/water interfaces. *Langmuir*, 16(4):1969–1979, 2000.

[50] B. J. Park, J. P. Pantina, E. M. Furst, M. Oettel, S. Reynaert, and J. Vermant. Direct measurements of the effects of salt and surfactant on interaction forces between colloidal particles at water-oil interfaces. *Langmuir*, 24(5):1686–1694, 2008.

[51] C. L. Wirth, E. M. Furst, and J. Vermant. Weak electrolyte dependence in the repulsion of colloids at an oil-water interface. *Langmuir*, 30:2670–5, 2014.

[52] L. Parolini, A. D. Law, A. Maestro, D. M. A. Buzza, and P. Cicuta. Interaction between colloidal particles on an oil–water interface in dilute and dense phases. *Journal of Physics: Condensed Matter*, 27(19):194119, 2015.

[53] B. J. Park, J. Vermant, and E. M. Furst. Heterogeneity of the electrostatic repulsion between colloids at the oil–water interface. *Soft Matter*, 6(21):5327, 2010.

[54] C. F. Brooks, G. G. Fuller, C. W. Frank, and C. R. Robertson. Interfacial stress rheometer to study rheological transitions in monolayers at the air-water interface. *Langmuir*, 15(7):2450–2459, 1999.

[55] S. Reynaert, C. F. Brooks, P. Moldenaers, J. Vermant, and G. G. Fuller. Analysis of the magnetic rod interfacial stress rheometer. *Journal of Rheology*, 52(1):261–285, 2008.

[56] T. Verwijlen, P. Moldenaers, H. A. Stone, and J. Vermant. Study of the flow field in the magnetic rod interfacial stress rheometer. *Langmuir*, 27(15):9345–9358, 2011.

[57] S. Vandebril, A. Franck, G. G. Fuller, P. Moldenaers, and J. Vermant. A double wall-ring geometry for interfacial shear rheometry. *Rheologica Acta*, 49(2):131–144, 2010.

[58] J. T. Petkov, T. D. Gurkov, B. E. Campbell, and R. P. Borwankar. Dilatational and shear elasticity of gel-like protein layers on air/water interface. *Langmuir*, 16(8):3703–3711, 2000.

[59] P. Cicuta and E. M. Terentjev. Viscoelasticity of a protein monolayer from anisotropic surface pressure measurements. *European Physical Journal E*, 16(2):147–158, 2005.

[60] D. Zang, D. Langevin, B. P. Binks, and B. Wei. Shearing particle monolayers: Strain-rate frequency superposition. *Physical Review E - Statistical, Nonlinear, and Soft Matter Physics*, 81(1), 2010.

[61] F. Ravera, E. Santini, G. Loglio, M. Ferrari, and L. Liggieri. Effect of nanoparticles on the interfacial properties of liquid/liquid and liquid/air surface layers. *Journal of Physical Chemistry B*, 110(39):19543–19551, 2006.

[62] F. Ravera, G. Loglio, and V. I. Kovalchuk. Interfacial dilational rheology by oscillating bubble/drop methods. *Current Opinion in Colloid and Interface Science*, 15(4):217–228, 2010.

[63] L. Liggieri, E. Santini, E. Guzmán, A. Maestro, and F. Ravera. Wide-frequency dilational rheology investigation of mixed silica nanoparticle–CTAB interfacial layers. *Soft Matter*, 7(17):7699–7709, 2011.

[64] M. Doi. *Soft Matter Physics*. Oxford University Press, 2013.

[65] K. E. J. Barrett. *Dispersion polymerization in organic media*. Wiley, 1975.

[66] H. Ono and H. Saeki. Preparation and properties of polymethyl methacrylate latex dispersions having no surfactant. *Colloid and Polymer Science*, 253(9):744–749, 1975.

[67] Thermo Fisher Scientific. Fluorescence SpectraViewer. Date accessed: 16 July 2020.

[68] C. Sheppard. *Confocal laser scanning microscopy*. BIOS Scientific, Oxford, 1997.

[69] T. Zemb and P. Lindner, editors. *Neutrons, X-rays and light: scattering methods applied to soft condensed matter*. North-Holland, 2002.

[70] C. F. Bohren and D. R. Huffman. *Absorption and scattering of light by small particles*. John Wiley & Sons, Ltd, New York, 1998.

[71] I. T. Horváth, P. Colinet, and M. R. Vetrano. Measuring contact angles of small spherical particles at planar fluid interfaces by Light Extinction. *Applied Physics Letters*, 108(20):201605, 2016.

[72] George M Hale and Marvin R Querry. Optical constants of water in the 200-nm to 200-μm wavelength region. *Applied optics*, 12(3):555–563, 1973.

[73] Mohammed Yahya and M Ziad Saghir. Prediction and experimental measurement of refractive index in ternary hydrocarbon mixtures. *Journal of Chemical & Engineering Data*, 60(8):2329–2342, 2015.

[74] Francis A Jenkins and Harvey E White. *Fundamentals of optics, 4th edition*. Tata McGraw-Hill Education, 1981.

[75] I. Muntz, F. Waggett, M. Hunter, A. B. Schofield, P. Bartlett, D. Marenduzzo, and J. H. J. Thijssen. Interaction between Nearly Hard Colloidal Spheres at an Oil-Water Interface. *Physical Review Research*, 2(2):023388, 2020.

[76] P. J. Wilde. Interfaces: Their role in foam and emulsion behaviour. *Current Opinion in Colloid and Interface Science*, 5:176–181, 2000.

[77] F. Leal-Calderon and V. Schmitt. Solid-stabilized emulsions. *Current Opinion in Colloid and Interface Science*, 13(4):217–227, 2008.

[78] T. N. Hunter, R. J. Pugh, G. V. Franks, and G. J. Jameson. The role of particles in stabilising foams and emulsions. *Advances in Colloid and Interface Science*, 137(2):57–81, 2008.

[79] J. H. J. Thijssen, A. B. Schofield, and P. S. Clegg. How do (fluorescent) surfactants affect particle-stabilized emulsions? *Soft Matter*, 7(18):7965, 2011.

[80] C. P. Kelleher, A. Wang, G. I. Guerrero-García, A. D. Hollingsworth, R. E. Guerra, B. J. Krishnatreya, D. G. Grier, V. N. Manoharan, and P. M. Chaikin. Charged hydrophobic colloids at an oil-aqueous phase interface. *Physical Review E - Statistical, Nonlinear, and Soft Matter Physics*, 92(6):062306, 2015.

[81] C. P. Kelleher, R. E. Guerra, A. D. Hollingsworth, and P. M. Chaikin. Phase behavior of charged colloids at a fluid interface. *Physical Review E - Statistical, Nonlinear, and Soft Matter Physics*, 95:022602, 2017.

[82] M. E. Leunissen, A. van Blaaderen, A. D. Hollingsworth, M. T. Sullivan, and P. M. Chaikin. Electrostatics at the oil-water interface, stability, and order in emulsions and colloids. *Proceedings of the National Academy of Sciences*, 104:2585–90, 2007.

[83] N. D. Mermin. Crystalline order in two dimensions. *Physical Review*, 176(1):250–254, 1968.

[84] A. Morozov, I. Muntz, J. H. J. Thijssen, and D. Marenduzzo. Debye-Hückel potential at an interface between two media. *Physical Review E*, (accepted), 2020.

[85] F. Waggett, M. Shafiq, and P. Bartlett. Failure of Debye-Hückel Screening in Low-Charge Colloidal Suspensions. *Colloids and Interfaces*, 2(4):51, 2018.

[86] S. D. Finlayson and P. Bartlett. Non-additivity of pair interactions in charged colloids. *Journal of Chemical Physics*, 145(3), 2016.

[87] D. Allan, C. van der Wel, N. Keim, T. A Caswell, D. Wieker, R. Verweij, C. Reid, Thierry, L. Grueter, K. Ramos, Apiszcz, Zoeith, R. W. Perry, F. Boulogne, P. Sinha, Pfigliozzi, N. Bruot, L. Uieda, J. Katins, H. Mary, and A. Ahmadia. soft-matter/trackpy: Trackpy v0.4.2. 2019.

[88] S. H. Behrens and D. G. Grier. Pair interaction of charged colloidal spheres near a charged wall. *Physical Review E - Statistical, Nonlinear, and Soft Matter Physics*, 64(5):050401, 2001.

[89] S. K. Sainis, V. Germain, and E. R. Dufresne. Statistics of particle trajectories at short time intervals reveal fN-scale colloidal forces. *Physical Review Letters*, 99(1):018303, 2007.

[90] M. Winterhalter and W. Helfrich. Effect of Surface Charge on the Curvature Elasticity. *Journal of Physical Chemistry*, 92:6865–6867, 1988.

[91] D. Sivia. *Data Analysis: A Bayesian Tutorial*. Oxford: Clarendon, 1996.

[92] G. N. Smith, S. D. Finlayson, S. E. Rogers, P. Bartlett, and J. Eastoe. Electrolyte-induced instability of colloidal dispersions in nonpolar solvents. *Journal of Physical Chemistry Letters*, 8(19):4668–4672, 2017.

[93] K. G. Marinova, R. G. Alargova, N. D. Denkov, O. D. Velev, D. N. Petsev, I. B. Ivanov, and R. P. Borwankar. Charging of Oil-Water Interfaces Due to Spontaneous Adsorption of Hydroxyl Ions. *Langmuir*, 12(8):2045–2051, 1996.

[94] J. K. Beattie and A. M. Djerdjev. The pristine oil/water interface: Surfactant-free hydroxide-charged emulsions. *Angewandte Chemie - International Edition*, 43(27):3568–3571, 2004.

[95] P. Creux, J. Lachaise, A. Graciaa, J. K. Beattie, and A. M. Djerdjev. Strong specific hydroxide ion binding at the pristine oil/water and air/water interfaces. *Journal of Physical Chemistry B*, 113(43):14146–14150, 2009.

[96] R. Vácha, S. W. Rick, P. Jungwirth, A. G.F. De Beer, H. B. De Aguiar, J. S. Samson, and S. Roke. The orientation and charge of water at the hydrophobic oil droplet - Water interface. *Journal of the American Chemical Society*, 133(26):10204–10210, 2011.

[97] D. Wang and H. Möhwald. Rapid fabrication of binary colloidal crystals by stepwise spin-coating. *Advanced Materials*, 16(3):244–247, 2004.

[98] G. Zhang, D. Wang, Z. Z. Gu, and H. Mchwald. Fabrication of superhydrophobic surfaces from binary colloidal assembly. *Langmuir*, 21(20):9143–9148, 2005.

[99] T. Honold, K. Volk, M. Retsch, and M. Karg. Binary plasmonic honeycomb structures: High-resolution EDX mapping and optical properties. *Colloids and Surfaces A: Physicochemical and Engineering Aspects*, 510:198–204, 2016.

[100] J. J. Urban, D. V. Talapin, E. V. Shevchenko, C. R. Kagan, and C. B. Murray. Synergism in binary nanocrystal superlattices leads to enhanced p-type conductivity in self-assembled PbTe/Ag2Te thin films. *Nature Materials*, 6(2):115–121, 2007.

[101] L. Assoud, R. Messina, and H. Löwen. Stable crystalline lattices in two-dimensional binary mixtures of dipolar particles. *EPL*, 80(4):48001, 2007.

[102] J. Fornleitner, F. Lo Verso, G. Kahl, and C. N. Likos. Genetic algorithms predict formation of exotic ordered configurations for two-component dipolar monolayers. *Soft Matter*, 4(3):480–484, 2008.

[103] J. Fornleitner, F. L. Verso, G. Kahl, and C. N. Likos. Ordering in two-dimensional dipolar mixtures. *Langmuir*, 25(14):7836–7846, 2009.

[104] C. N. Likos and C. L. Henley. Complex alloy phases for binary hard-disc mixtures. *Philosophical Magazine B: Physics of Condensed Matter; Statistical Mechanics, Electronic, Optical and Magnetic Properties*, 68(1):85–113, 1993.

[105] T. Stirner and J. Sun. Molecular dynamics simulation of the structural configuration of binary colloidal monolayers. *Langmuir*, 21(14):6636–6641, 2005.

[106] A. D. Law, T. S. Horozov, and D. M. A. Buzza. The structure and melting transition of two-dimensional colloidal alloys. *Soft Matter*, 7(19):8923–8931, 2011.

[107] J. Dzubiella, G. P. Hoffmann, and H. Löwen. Lane formation in colloidal mixtures driven by an external field. *Physical Review E - Statistical Physics, Plasmas, Fluids, and Related Interdisciplinary Topics*, 65(2):021402, 2002.

[108] L. Assoud, R. Messina, and H. Löwen. Binary crystals in two-dimensional two-component Yukawa mixtures. *Journal of Chemical Physics*, 129(16):164511, 2008.

[109] R. Mears, I. Muntz, and J. H. J. Thijssen. Surface Pressure of Liquid Interfaces Laden with Micron-Sized Particles. arxiv:2005.02352, 2020.

[110] A. D. Law, D. M. A. Buzza, and T. S. Horozov. Two-dimensional colloidal alloys. *Physical Review Letters*, 106(12):128302, 2011.

[111] T. S. Horozov, R. Aveyard, B. P. Binks, and J. H. Clint. Structure and stability of silica particle monolayers at horizontal and vertical octane-water interfaces. *Langmuir*, 21(16):7405–7412, 2005.

[112] L. J. Bonales, F. Martínez-Pedrero, M. A. Rubio, R. G. Rubio, and F. Ortega. Phase behavior of dense colloidal binary monolayers. *Langmuir*, 28(48):16555–16566, 2012.

[113] M. Á. Fernández-Rodríguez, R. Elnathan, R. Ditcovski, F. Grillo, G. M. Conley, F. Timpu, A. Rauh, K. Geisel, T. Ellenbogen, R. Grange, F. Scheffold, M. Karg, W. Richtering, N. H. Voelcker, and L. Isa. Tunable 2D binary colloidal alloys for soft nanotemplating. *Nanoscale*, 10(47):22189–22195, 2018.

[114] T. Nallamilli, S. Ragothaman, and M. G. Basavaraj. Self assembly of oppositely charged latex particles at oil-water interface. *Journal of Colloid and Interface Science*, 486:325–336, 2017.

[115] T. Vissers, A. Wysocki, M. Rex, H. Löwen, C. P. Royall, A. Imhof, and A. van Blaaderen. Lane formation in driven mixtures of oppositely charged colloids. *Soft Matter*, 7(6):2352–2356, mar 2011.

[116] V. Lotito and T. Zambelli. Pattern Formation in Binary Colloidal Assemblies: Hidden Symmetries in a Kaleidoscope of Structures. *Langmuir*, 34(26):7827–7843, 2018.

[117] K. Masschaele, J. Fransaer, and J. Vermant. Flow-induced structure in colloidal gels: direct visualization of model 2D suspensions. *Soft Matter*, 7(17):7717, 2011.

[118] N. C. Keim and P. E. Arratia. Yielding and microstructure in a 2D jammed material under shear deformation. *Soft Matter*, 9(27):6222, 2013.

[119] B. Brugger, J. Vermant, and W. Richtering. Interfacial layers of stimuli-responsive poly-(N-isopropylacrylamide-co- methacrylicacid) (PNIPAM-co-MAA) microgels characterized by interfacial rheology and compression isotherms. *Physical Chemistry Chemical Physics*, 12(43):14573–14578, 2010.

[120] S. Razavi, K. D. Cao, B. Lin, K. Y. C. Lee, R. S. Tu, and I. Kretzschmar. Collapse of Particle-Laden Interfaces under Compression: Buckling vs Particle Expulsion. *Langmuir*, 31(28):7764–7775, 2015.

[121] V. Garbin, I. Jenkins, T. Sinno, J. C. Crocker, and K. J. Stebe. Interactions and stress relaxation in monolayers of soft nanoparticles at fluid-fluid interfaces. *Physical Review Letters*, 114(10):108301, 2015.

[122] K. Kim, S. Q. Choi, J. A. Zasadzinski, and T. M. Squires. Interfacial microrheology of DPPC monolayers at the air-water interface. *Soft Matter*, 7(17):7782–7789, 2011.

[123] J. Schindelin, I. Arganda-Carreras, E. Frise, V. Kaynig, M. Longair, T. Pietzsch, S. Preibisch, C. Rueden, S. Saalfeld, B. Schmid, J. Y. Tinevez, D. J. White, V. Hartenstein, K. Eliceiri, P. Tomancak, and A. Cardona. Fiji: An open-source platform for biological-image analysis, v1.52n. *Nature Methods*, 9(7):676–682, 2012.

[124] C. W. Macosko. *Rheology: Principles, Measurements, and Applications*. VCH, New York, 1994.

[125] D. Stamou, C. Duschl, and D. Johannsmann. Long-range attraction between colloidal spheres at the air-water interface: The consequence of an irregular meniscus. *Physical Review E - Statistical Physics, Plasmas, Fluids, and Related Interdisciplinary Topics*, 62(4 B):5263–5272, 2000.

[126] R. van Hooghten, L. Imperiali, V. Boeckx, R. Sharma, and J. Vermant. Rough nanoparticles at the oil-water interfaces: Their structure, rheology and applications. *Soft Matter*, 9(45):10791–10798, 2013.

[127] J. Mewis and J. Vermant. Rheology of sterically stabilized dispersions and lattices. *Progress in Organic Coatings*, 40(1-4):111–117, dec 2000.

[128] E. R. Weeks and D. A. Weitz. Properties of Cage Rearrangements Observed near the Colloidal Glass Transition. *Physical Review Letters*, 89(9):095704, 2002.

[129] L. Imperiali, K. H. Liao, C. Clasen, J. Fransaer, C. W. Macosko, and J. Vermant. Interfacial rheology and structure of tiled graphene oxide sheets. *Langmuir*, 28(21):7990–8000, 2012.

[130] R. van Hooghten. Personal Communication, 2019.

[131] T. G. Mason, J. Bibette, and D. A. Weitz. Yielding and flow of monodisperse emulsions. *Journal of Colloid and Interface Science*, 179(2):439–448, 1996.

[132] R. D. Groot and S. D. Stoyanov. Equation of state of surface-adsorbing colloids. *Soft Matter*, 6(8):1682–1692, 2010.

[133] J. P. Rane, V. Pauchard, A. Couzis, and S. Banerjee. Interfacial rheology of asphaltenes at oil-water interfaces and interpretation of the equation of state. *Langmuir*, 29(15):4750–4759, 2013.

[134] L. G. Torres, R. Iturbe, M. J. Snowden, B. Z. Chowdhry, and S. A. Leharne. Preparation of o/w emulsions stabilized by solid particles and their characterization by oscillatory rheology. *Colloids and Surfaces A: Physicochemical and Engineering Aspects*, 302(1-3):439–448, 2007.

[135] J. Bibette, F. L. Calderon, and P. Poulin. Emulsions: basic principles. *Reports on Progress in Physics*, 62(6):969—-1033, 1999.

[136] C. Washington. Stability of lipid emulsions for drug delivery. *Advanced Drug Delivery Reviews*, 20(2-3):131–145, 1996.

[137] J. Frelichowska, M. A. Bolzinger, J. P. Valour, H. Mouaziz, J. Pelletier, and Y. Chevalier. Pickering w/o emulsions: Drug release and topical delivery. *International Journal of Pharmaceutics*, 368(1-2):7–15, 2009.

[138] N. Korin, M. Kanapathipillai, B. D. Matthews, M. Crescente, A. Brill, T. Mammoto, K. Ghosh, S. Jurek, S. A. Bencherif, D. Bhatta, A. U. Coskun, C. L. Feldman, D. D. Wagner, and D. E. Ingber. Shear-activated nanotherapeutics for drug targeting to obstructed blood vessels. *Science*, 337(6095):738–742, 2012.

[139] K. S. Sakariassen, S. R. Hanson, and Y. Cadroy. Methods and models to evaluate shear-dependent and surface reactivity-dependent antithrombotic efficacy. *Thrombosis Research*, 104(3):149–174, 2001.

[140] M. R. K. Mofrad. Rheology of the Cytoskeleton. *Annual Review of Fluid Mechanics*, 41(1):433–453, 2009.

[141] P. A. Pullarkat, P. A. Fernández, and A. Ott. Rheological properties of the Eukaryotic cell cytoskeleton. *Physics Reports*, 449(1-3):29–53, 2007.

[142] J. W. Tavacoli, J. H.J. Thijssen, A. B. Schofield, and P. S. Clegg. Novel, robust, and versatile bijels of nitromethane, ethanediol, and colloidal silica: Capsules, sub-ten-micrometer domains, and mechanical properties. *Advanced Functional Materials*, 21(11):2020–2027, 2011.